3-2006

Alleviation of Buffet-Induced Vibration Using Piezoelectric Actuators

Shawn D. Morganstern

ALLEVIATION OF BUFFET-INDUCED VIBRATION USING PIEZOELECTRIC
ACTUATORS

THESIS

Shawn D. Morgenstern, Captain, USAF

AFIT/GAE/ENY/06-M25

DEPARTMENT OF THE AIR FORCE
AIR UNIVERSITY

AIR FORCE INSTITUTE OF TECHNOLOGY

Wright-Patterson Air Force Base, Ohio

AFIT/GAE/ENY/06-M25

Alleviation of Buffet-Induced Vibration Using Piezoelectric Actuators

THESIS

Presented to the Faculty

Graduate School of Engineering and Management

Air Force Institute of Technology

Air University

Air Education and Training Command

In Partial Fulfillment of the Requirements for the

Degree of Master of Science in Aeronautical Engineering

Shawn D. Morgenstern, B.S.

Captain, USAF

February, 2006

APPROVED FOR PUBLIC RELEASE; DISTRIBUTION UNLIMITED.

Alleviation of Buffet-Induced Vibration Using Piezoelectric Actuators

Shawn D. Morgenstern, B.S.

Captain, USAF

Approved:

_____   _____
Robert A. Canfield Ph.D.   date
Thesis Advisor

_____   _____
Donald L. Kunz Ph.D.   date
Thesis Advisor

_____   _____
Major Daniel R. Millman Ph.D.   date
Committee Member

Table of Contents

v

List of Figures

List of Tables

List of Symbols

List of Abbreviations

AFIT/GAE/ENY/06-M25

Abstract

Buffet-induced vibrations have been problematic for aircraft for many years, and can have a disastrous impact when allowed to continue to the point of structural failure. Early attempts at combating harmful vibrations included relatively passive methods such as structural enhancements and leading edge fences used to minimize the strength of vortices. However, modern techniques have shown greater promise. Synthetic jet actuators have demonstrated the capability to significantly decrease vibrational strength by altering the airflow impinging upon a structure. Piezoelectric actuators have also shown great potential. Strategically mounted to the surface of the affected structure, they impart directional strain to reduce the negative effects associated with the strain energy of specific mode shapes. The F-16 ventral fin is representative of an aircraft structure prone to failure when subjected to the buffet field from a Low Altitude Navigation and Targeting Infrared for Night (LANTIRN) pod. However, ventral fin failures pose relatively little risk to the pilot or the aircraft. Therefore, it has great potential as a platform for further investigation into the effectiveness of piezoelectric actuators, which is the subject of this research. In addition, this research represents the foundation of a rare opportunity to test the capability of piezoelectric actuators in flight as an extremely cost-effective alternative to wind tunnel testing. It was sponsored by the Air Force Research Laboratory (AFRL) in collaboration with the United States Air Force (USAF) Test Pilot School (TPS) where actual test flights will be conducted in the near future.

Investigation into the effectiveness of piezoelectric actuators for the F-16 ventral fin began with an accurate finite element model (FEM). The model was tuned and optimized to match published modal parameters and analyzed to determine strain energy profiles for the first five modes of vibration. The three most critical modes were determined through an evaluation of historical flight test data detailing the

relative dominance of each mode and the ventral fin failure history, as well as an evaluation of the aeroelastic characteristics of the fin FEM. Piezoelectric actuators were subsequently designed for the most critical modes and integrated into the FEM using a thermal analogy within MSC.Nastran. They were located within the regions of highest strain energy and aligned with the principal strain vectors in those regions. Finally, the second phase of critical mode selection was completed in an effort to determine the two most suitable modes for future flight testing. Various actuator-fin combinations were individually analyzed using Zona's Aeroservoelasticity (ASE) Module to determine the relative effectiveness of each actuator, and additional flight test data from the actual ventral fin test article were analyzed. The results identified Modes 1, 2 and 4 as the most likely candidates for future testing. In addition, Modes 1 and 4 were found to be the most observable given the instrumentation locations on the actual ventral fin. Finally, the TPS data provided evidence that the natural modes of vibration for the actual ventral fin were significantly different than those predicted by the ventral fin FEM. Additional refinement of the model will be required prior to implementation of the technology.

Alleviation of Buffet-Induced Vibration Using Piezoelectric Actuators

I. Introduction

Engineers and scientists have been devising methods to combat structural vibrations which plague modern high-speed aircraft, but the task has been a challenging one. Often, structural vibration modes are excited as a result of the interaction between turbulent airflow, the differential pressures associated with it, and aircraft structures and control surfaces. This aeroelastic phenomenon is commonly referred to as buffet.

Buffet affects a wide range of aircraft and aircraft structures, but its impact has proved to be particularly troubling for twin-tail fighter aircraft. Shortly after the F-15 was placed in service and many high angle of attack maneuvers had been executed, fatigue cracks were discovered in the vertical tails of multiple aircraft. After repeated temporary fixes, an investigation confirmed tail buffet to be the cause [10, section I.3]. Other twin-tail aircraft such as the F/A-18 and F/A-22 have also experienced buffet-induced structural vibration problems. However, the phenomenon has not been limited to twin-tail aircraft. The F-16 for example, has suffered severe ventral fin damage as a result of buffet. The aircraft has two ventral fins located on the underside of the fuselage slightly aft of the wing trailing edge which provide enhanced lateral directional stability during supersonic flight. Early ventral fins were often subject to partial or complete loss as a result of buffet during flight, but without any noticeable signals to the pilot. Inlet spillage turbulence during high speed rapid decelerations was cited as the primary buffeting source [4, page 9]. During the early 1980's when the F-16 was fitted with LANTIRN pods, additional ventral fin failures were experienced. The LANTIRN pods were mounted on the underside of fuselage, just aft of the inlet as shown in Figure 1.1. The two mounting locations for the LANTIRN

pods placed them directly upstream of the ventral fins. As a result of the turbulent airflow produced by the LANTIRN pods, ventral fin buffet, cracking and failure was experienced. Figure 1.2 shows a failure following the first F-16 flight with LANTIRN pods. Despite a re-design of the ventral fins and supporting structures following the initial failures, the losses continued.

Figure 1.1:   Location of Ventral Fins and LANTIRN Pods

Buffet has been a costly problem, not solely in terms of the expense of repairing and replacing aircraft structural components, but also in terms of the impact it has had on mission availability and performance. In 1998, the cost of repairing and replacing F-15 vertical tails due to fatigue damage was estimated to be approximately $5-6M per year, in addition to the loss of flight readiness to Air Combat Command. In flight, buffet-induced vibrations forced a restriction on the angle of attack and speed at which certain maneuvers could be flown [10, section 1]. Clearly, something had to be done.

Many different approaches were used in an attempt to counter the harmful vibrations, including both passive structural modifications and flow control devices. Passive structural modifications included methods such as reinforcing structural members through the use of brackets, cleats, or doublers [18, page 2]; adding patches to

Figure 1.2:   Ventral Fin Failure

the existing structure to repair existing defects while simultaneously stiffening the structure; and adding damping materials to the design of existing structures. Flow control devices included wing-mounted leading edge modifications for blowing air, and fences used to alter turbulent vortices in such a way as to reduce destructive buffet. More recently, innovative active flow and structural control methods have been developed, and have shown great promise in combating buffet. Synthetic jet actuators have demonstrated the capability to significantly decrease the strength of structural vibrations by altering the turbulent flow field impacting a particular aircraft structure. Piezoelectric actuators have also shown great potential. They can be mounted to the affected surface and actuated via suitable control logic. When a voltage is applied, they impart directional strain to reduce the negative affects associated with the strain energy of specific vibrational mode shapes.

The F-16 ventral fin represents an ideal test structure for further investigation into the effectiveness of synthetic jet and piezoelectric actuators. Although the fin is certainly prone to failure when subjected to the buffet field from a LANTIRN pod,

a failure poses relatively little risk to the pilot or the aircraft. Additionally, if the research is done in cooperation with TPS, it will be an extremely cost-effective and practical alternative to wind tunnel testing. The potential benefits of this research are far-reaching, including reduced maintenance and repair costs and enhanced mission capability for a variety of military aircraft.

1.1 Problem

The research problem described in this thesis was to determine the natural modes of vibration that were the most critical in the buffet response of the F-16 ventral fin, and design a suitable piezoelectric actuator "patch" layout capable of reducing buffet-induced vibration.

1.2 Scope

The research presented in this thesis was an investigation of the techniques used to modify and tune an FEM to match published modal vibration data, as well as the procedures for integrating and modeling piezoelectric actuators within MSC.Nastran using a thermal analogy in which a change in temperature, ΔT, is used to represent an equivalent change in voltage, ΔV. In support of those techniques and procedures, various sources of historical data and the results of several ASE analyses using Zona's ZAERO software were used to determine which vibration modes in the buffet response of F-16 ventral fin are most critical and, thus, the most suitable for application of piezoelectric actuator technology.

1.3 Approach/Methodology

Four distinct tasks were accomplished in support of a solution to the previously defined problem. A ventral fin FEM was obtained, tuned and optimized in order to match published data for the first four modes of vibration. An initial determination of the three most critical vibration modes in the buffet response of the ventral fin was determined through analysis of: historical flight test data, the geometric characteris-

tics of documented ventral fin failures in comparison with strain energy predictions for the FEM, and the aeroelastic characteristics of the FEM using the ZAERO software. Piezoelectric actuator patch layouts were successfully designed via analysis of the strain energy density and principal strain vectors for the optimized model, then integrated into the ventral fin FEM using a thermal analogy within MSC.Nastran. Finally, the second phase of critical mode selection was completed using two separate methods. The ZAERO ASE software module was used to individually analyze the stability of the three most critical modes of vibration within a control loop employing the piezoelectric patch layouts for each mode. Lastly, power spectral density (PSD) plots produced from testing conducted by the USAF TPS on the actual ventral fin test article during the course of this research were reviewed for identification of the two most dominant modes of vibration.

II. Literature Review

The following review provides a discussion of the aeroelastic phenomenon of buffet and its indisputably harmful impact on military aircraft, as well as the modern active structural control technology and techniques which can be employed to prevent it. The definition of several aeroelastic phenomena are covered and compared to that of buffet, and several historical examples are cited in order to provide the reader a clear frame of reference on the nature of the problem. An introduction into the concept of ASE modeling is provided, followed by a discussion of the applicability of a fairly new technology, macro-fiber composite (MFC) actuators, to the problem of vibration alleviation. Finally, a brief introduction to the concept of control system methodology and design is presented. Taken as a whole, this review should provide the reader with a broad overview of the buffet-induced vibration problem, and a clear understanding of the methodology used to develop and implement a solution to the problem.

2.1   Buffet-Induced Vibration on Military Aircraft

Military aircraft are required to perform under a variety of operating conditions, frequently within harsh flight environments, in order to carry out their respective missions. As a result, a variety of adverse aeroelastic phenomena including flutter, limit cycle oscillation (LCO), buzz, and buffet can occur with potentially devastating effects.

While flutter, a condition which occurs when the aerodynamic surfaces of an aircraft are driven to divergent oscillation as a result of unstable interaction with the air stream, is fairly predictable, LCO, buzz and buffet are not [4, page 2]. Consequently, designing aircraft in such a way to avoid LCO, buzz and buffet is a significant challenge. Despite their unpredictability, the characteristics of those phenomenon are still fairly well understood. LCO occurs as a result of "nonlinear aeroelastic interaction between structural dynamic response and unsteady aerodynamic forces" and is characterized by unstable oscillations which increase in magnitude until "stabilized by nonlinear forces at higher amplitude" [4, page 5]. Buzz, a non-linear phenomenon

which is similar to LCO, usually occurs in the transonic flight regime and "is driven by some type of shock-induced separation" [4, page 4]. Buffet, which is the subject of this research, occurs when turbulent airflow interacts with an aerodynamic structure, exciting the vibrational modes of that structure. The large-amplitude vibrations which result can significantly reduce the structure's service life while drastically increasing maintenance and repair costs.

One explanation for the susceptibility of military aircraft to buffet problems is the fact that they are often required to operate throughout vast flight envelopes while performing multiple roles. Many modern military aircraft are considered to be very high performance; they often execute their missions under high g-loading, and at high Mach numbers. Frequenctly, they also employ new materials and fabrication techniques. Older weapon systems often face challenging buffet problems when they are upgraded with structural and aerodynamic enhancements. The combination of extreme performance, extreme operating conditions, and new modifications makes the prevention and elimination of aerodynamic buffet very challenging [4, page 1].

Perhaps the most well-known examples of aerodynamic buffet are those that affect the tails of high-performance twin tail aircraft such as the F-15, F/A-18 and F/A-22. Fatigue damage on the tails of the F-15 was first discovered in 1975, less than one year after the first F-15A was delivered. This discovery prompted an immediate effort to strengthen the structure. Over the course of the next year, additional fatigue cracks were observed and repaired, eventually leading to a major design change in 1976. Still, discovery of new cracks continued. Another major design modification was performed in 1986, followed by continued fatigue cracking [10, section I.3]. In 1988, the Georgia Institute of Technology performed an evaluation of the cause of the fatigue failures at the request of the USAF. They concluded that tail buffet occurring as a result of high angle of attack maneuvers was likely the cause of the fatigue damage. The design changes which had been implemented up to that point were all intended to stiffen the structure, and those changes likely had the effect of repositioning the cracks to the non-stiffened areas of the tails [10, section I.4]. Also,

the internal honeycomb structure of the tails was damaged by corrosion as a result of moisture entering through the cracks. The complicated nature of the procedure used to fix this problem resulted in very large increases in ownership costs. Additionally, oscillation of the vertical tails resulted in oscillating control loads and subsequent restriction of the aircraft's maneuvering flight envelope [10, section I.5].

While the affect of buffet on primary structures such as vertical tails receives a great deal of attention for obvious reasons, the majority of buffet-induced structural fatigue occurs on secondary structures, such as antennae, panels and fins. For example, inlet spillage from the intake of the F-16 was found to cause unacceptable levels of buffet-induced vibration on the Advanced Identification Friend-or-Foe (AIFF) antenna array mounted on the lower inlet lip when the arrays were first introduced [5, page 3]. Fortunately, a successful antenna redesign eliminated the problem. Another example involves the F-16 ventral fin, which is the subject of the research in this thesis.

The F-16 carries two ventral fins on the aft underside of its fuselage for the purpose of enhancing lateral stability during supersonic flight. Early versions of the fin were often destroyed in flight without pilot awareness as a result of inlet spillage turbulence while performing rapid decelerations. Safety-of-flight was not a serious concern, but the failures incurred higher maintenance costs and used up valuable spare fins. In the early 1980's, the aircraft was required to carry two LANTIRN pods on either side of the bottom of the fuselage, just aft of the engine inlet. These locations placed the LANTIRN pods directly upstream of the ventral fins. The first flight with the LANTIRN pods resulted in a complete loss of the right-hand ventral fin as depicted in Figure 1.2, leading to multiple ventral fin and supporting structure redesigns. Flight testing of three improved variants of the fin was conducted by the Royal Netherlands Air Force [33], and eventually a Block 40 fin with stiffer aluminum skins and an aerodynamic "nose cap" was chosen as the preferred spare, with greatly reduced failure rates compared to the original fin design [4, page 9].

Clearly, aerodynamic buffet is a serious problem for military aircraft and one that needs to be addressed. Originally, passive means of combating the problem were employed with marginal effectiveness. Passive flow control techniques included the addition of wing leading edge blowing and wing or fuselage fences. Passive structural modifications were also employed which included the use of passive damping materials within a structure and the reinforcement of structural assemblies by "increasing skin or spar thickness or applying reinforcing members such as brackets, cleats, or doublers" [18, page 2]. Structural patches have also been used. Such patches allowed the user to repair existing defects while simultaneously stiffening the structure [10, section 2]. More recently, active flow and structural control methods have been proposed. Both methods use "smart materials" to either affect the turbulent flow causing structural buffet or dynamically change the properties of the structure under buffet.

2.2 *Active Buffet Alleviation Using Smart Materials*

Beginning in the mid-1990's, reports documenting the effectiveness of active smart material solutions to the problem of buffet alleviation began to surface. In 1995, the Active Control eXperts corporation performed a study in cooperation with the Wright Laboratory to address the feasibility of reducing buffet vibrations in vertical tail aircraft using an active piezoelectric system [12, page 179]. The research was methodically conducted using a four-step process. Employing an F/A-18 vertical tail as their subject structure, they used performance requirements and the buffet disturbance environment to define the functional requirements of the active smart material system, assembled a state space ASE model of the tail, chose the control system architecture, tested the system and assessed its performance [12, page 180]. They found that it was critical in the development of their ASE model to properly include the effects of unsteady aerodynamics. Similarly, they found actuator sizing and placement to be a critical design element. The actuators were distributed in areas of high strain, using between one and five layers per location, to minimize the strain energy in the tail structure [12, page 185]. They used a finite element

model constructed within NASTRAN to characterize the modes of vibration and applied a thermal analogy to model the piezoelectric effect of the actuator elements. After experimenting with a variety of sensor locations, actuators distributions and control schemes, they found that performance increases as high as 70 percent could be obtained with weight penalties less than 8 percent.

In 1995, the National Aeronautics and Space Administration (NASA) Langley Research Center (LaRC) was actively pursuing several projects applying adaptive materials and integrated systems to control aircraft ASE response [23, page 168]. Some of the most widely publicized research was focused on using various active structural control techniques to reduce the effect of buffet generated when vortices produced by the wing leading edge extensions on an F/A-18 Hornet burst and impinge upon the twin tails. Specifically, a 1/6-scale F/A-18 wind-tunnel model was tested in the Transonic Dynamics Tunnel as part of the Actively Controlled Response Of Buffet-Affected Tails (ACROBAT) program. The model was equipped with an active rudder and other aerodynamic devices on the starboard vertical tail as well as piezoelectric actuators on the port vertical tail. The research indicated that:

> by using single-input-single-output (SISO) control laws at gains well below the physical limits of the control effectors, the power spectral density of the root strains at the frequency of the first bending mode of the vertical tail was reduced by as much as 60 percent up to angles of attack of 37 degrees. Root mean square (rms) values of root strain were reduced by as much as 19 percent. [15] [16] [17]

While conducting the research, the buffet on the vertical tails was found to be variable with angle of attack, resulting in a shift in the frequency of the first bending mode. The piezoelectric actuator configuration on the port tail consisted of seven actuator pairs, with three located at the root and four located elsewhere on the tail. The two individual actuators making up each pair were located on opposite sides of the tail and were commanded to strain in opposite directions simultaneously, thus forcing the tail to bend. The open-loop frequency response functions of the vertical tails were experimentally determined and used to build a matrix of transfer functions

between the inputs generated by the control effectors and the outputs measured by strain gages and accelerometers mounted on the tails. The transfer functions were then used in the forward loop of the active control system. Analysis of the results indicated that by using the rudder as a primary actuator, assuming the actuation frequency was increased to include the first two structural frequencies, "the rms of the tail root bending moment could be reduced by as much as 33 percent". Using the piezoelectric strain actuators in conjunction with linear control algorithms, "a 50% reduction in the rms strain at the root of the tail could be achieved at selected flight conditions." [18, page 2]. More recent research has shown a benefit of the piezoelectric actuators over active rudder control in that they are able to maintain their effectivness under any flight condition while active rudder control cannot [18, page 2].

Research efforts focusing on buffet load alleviation through the use of piezo-electric actuators have also resulted in international collaboration. In 1998, Canada, Australia and the United States initiated a project to investigate the feasibility of tail buffet reduction via an active buffet load alleviation system [11, page 29]. In a manner very similar that used by LaRC during the ACROBAT program, the research team instrumented the starboard vertical tail from a non-flying fighter aircraft with an array of piezoelectric actuators, accelerometers and strain gages. The actuators were sized and placed "using an optimization scheme that evaluated the modal strain energy in the tail" [11, page 29]. The accelerometers and strain gages were used to monitor the response of the tail to simulated buffet loads, and deformation was reduced through active control of the piezoelectric actuators using dynamic sensor feedback. Both SISO and multiple-input-multiple-output (MIMO) control laws were evaluated and found to be "similarly effective in reducing the rms strain at the root of the vertical tail where fatigue is know to occur" [11, page 29].

Several active flow and structural control experiments were conducted by the Air Force Research Laboratory (AFRL) in order to evaluate synthetic jet actuator and bonded piezoelectric ceramic actuator technologies in a low-speed wind tunnel. In 2002, a 4-inch diameter pod equipped with synthetic jet actuators was used to

demonstrate that radial injection of air into the air stream was more effective than axial injection at reducing a fatigue damage parameter relating acoustic loads to structural fatigue [30]. In 2003, an 8-inch diameter pod similar in shape to a LANTIRN pod was tested with two General Electric proprietary Dual Bimorph Synthetic Jet (DBSJ) actuators attached to six 3-millimeter orifices machined into the side of the pod at the aft end. At a wind tunnel velocity of 0.5 Mach, a 3 to 5 decibel reduction in the dynamic pressure spectra was detected at a location 3.8 pod diameters aft of the pod [27]. Further research into this technology was conducted by the students and staff of the USAF TPS as part of an ongoing Aeroelastic Load Control (ALC) project. Their test platform consisted of an F-16B aircraft with a dummy LANTIRN pod and an instrumented ventral fin mounted on the right side of the bottom of the fuselage. The dummy LANTIRN pod was modified with an aft-end extension containing six DBSJ actuators controlled via a hand-held PC in the rear cockpit. The ventral fin was an original Block 15 fin selected for its high susceptibility to vibration, and was instrumented with six pressure sensors, two accelerometers and a set of four strain gages. The strain gages were bridged together to produce a single output. The system, as depicted in Figure 2.1, was designed to test the active flow control concepts under investigation by the AFRL in an "airborne wind tunnel" under a variety of flight conditions. Unfortunately, instrumentation limitations prevented positive determination of the effectiveness of the system in reducing buffet-induced ventral fin vibration when the aircraft was configured without external wing-mounted fuel tanks. The test team found that the DBSJs did not significantly reduce the ventral fin vibration when the aircraft was configured with the external tanks. This may have been due to a combination of insufficient volumetric flow from the DBSJs and excessive distance between the LANTIRN pod and the ventral fin [14]. Future work on the ALC project will likely involve additional active flow control testing, as well as active structural control tests developed from the research presented in this thesis.

Without question, active structural control, specifically through the use of smart materials, shows great promise for reducing the adverse effects of buffet on modern

Figure 2.1:   ALC System Used by USAF TPS

military aircraft. The following sections provide additional detail into the methodology used for employing this technology.

2.3   ASE Modeling

Typically, before smart materials can be used in an active structural control application, an ASE model of the structure in question must be constructed and analyzed. Results from an analysis including structural vibration modes as well as aerodynamic and piezoelectric actuator forces can then be used to predict the structural response under an adequate feedback control loop.

Structural models are usually generated by an FEM program such as NASTRAN. An abundance of element types and modeling options make this software ideal for accurate representation of the desired structure. Aerodynamic modeling and integration with the structural model can be performed using a variety of methods and software. For example, Zona's ZAERO software can import "externally computed free vibration solutions" from a variety of FEM sources and integrate them with an aerodynamic model allowing complete aeroelastic design and analysis capability [37]. Finally, an FEM incorporating the piezoelectric actuators used to control the affected structure must be generated. In the case of MSC.Nastran, accurate piezo-

electric modeling can be achieved using a thermal analogy applied to structural plate elements [1, page 29].

In order to validate the ASE model, comparisons with ground and flight test data are performed. Ground vibration test data can be compared with the mode shapes and frequencies predicted by the FEM analysis software, allowing modifications to and optimization of the structural model, as required. Additionally, flight test data can be used to determine structural buffet response for comparison with model predictions.

2.4 Vibration Alleviation Using Macro-Fiber Composites

Modern smart materials are available in a variety of compositions and configurations. When they first started gaining popularity for use in buffet-induced vibration alleviation applications, the material used was of piezoceramic (PZT) composition. It was manufactured into rectangular pieces referred to as "patches". When bonded to a structure, strain from the structure was used by a controller to input a voltage into these PZT patches. The patches responded by producing strain equal and opposite to that at the locations of the structure upon which they were mounted, minimizing the net vibration [28, page 2].

More recently, researchers have developed MFC materials. According to R. Brett Williams, et al.:

> The MFC is a layered, planar actuation device that employs rectangular cross-section, unidirectional PZT fibers embedded in a thermosetting polymer matrix. This active, fiber-reinforced layer is then sandwiched between copper-clad Kapton film layers that have an etched interdigitated electrode pattern. [35, page 1]

MFCs possess considerable advantages over traditional PZT materials. While PZT materials are extremely brittle and require great care during handling and while bonding to a structure, MFCs are highly flexible and durable [31, page 683]. Usually, a large number of PZT actuators are required for "large scale, real world applications" [10, section IV.1]. However, MFC performance exceeds that of PZT materials in terms of forces and displacements produced [31, page 683]. One great benefit of

any piezoelectric material is its ability to act as both a sensor and an actuator. Such a setup is particularly useful when applied to vibration alleviation where additional advantages can be realized during examination of the structure's closed loop stability [31, page 689].

In 2001, LaRC was actively pursuing research with an objective of examining the performance of MFC actuators in alleviating fin buffet. The Evaluation of New Actuators in a Buffet Loads Environment (ENABLE) program found that the actuators performed superbly, with peak values values for power spectral density functions reduced by as much as 85 percent [19, page 10]. Two different MFCs were evaluated using the refurbished 1/6-scale F/A-18 model which had been employed to evaluated previous generation actuator technologies. According to Robert Moses, et al.:

> Two new fins were manufactured. The fin skins consisted of 2 plies of 0.0015-inch think white fiberglass cloth and an epoxy resin. The actuators were placed on the inside surface of the inner ply and cured with the skins using molds and in vacuum. Flexible cables made of copper-clad polyimid film extended from each actuator to the root of the fin to power the actuators during operation. Once cured, the skins were bonded to the foam core, yielding the final construction assembly. [19, page 13]

Ten actuators, five per side, were embedded beneath the fiberglass shells for each fin. Six were placed near each root to alleviate buffeting in the first bending mode and four were distributed near each tip to alleviate buffeting in the first torsion mode [19, page 14].

Logically, proper actuator placement and sizing is important to an effective vibration alleviation system. A preferred method for placing the actuators is to determine areas of high strain density and locate them there, with the PZT fibers aligned with the directions of principal strain. The actuators can also be layered, or stacked, as required to achieve the forces desired to counteract those resulting from buffet vibration [12, page 185]. Additionally, the specific variety of actuators must be chosen. MFC actuators are available in two varieties, with isotropic or orthotropic properties. Isotropic actuators utilize what is referred to as a d_{31} piezoelectric charge
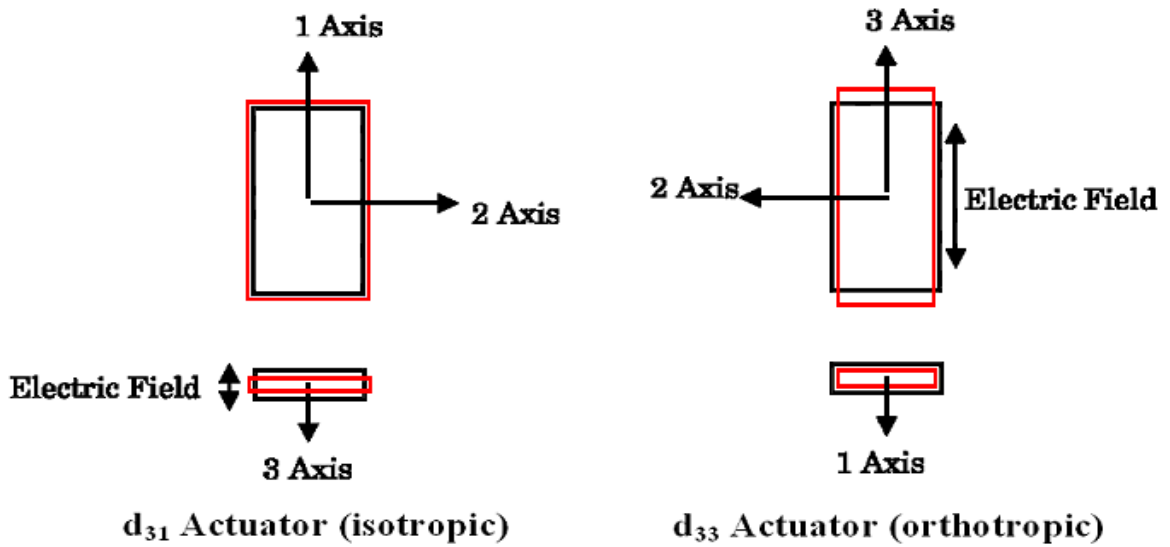
Figure 2.2:   Comparison of Isotropic and Orthotropic Actuators [1, page 27]

constant, while orthotropic actuators utilize a d_{33} charge constant. Both types are shown in Figure 2.2. Note that the undeflected shape of each actuator is represented by the black line, while the red line represents the deflected shape given a voltage input. Also, the 2-axis and 3-axis strains are out of phase for the d_{33} actuator [1, page 27]. As described by Jay Burnham, d_{33} actuators have been shown to outperform d_{31} actuators by a factor of three for a given piezoceramic material and, hence, are recommended for use over the d_{31} variety [1, page 44].

Overall, piezoelectric actuators in general and MFC actuators in particular have shown great promise for use in buffet-induced vibration alleviation applications. The keys to an effective system include proper design and placement of the actuator assembly and required sensors, as well as the design of a suitable controller employing appropriate feedback control techniques [10, section XII].

2.5   Control System Methodology and Design

Prior to beginning the actual design of a suitable controller, selection and placement of appropriate feedback sensors should be determined, and suitable performance objectives and metrics should be defined. After that, the first real task in the design

of a controller is obtaining a mathematical representation of the system to be controlled, also known as the "plant" [10, section XI.6]. According to S. Hanagud, "the plant model can be: an FEM in the configuration space, an FEM in the modal space, an FEM in the state-space, or a transfer function matrix model" [10, section 3]. If acceleration feedback, which Hanagud found to be desirable, is used, then "the desired plant model is the modal space model, or the transfer function matrix model" [10, section 3].

After the plant model has been developed, the controller itself must be designed. If an acceleration feedback control loop is used, it can be set up such that it increases the damping in several vibration modes through the use of a single actuator [10, section VII.2]. The specific details of such a design are discussed in detail by Hanagud [10, section VI.1]. In the buffet alleviation research conducted by LaRC, as documented by Robert Moses, "control laws were designed using frequency domain methods to alleviate buffeting in the first bending and first torsion modes of the fins" [15] [16] [19]. If the modes are well-separated, SISO controllers can be used in conjunction with filtering. Both low-pass and band-pass filtering can be used to ensure that other modes are not excited when feedback is turned on [19, page 17]. Certainly, there are a variety of feasible options. Ideally, plant information would be available for each flight condition at which a structure would be required to fly. Then the control laws could be optimized for each flight condition, providing the best possible continuous solution to the problem of buffet-induced vibration. However, demonstration of the effectiveness of active vibration alleviation is possible by using one time-invariant, fixed-parameter, SISO control law for all flight conditions [18, page 3].

Typical components of the control systems documented by Moses included an analog-to-digital converter, a digital controller and a digital-to-analog converter [15, page 94] [16]. Fortunately, time delays inherent in such systems can be taken advantage of within the control laws. Specifically, "by lagging accelerations by ninety degrees of phase, the commanded motion of the actuator may provide damping to reduce the buffeting" of the structure [15, page 94] [16]. Moses also stated that for

piezoelectric actuators, "the digital controller and the distance between the amplifiers and the actuators were the major contributors to the phase lags" [15, page 94] [16].

A simple control scheme used within the ZAERO ASE module during the course of this research is discussed in Section 3.6.

III. Theoretical Background

This chapter presents a summary of the theoretical framework required for the prediction and analysis of the vibrational modes of the F-16 ventral fin, optimization of the modal characteristics to match published data, analysis of the aeroelastic characteristics of the FEM within ZAERO, determination of the structural strain energy and principal strain vectors, design of the piezoelectric actuators within MSC.Nastran using a thermal analogy, and modeling of the fin and actuators within a closed loop control system while performing a flutter analysis using the ZAERO ASE module.

Section 3.1 presents a summary of the method used to calculate a system's natural modes. In section 3.2, the optimization theory used to refine the natural modes of the ventral fin FEM to be representative of published data is introduced. Given an accurate FEM, the ZAERO flutter analysis material covered in section 3.3 becomes useful, as such an analysis can be used to predict the onset of a flutter condition as well as the associated modal participation. Although the ventral fin problem is related to buffet, the information obtained is still useful as it provides an understanding of the aeroelastic behavior of the fin, leading to a determination of the most critical modes. Section 3.4 introduces the theory behind determination of structural strain energy and principal strain vectors, which are required for choosing an optimal location for piezoelectric actuator placement. Section 3.5 details the method used to model the piezoelectric actuators, including voltage application, within the FEM using a thermal analogy. Finally, Section 3.6 presents a summary of the theory used to model the fin and actuators within a closed loop control system while performing a flutter analysis using the ZAERO ASE module.

3.1   Natural Modes of Vibration

The undamped natural modes of vibration for the ventral fin FEM are calculated within NASTRAN using the standard methodology for multiple degree-of-freedom systems. A summary of the methodology begins with Newton's second law, $F = ma$,

where F is force, m is mass and a is acceleration. For a multi-element structure with multiple degrees of freedom, this equation can be rewritten as

$$[\mathbf{M}]\{\ddot{\mathbf{D}}\} + [\mathbf{C}]\{\dot{\mathbf{D}}\} + [\mathbf{K}]\{\mathbf{D}\} = \{\mathbf{R}^{ext}\} \tag{3.1}$$

where $[\mathbf{M}]$, $[\mathbf{C}]$, and $[\mathbf{K}]$ are the mass, damping and stiffness matrices, $\{\mathbf{D}\}$ is a vector of the nodal degrees of freedom, and $\{\mathbf{R}^{ext}\}$ is a vector of externally applied loads [3, page 376]. However, for undamped free vibration the damping is assumed to be zero and there are no externally applied loads. Consequently, equation (3.1) reduces to

$$[\mathbf{M}]\{\ddot{\mathbf{D}}\} + [\mathbf{K}]\{\mathbf{D}\} = \{\mathbf{0}\} \tag{3.2}$$

Additionally, the nodal displacements and accelerations associated with free vibration may be written as

$$\{\mathbf{D}\} = \{\bar{\mathbf{D}}\}\sin\omega t \qquad \{\ddot{\mathbf{D}}\} = -\omega^2\{\bar{\mathbf{D}}\}\sin\omega t \tag{3.3}$$

where $\{\bar{\mathbf{D}}\}$ represents the variation of nodal displacements from static equilibrium. The equations are formulated in this manner since the calculation of natural frequencies within a linear problem is independent of the nodal equilibrium positions [3, page 385]. Combining equations (3.2) and (3.3) yields the eigenproblem for undamped free vibration of a multi-degree-of-freedom system,

$$([\mathbf{K}] - \omega^2[\mathbf{M}])\{\bar{\mathbf{D}}\} = \{\mathbf{0}\} \tag{3.4}$$

where ω^2 is an eigenvalue and ω is one of the natural frequencies of vibration. For each eigenvalue and natural frequency, there is a corresponding eigenvector, $\{\bar{\mathbf{D}}\}$ which represents the "shape" of that particular mode of vibration. The solutions to

equation (3.4) are computed within NASTRAN, providing the natural frequencies of vibration for the ventral fin FEM as well as the corresponding mode shapes.

3.2 FEM Model Optimization

Design optimization is used in order to modify the design of a complex structure such as the ventral fin FEM, while specifying the design variables, design constraints and a "cost function" or performance index. NASTRAN employs sensitivity analysis techniques in order to determine changes in structural response quantities for infinitesimal changes in the design parameters [20, section 4.4]. A sensitivity matrix is formed and the elements of the matrix are defined as

$$S_{ij} = \frac{\partial R_i}{\partial X_j} \tag{3.5}$$

where S_{ij} is the i,j term within the sensitivity matrix, R_i is the ith response and X_j is the jth design variable [21, section 11.10]. Therefore, each sensitivity matrix term is equivalent to the slope of the curve for a specific response versus a specific design variable.

The surface elements of the ventral fin FEM are characterized by four regions of different skin thickness. Those skin thicknesses are employed as four of the design variables within the optimization routine. Additional design variables include the spring constants for each of three sets of tuning springs which were added to the model along the fuselage mounting surface. One set is composed of springs attached to nodes on the front of the mounting surface relative to the central mounting bracket; one set is composed of springs attached to two of the nodes comprising the mounting bracket itself; and the final set is composed of springs attached to the nodes on the rear of the mounting surface relative to the bracket. The design constraints are the frequency windows for Modes 1 through 4, as defined by previously published Block 15 GVT and Block 30 NASTRAN model data. Section 4.1.3 provides additional detail on both the design variables and the design constraints.

Beginning with specified starting values for each of the design variables, NASTRAN uses iterative numerical techniques in combination with the sensitivity matrix in order to apply changes to the design variables which bring the responses within the bounds specified by the design constraints while simultaneously minimizing the cost function. In the case of the ventral fin FEM, the cost function minimized is a measure of change from the original design configuration. Minimal change is desired in the interest of preserving the original model as much as possible. The cost function, F_c, used for optimization of the ventral fin FEM is defined as

$$F_c = 1.0 + \sqrt{(x_1 - 1.0)^2 + (x_2 - 1.0)^2 + \cdots + (x_7 - 1.0)^2} \qquad (3.6)$$

where x_k are the normalized design variables which can range in value from 0.01 to 100.0. Therefore, the closer they are in value to 1.0, the lower the value of the cost function. Additional details of the specific design optimization techniques used by MSC.Nastran are described in greater depth in the MSC.Nastran Design Sensitivity and Optimization Users Guide [22].

3.3 Zona ZAERO Flutter Analysis

As previously noted, the F-16 ventral fin issue is not related to flutter, but buffet. Unfortunately, an accurate representation of the buffet field created by the LANTIRN pod was not available during the execution of this research, nor were the resources required to accurately create an original buffet model. Therefore, in order enhance the process of determining which vibration modes of the fin were most critical, Zona's ZAERO software was used to conduct flutter analyses. This provided an understanding of the aeroelastic behavior of the fin, specifically the modal interaction, within the flight regions of interest. The ZAERO software module used for the basic flutter analysis was the ZONA6 Unsteady Subsonic Aerodynamics code. A summary of the flutter solution derivation including the ZONA6 linear formulation, aerodynamic influence coefficient (AIC) matrix formulation, and the specific solu-

tion methods employed, as written in the Zona ZAERO Theoretical Manual [36] and summarized by Raymond Toth [32], is presented in this section. Note that the solution methods presented assume a complete aircraft model with both wing and body elements. In the case of the ventral fin FEM, no body elements were present.

3.3.1 ZONA6 Linear Formulation.

ZONA6 solves the linearized small disturbance equation for subsonic flow

$$\left(1 - M_\infty^2\right)\Phi_{xx} + \Phi_{yy} + \Phi_{zz} - 2\frac{M_\infty}{a_\infty}\Phi_{xt} - \frac{1}{a_\infty^2}\phi_{tt} = 0 \tag{3.7}$$

by assuming a solution of the form

$$\Phi = \phi_0 + \phi_1 \qquad \phi_1 = \phi e^{iwt} \tag{3.8}$$

where

$\phi_1 \ll \phi_0$

M_∞ \qquad is the freestream Mach number

Φ \qquad is the total velocity potential

ϕ_0 \qquad is the steady potential

ϕ_1 \qquad is the unsteady potential

ϕ \qquad is the reduced frequency domain potential

ω \qquad is the oscillation frequency

The steady and unsteady components of equation (3.7) are separated by substituting equations (3.8) into (3.7) and collecting like terms to yield

$$\left(1 - M_\infty^2\right)\phi_{0xx} + \phi_{0yy} + \phi_{0zz} = 0 \tag{3.9}$$

$$\left(1 - M_\infty^2\right)\phi_{1xx} + \phi_{1yy} + \phi_{1zz} - \frac{2M_\infty}{a_\infty}\phi_{1xt} - \frac{1}{a_\infty^2}\phi_{1tt} = 0 \tag{3.10}$$

where equation (3.9) is the steady linearized small disturbance equation and equation (3.10) is the unsteady linearized small disturbance equation. Equation (3.10) is solved after incorporating the structural mode shapes from the NASTRAN model. A set of unsteady pressure coefficients, C_p, is generated using the steady mean flow conditions, unsteady perturbation quantities, reduced frequency, and the mode shapes and their derivatives. The unsteady C_p's are the basis for the AIC matrix relating deformations to aerodynamic forces.

3.3.2 Aerodynamic Influence Coefficient Matrix Formulation. In order to generate the flutter solution, a modal AIC relating structural mode shapes to unsteady aerodynamic forces must be calculated. By multiplying the area of each box of a wing-like component by the unsteady pressure on that box, the normal force may be computed. The calculations for body-like components are significantly more complicated. However, the quantities required to complete them are all available from the ZONA6 linear calculations. After expanding the normal force vector to include the force and moment components, a square matrix relating the structural mode shapes to the aerodynamic forces is constructed as

$$\{\mathbf{L}_h\} = q_\infty [AIC]\{\mathbf{h}\} \tag{3.11}$$

where

$$[AIC] = [\bar{\mathbf{B}}][NIC]^{-1}[\bar{\mathbf{F}}] + [\bar{\mathbf{D}}] \tag{3.12}$$

$$\{\mathbf{h}\} = [\mathbf{T}]\{x\} \tag{3.13}$$

$$\{\mathbf{L}_h\} = [\mathbf{T}][\Phi]\{\mathbf{F}_a\} \tag{3.14}$$

q_∞ is the freestream dynamic pressure

$[NIC]$ is the normal velocity influence coefficient matrix

$\{\mathbf{h}\}$ is the structural deformation at each aerodynamic box

$\{\mathbf{L}_h\}$ is the resultant aerodynamic force vector at each

                aerodynamic box due to $\mathbf{h}$

$[\mathbf{T}]$ is the spline matrix relating aerodynamic

                degrees of freedom to structural degrees of freedom

$[\Phi]$ is the modal transformation matrix

and $[\bar{\mathbf{B}}]$, $[\bar{\mathbf{F}}]$ and $[\bar{\mathbf{D}}]$ are all complex matrices containing the steady mean flow conditions and normal vector components, and are functions of the reduced frequency. Equation (3.12) is defined for the degrees of freedom at the aerodynamic grid points and must be interpolated to the structural grid points using a spline matrix, then transformed to modal coordinates before it is included in the g-method eigenvalue equation.

3.3.3 Flutter Solution Methods.   Three basic methods are used to calculate the flutter boundary from the aeroelastic equations of motion: the k, $p\text{-}k$, and g-methods. Each method applies the assumption that at the flutter boundary, one of the natural vibration modes of the system will become neutrally stable and produce simple harmonic motion while the other modes remain stable. Excluding external forces since flutter analysis is interested in finding the self-excited response of the structure, the general system of equations for flutter in the Laplace domain may be written as

$$[s^2\mathbf{M} + s\mathbf{C} + \mathbf{K}]\mathbf{q} = \mathbf{F}_a \tag{3.15}$$

where

$\mathbf{M} = \Phi^T\, m\, \Phi$ is the generalized mass matrix

$\mathbf{K} = \Phi^T\, k\, \Phi$ is the generalized stiffness matrix

$\mathbf{C} = \Phi^T\, c\, \Phi$ is the generalized viscous damping matrix

q	are the generalized coordinates
$\mathbf{F}_a$	are the aerodynamic forces produced by structural deformation

The equation for the natural modes of the ventral fin in terms of generalized coordinates,

$$x(t) = \Phi q(t) \tag{3.16}$$

where Φ is the modal transformation matrix, is combined with equations (3.11) through (3.14). Substituting $\mathbf{F}_a$ from equation (3.15) while omitting the viscous damping term for simplicity, the flutter matrix equation becomes

$$\left[s^2 \mathbf{M} + \mathbf{K} - q_\infty \mathbf{Q}\left(\frac{sL}{V}\right) \right] \mathbf{q} = 0 \tag{3.17}$$

where $\mathbf{Q}\left(\frac{sL}{V}\right)$ is the generalized aerodynamic force matrix in the Laplace domain. Equation (3.17) is transformed to the frequency domain by applying the simple harmonic motion assumption and becomes

$$[-\omega^2 \mathbf{M} + \mathbf{K} - q_\infty \mathbf{Q}(ik)]\mathbf{q} = 0 \tag{3.18}$$

The aerodynamic force matrix becomes the AIC matrix, $\mathbf{Q}(ik)$, which is a function of the reduced frequency, $k = \frac{\omega b}{V}$, where b is half of the fin root chord length and V is the velocity of the fin. Equation (3.18) is the basic form of the flutter equation which is solved for the flutter roots. Additional details pertaining to each of the three specific flutter solution methods may be found in the ZAERO Theoretical Manual [36].

3.4 Structural Strain Energy and Principal Strain Vectors

Evaluation of the strain energy within the FEM begins with the determination of strain and stress at each of the nodal locations throughout the model. By definition, normal strain, ϵ, is a change in length divided by the original length and shear strain, γ, is the amount of change in a right angle. In three dimensions, these relations may be summarized as

$$\epsilon_x = \frac{\partial u}{\partial x} \qquad \epsilon_y = \frac{\partial v}{\partial y} \qquad \epsilon_z = \frac{\partial w}{\partial z}$$

$$\gamma_{xy} = \frac{\partial u}{\partial y} + \frac{\partial v}{\partial x} \qquad \gamma_{yz} = \frac{\partial v}{\partial z} + \frac{\partial w}{\partial y} \qquad \gamma_{zx} = \frac{\partial w}{\partial x} + \frac{\partial u}{\partial z} \qquad (3.19)$$

or in matrix form

$$\begin{Bmatrix} \epsilon_x \\ \epsilon_y \\ \epsilon_z \\ \gamma_{xy} \\ \gamma_{yz} \\ \gamma_{zx} \end{Bmatrix} = \begin{bmatrix} \frac{\partial}{\partial x} & 0 & 0 \\ 0 & \frac{\partial}{\partial y} & 0 \\ 0 & 0 & \frac{\partial}{\partial z} \\ \frac{\partial}{\partial y} & \frac{\partial}{\partial x} & 0 \\ 0 & \frac{\partial}{\partial z} & \frac{\partial}{\partial y} \\ \frac{\partial}{\partial z} & 0 & \frac{\partial}{\partial x} \end{bmatrix} \begin{Bmatrix} u \\ v \\ w \end{Bmatrix} \qquad (3.20)$$

where ϵ_i is the normal strain in the i direction, γ_{ij} is the shear strain in the ij plane, and u, v, and w are displacements in the x, y, and z-directions, respectively. The stress at each node can then be determined using the Hooke's Law relationship in matrix form, $\{\sigma\} = [\mathbf{E}]\{\epsilon\}$, where $\{\sigma\}$ is a vector of nodal stresses (force per unit area) and $[\mathbf{E}]$ is the constitutive matrix relating stress to strain.

In order to determine the strain, and therefore the stress, at any location within the model, appropriate shape functions are used to interpolate displacements from the surrounding nodes. In equation form

$$\{\mathbf{u}\} = [\mathbf{N}]\{\mathbf{D}\} \qquad (3.21)$$

where $\{\mathbf{u}\} = \lfloor u \quad v \quad w \rfloor^T$ is an array of displacements, $[\mathbf{N}]$ is the shape function matrix and $\{\mathbf{D}\}$ contains the nodal displacement degrees of freedom. Strains are determined from those displacements according to equation (3.20) and stresses are once again determined using the Hooke's Law relationship.

The theory which is applied to determine structural strain energy in the ventral fin FEM may be summarized by considering a unit volume of a certain material which is subject to deformation as shown by Robert Cook, et. al [3, section 4.4]. The energy that must be supplied to deform the material may be written as

$$U_0 = \int \{\sigma\}^T \{d\epsilon\} \tag{3.22}$$

or

$$U_0 = \int \sigma_x d\epsilon_x + \int \sigma_y d\epsilon_y + \int \sigma_z d\epsilon_z + \int \tau_{xy} d\gamma_{xy} + \int \tau_{yz} d\gamma_{yz} + \int \tau_{zx} d\gamma_{zx} \tag{3.23}$$

where U_0 is the strain energy per unit volume, σ_i is the normal stress in the i direction, ϵ_i is the normal strain in the i direction, τ_{ij} is the shear stress in the ij plane, and γ_{ij} is the shear strain in the ij plane. Combining the Hooke's Law relationship with equation (3.22) and completing the integration yields

$$U_0 = \frac{1}{2} \{\sigma\}^T \{\epsilon\} = \frac{1}{2} \{\epsilon\}^T [\mathbf{E}] \{\epsilon\} \tag{3.24}$$

Equation (3.24) may be applied to any location within the model using the stress and strain for that location. Finally, the equation may be numerically integrated across a specific volume of the model to give the total strain energy for that volume according to:

$$U = \int U_0 dV = \int \left(\frac{1}{2} \{\epsilon\}^T [\mathbf{E}] \{\epsilon\} \right) dV \tag{3.25}$$

3-10

The principal strain vectors exist on perpendicular planes, and are obtained for each skin element by applying standard mathematical equations which assume that the x-y coordinate axes are in the plane of the surface of each element. The principal angles, θ_p, are calculated using

$$\tan 2\theta_p = \frac{\gamma_{xy}}{\epsilon_x - \epsilon_y} \tag{3.26}$$

and the magnitudes of the principal strains are calculated using

$$\epsilon_{1,2} = \frac{\epsilon_x + \epsilon_y}{2} \pm \sqrt{\left(\frac{\epsilon_x - \epsilon_y}{2}\right)^2 + \left(\frac{\gamma_{xy}}{2}\right)^2} \tag{3.27}$$

Coordinate transformations are applied as required to ensure the principal strains for each location are compared using a common coordinate system.

3.5   *Development of Piezoelectric Actuator Model*

Although NASTRAN is well suited to the task of developing a model of the ventral fin and optimizing it, as discussed in section 3.2, it does not have the ability to directly define piezoelectric attributes or apply a particular voltage to an element within the model. Consequently, a suitable workaround for modeling the piezoelectric actuators within NASTRAN has to be implemented. The method chosen employs a thermal analogy.

NASTRAN does allow for definition of thermal attributes for the elements within an FEM. Consequently, if a reliable and accurate analogy can be developed to relate voltage changes to thermal changes, it can be applied to newly defined elements used to represent piezoelectric actuators attached to the skin elements of the ventral fin FEM. Development of the analogy begins with the basic Hooke's Law equation, $\sigma = E\epsilon$, where σ is stress, E is Young's modulus (force per unit area), and ϵ is strain. Since material strains can be produced by a change in temperature, the previous equation can also be written as $\sigma = -E\alpha\Delta T$, or in matrix form

$$\begin{Bmatrix} \sigma_x \\ \sigma_y \end{Bmatrix} = - \begin{bmatrix} E_{11} & E_{12} \\ E_{12} & E_{22} \end{bmatrix} \begin{Bmatrix} \alpha_x \\ \alpha_y \end{Bmatrix} \Delta T \tag{3.28}$$

where for an isotropic material,

$$E_{11} = E_{22} = \frac{E}{1 - \nu^2} \qquad E_{12} = \frac{E\nu}{1 - \nu^2} \tag{3.29}$$

and where α is the coefficient of thermal expansion, ΔT is the change in temperature, and ν is Poisson's ratio. The negative sign in the equation is used to maintain the standard sign convention, with positive and negative stresses being associated with tension and compression respectively.

In the same manner that temperature and a coefficient of thermal expansion can be used to calculate strains and stresses in a material affected by temperature changes, the piezoelectric equivalent of the thermal equations can be also be used to calculate the strains and stresses in a piezoelectric material with an applied voltage [9]. In this case the piezoelectric material properties, e, take the place of the thermal coefficients and the electric field, E, replaces the temperature: $\sigma = -e\bar{E}$, or in matrix form

$$\begin{Bmatrix} \sigma_x \\ \sigma_y \end{Bmatrix} = - \begin{Bmatrix} e_{33} \\ e_{31} \end{Bmatrix} \bar{E} \tag{3.30}$$

where

$$\bar{E} = \frac{\Delta V}{t} \tag{3.31}$$

and e_{ij} are the stress-based piezoelectric coupling terms for the applied voltage, ΔV, and thickness, t, of the piezoelectric material. Equating the stress vectors in equations (3.28) and (3.30) produces the following relation.

$$\begin{bmatrix} E_{11} & E_{12} \\ E_{12} & E_{22} \end{bmatrix} \begin{Bmatrix} \alpha_x \\ \alpha_y \end{Bmatrix} \Delta T = \begin{Bmatrix} e_{33} \\ e_{31} \end{Bmatrix} \frac{\Delta V}{t} \tag{3.32}$$

By setting $\Delta T = \Delta V$, desired changes in voltage for the piezoelectric elements can be directly input into the FEM code via the thermal analogy as changes in temperature of identical magnitude. As a result, the equality may be rewritten as

$$\begin{Bmatrix} \alpha_x \\ \alpha_y \end{Bmatrix} = E^{-1} \begin{Bmatrix} e_{33} \\ e_{31} \end{Bmatrix} \frac{1}{t} \tag{3.33}$$

and further simplified to

$$\begin{Bmatrix} \alpha_x \\ \alpha_y \end{Bmatrix} = \begin{Bmatrix} d_{33} \\ d_{31} \end{Bmatrix} \frac{1}{t} \tag{3.34}$$

where d_{33} and d_{31} are piezoelectric strain coupling terms in the fiber and electrode directions, respectively. By using the actual piezoelectric properties (strain coupling terms) for the proposed brand of actuators [29], it is then possible to generate analogous thermal expansion coefficients for use within NASTRAN according to equation (3.34). It is important to note that the relations developed above apply to P1, F1, and S1-type actuators (but not the P2-type) available from the Smart Material corporation [26]. The P2-type actuator will not be used on the actual ventral fin.

3.6   Zona ZAERO ASE Analysis

The ZAERO ASE module was used in the interest of comparing the effectiveness of the actuator patches under a closed loop control system. It was integrated with the flutter analysis and predictions were obtained after the required control parameters and components were defined. This section presents a theoretical summary of the methodology employed by the ASE module, and was taken from ZAERO Theoretical Manual [36].

3.6.1 Aeroelastic Model. The time-domain ASE model is constructed from the separate models of the aeroelastic plant, the sensing and actuation models, and the control system, all expressed in state-space form. In the aeroelastic model, each modal coordinate is represented by two states: the modal displacement and its velocity. The state-space aeroelastic equation of motion is

$$\{\dot{\mathbf{x}}_{ae}\} = [\mathbf{A}_{ae}]\{\mathbf{x}_{ae}\} + [\mathbf{B}_{ae}]\{\mathbf{u}_{ae}\} \tag{3.35}$$

where

$$\{\mathbf{x}_{ae}\} = \begin{Bmatrix} \xi \\ \dot{\xi} \\ x_a \end{Bmatrix} \qquad \{\mathbf{u}_{ae}\} = \begin{Bmatrix} \delta_c \\ \dot{\delta}_c \\ \ddot{\delta}_c \end{Bmatrix} \tag{3.36}$$

$[\mathbf{A}_{ae}]$ and $[\mathbf{B}_{ae}]$ are aeroelastic state-space matrices, $\{\mathbf{x_{ae}}\}$ is the aeroelastic state vector, $\{\mathbf{u_{ae}}\}$ is the aeroelastic input vector, $\{\xi\}$ is a vector of generalized displacements, $\{x_a\}$ is a vector of the aerodynamic lag states and $\{\delta_c\}$ is a vector of control surface deflection commands.

The outputs of the aeroelastic plant are sensor readings, and are assumed to be linear combinations of the state response. The combinations are defined by the modal displacement vector at the sensor location. In general, displacement, velocity and acceleration sensor readings can be expressed by

$$\{\mathbf{y}_{ae}\} = [\mathbf{C}_{ae}]\{\mathbf{x}_{ae}\} + [\mathbf{D}_{ae}]\{\mathbf{u}_{ae}\} \tag{3.37}$$

where $[\mathbf{C}_{ae}]$ and $[\mathbf{D}_{ae}]$ are aeroelastic state-space matrices.

3.6.2 Actuator Model. The dynamic model of the actuator driving the ith control surface is specified by a transfer function having the form

$$\frac{\delta_{c_i}(s)}{u_{ac_i}(s)} = \frac{a_{i3}}{s^3 + a_{i1}s^2 + a_{i2}s + a_{i3}} \tag{3.38}$$

where u_{ac_i} is the servo-commanded (actuator input) control surface deflection. For a system with more than one actuator, the state-space model of all the actuators is arranged so that the total actuator state vector, $\{\mathbf{x}_{ac}\}$, equals the input vector, $\{\mathbf{u}_{ae}\}$, of equation (3.35). The assembled actuator state-space equation is thus formed as

$$\{\dot{\mathbf{x}}_{ac}\} = [\mathbf{A}_{ac}]\{\mathbf{x}_{ac}\} + [\mathbf{B}_{ac}]\{\mathbf{u}_{ac}\} \tag{3.39}$$

The augmentation of $\{\mathbf{x}_{ae}\}$ of equation (3.35) to include the actuator states $\{\mathbf{x}_{ac}\}$ yields

$$\{\dot{\mathbf{x}}_p\} = [\mathbf{A}_p]\{\mathbf{x}_p\} + [\mathbf{B}_p]\{\mathbf{u}_p\} \tag{3.40}$$

where

$$\{\mathbf{x}_p\} = \begin{Bmatrix} \mathbf{x}_{ae} \\ \mathbf{x}_{ac} \end{Bmatrix} \qquad [\mathbf{A}_p] = \begin{bmatrix} \mathbf{A}_{ae} & \mathbf{B}_{ae} \\ \mathbf{0} & \mathbf{A}_{ac} \end{bmatrix} \qquad [\mathbf{B}_p] = \begin{bmatrix} \mathbf{0} \\ \mathbf{B}_{ac} \end{bmatrix} \tag{3.41}$$

The output equation becomes

$$\{\mathbf{y}_p\} = [\mathbf{C}_p]\{\mathbf{x}_p\} \tag{3.42}$$

where

$$[\mathbf{C}_p] = [\mathbf{C}_{ae} \quad \mathbf{D}_{ae}] \tag{3.43}$$

3.6.3 Control System Model. The control system is modeled as an interconnection of three types of basic control elements in addition to a variable gain matrix. The interconnections within the control elements and between them and the

aeroelastic system can be either fixed or formed through the variable gain matrix. The three types of elements used are: SISO elements specified as transfer functions, MIMO elements defined in state-space, and zero-order junctions.

A SISO control element is defined by a proper transfer function, $T_{se,i}(s)$, which is then realized in state-space within the ASE module. A general transfer function from the input, $u_{se,i}(s)$, to the output, $y_{se,i}(s)$, is expressed by a ratio of polynomials in s as

$$T_{se,i}(s) = \frac{y_{se,i}(s)}{u_{se,i}(s)} \frac{b_{0,i}s^n + b_{1,i}s^{n-1} + \cdots + b_{n,i}}{s^n + a_{1,i}s^{n-1} + \cdots + a_{n,i}} \tag{3.44}$$

The controller canonical form is

$$\{\dot{\mathbf{x}}_{se,i}\} = [\mathbf{A}_{se,i}] \{\mathbf{x}_{se,i}\} + \{\mathbf{B}_{se,i}\} u_{se,i}$$
$$\mathbf{y}_{se,i} = [\mathbf{C}_{se,i}] \{\mathbf{x}_{se,i}\} + \mathbf{D}_{se,i} u_{se,i} \tag{3.45}$$

where

$$[\mathbf{A}_{se,i}] = \begin{bmatrix} 0 & 1 & & 0 \\ \vdots & & \ddots & \\ 0 & 0 & & 1 \\ -a_{n,i} & -a_{n-1,i} & \cdots & -a_{1,i} \end{bmatrix} \qquad \{\mathbf{B}_{se,i}\} = \begin{Bmatrix} 0 \\ \vdots \\ 0 \\ 1 \end{Bmatrix}$$

$$[\mathbf{C}_{se,i}] = [(b_{n,i} - b_{0,i}a_{n,i}) \quad (b_{n-1,i} - b_{0,i}a_{n-1,i}) \quad \cdots \quad (b_{1,i} - b_{0,i}a_{1,i})]$$

$$\mathbf{D}_{se,i} = b_{0,i} \tag{3.46}$$

The number of states in $\{\mathbf{x}_{se,i}\}$ is equal to the order n of the denominator polynomial in equation (3.44).

A MIMO state-space control element is defined by its order (number of states), the number of inputs and outputs, and the associated state-space dynamics and output matrices. The equations of a MIMO state-space element are

$$\{\dot{\mathbf{x}}_{me,i}\} = [\mathbf{A}_{me,i}]\{\mathbf{x}_{me,i}\} + [\mathbf{B}_{me,i}]\{\mathbf{u}_{me,i}\}$$
$$\{\mathbf{y}_{me,i}\} = [\mathbf{C}_{me,i}]\{\mathbf{x}_{me,i}\} + [\mathbf{D}_{me,i}]\{\mathbf{u}_{me,i}\}$$

$$(3.47)$$

Note that a special case of equation (3.47) is a SISO element specified in the state-space format.

Finally, a zero-order element is a special case of the MIMO element which is defined by its number of inputs and number of outputs. This is a junction element in which every output is a weighted sum of the inputs. The element equation is

$$\{\mathbf{y}_{je,i}\} = [\mathbf{D}_{je,i}]\{\mathbf{u}_{je,i}\} \qquad (3.48)$$

where the elements of $[\mathbf{D}_{je,i}]$ are the various weights, which can be positive, negative or zero.

The overall control system is constructed as an interconnection of the above defined control elements and the variable gain matrix. To build the interconnection, all of the control elements are combined into one state-space model,

$$\{\dot{\mathbf{x}}_e\} = [\mathbf{A}_e]\{\mathbf{x}_e\} + \begin{bmatrix} \mathbf{B}_{e_1} & \mathbf{B}_{e_2} \end{bmatrix} \begin{Bmatrix} \mathbf{u}_{e_1} \\ \mathbf{u}_{e_2} \end{Bmatrix}$$
$$\begin{Bmatrix} \mathbf{y}_{e_1} \\ \mathbf{y}_{e_2} \end{Bmatrix} = \begin{bmatrix} \mathbf{C}_{e_1} \\ \mathbf{C}_{e_2} \end{bmatrix} \{\mathbf{x}_e\} + \begin{bmatrix} \mathbf{D}_{e_{11}} & \mathbf{D}_{e_{12}} \\ \mathbf{D}_{e_{21}} & \mathbf{D}_{e_{22}} \end{bmatrix} \begin{Bmatrix} \mathbf{u}_{e_1} \\ \mathbf{u}_{e_2} \end{Bmatrix}$$

$$(3.49)$$

where $\mathbf{u}_{e_1}$ and $\mathbf{y}_{e_1}$ are the inputs and outputs which are interconnected by variable gains or connected to the aeroelastic plant, and $\mathbf{u}_{e_2}$ and $\mathbf{y}_{e_2}$ are the inputs and outputs of equivalent dimension which are involved in fixed interconnections. After the fixed connections are applied, the associated inputs and outputs are eliminated from the

equations of motion. The fixed connections are employed by substituting the terms in $\{\mathbf{y}_{e_2}\}$ of the output equation for the respective terms in $\{\mathbf{u}_{e_2}\}$ in the dynamic part of equation (3.49). The resulting state-space control equations are

$$\{\dot{\mathbf{x}}_c\} = [\mathbf{A}_c]\{\mathbf{x}_c\} + [\mathbf{B}_c]\{\mathbf{u}_c\}$$
$$\{\mathbf{y}_c\} = [\mathbf{C}_c]\{\mathbf{x}_c\} + [\mathbf{D}_c]\{\mathbf{u}_c\} \tag{3.50}$$

where $\{\mathbf{x}_c\} = \{\mathbf{x}_e\}$, $\{\mathbf{u}_c\} = \{\mathbf{u}_{e_1}\}$ and $\{\mathbf{y}_c\} = \{\mathbf{y}_{e_1}\}$. The model represented by equation (3.50) and its parameters are independent of the structural and aerodynamic variables and thus are unchanged in repeated analyses with various structural, aerodynamic and control-gain parameters.

3.6.4   The ASE Model.   The ASE Model is obtained by connecting the aeroelastic model represented by equations (3.40) and (3.42) with the control system represented by equation (3.50) through fixed and variable gain connections. The resulting model is

$$\{\dot{\mathbf{x}}_v\} = [\mathbf{A}_v]\{\mathbf{x}_v\} + [\mathbf{B}_v]\{\mathbf{u}_v\}$$
$$\{\mathbf{y}_v\} = [\mathbf{C}_v]\{\mathbf{x}_v\} + [\mathbf{D}_v]\{\mathbf{u}_v\} \tag{3.51}$$

where

$$\{\mathbf{x}_v\} = \begin{Bmatrix} \mathbf{x}_p \\ \mathbf{x}_c \end{Bmatrix} \tag{3.52}$$

The ASE loop is closed by relating the input vector $\{\mathbf{u}_v\}$ to the output vector $\{\mathbf{y}_v\}$ via a gain matrix, $[\mathbf{G}_v]$, as

$$\{\mathbf{u}_v\} = [\mathbf{G}_v]\{\mathbf{y}_v\} \tag{3.53}$$

Substitution of equation (3.53) into equation (3.51) yields the closed-loop ASE equations of motion

$$\{\dot{\mathbf{x}}_v\} = [\bar{\mathbf{A}}_v]\{\mathbf{x}_v\} \tag{3.54}$$

where

$$[\bar{\mathbf{A}}_v] = [\mathbf{A}_v] + [\mathbf{B}_v][\mathbf{G}_v][\mathbf{I} - \mathbf{D}_v\mathbf{G}_v]^{-1}[\mathbf{C}_v] \tag{3.55}$$

3.6.5 Flutter Analysis. The ASE flutter analysis is based on the eigenvalues of $[\mathbf{A}_{ae}]$ in the open-loop case and those of $[\bar{\mathbf{A}}_v]$ in the closed-loop case. The flutter dynamic pressure in both cases is the lowest dynamic pressure at which the imaginary part of one of the roots becomes positive. Additional details pertaining to specific flutter sensitivity analysis and equations are detailed in the ZAERO Theoretical Manual [36].

IV. Methodology

The overall objective of this research was to determine the natural modes of vibration that are most critical in the buffet response of the F-16 ventral fin, and design piezo-electric actuators capable of reducing that buffet in support of future flight testing and subsequent technology development. Several important steps were accomplished to meet that objective. An FEM of the ventral fin was obtained and optimized in order to accurately represent the Block 15 fin which will be used for actual flight testing. Using historical data and the results of a ZAERO aeroelastic analysis of the FEM, the three most critical vibration modes were determined. The first four modes were further analyzed for MFC actuator placement and alignment. That analysis consisted of identifying areas of high strain energy density, as well as the directions of princi-pal strain. The actuators themselves were designed and implemented via a thermal analogy within MSC.Nastran. Subsequently, all possible two-mode combinations of actuators for the three most critical modes were modeled and tested using a simple control scheme within the ZAERO ASE module. That analysis was conducted in order to determine modal interaction and stability characteristics, useful for selection of the two most critical modes. Finally, flight test data obtained from ALC testing conducted at the USAF TPS was analyzed to further enhance selection of the two most critical modes.

4.1 FEM Development

The first step in the process of designing actuators for the ventral fin was to obtain an accurate FEM model of the fin. The actual ventral fin which will be used in future flight testing is a Block 15 fin, selected for its decreased rigidity relative to the improved Block 40 version. A search was conducted for an existing NASTRAN FEM of the Block 15 fin, but none was found. Instead, a Block 40 FEM of the entire bottom rear structure of the aircraft as shown in Figure 4.1 was discovered and provided by Mr. Bob Bair of the Aeronautical Systems Center. The history of the model indicated that it had originally been modified to reflect the Block 15
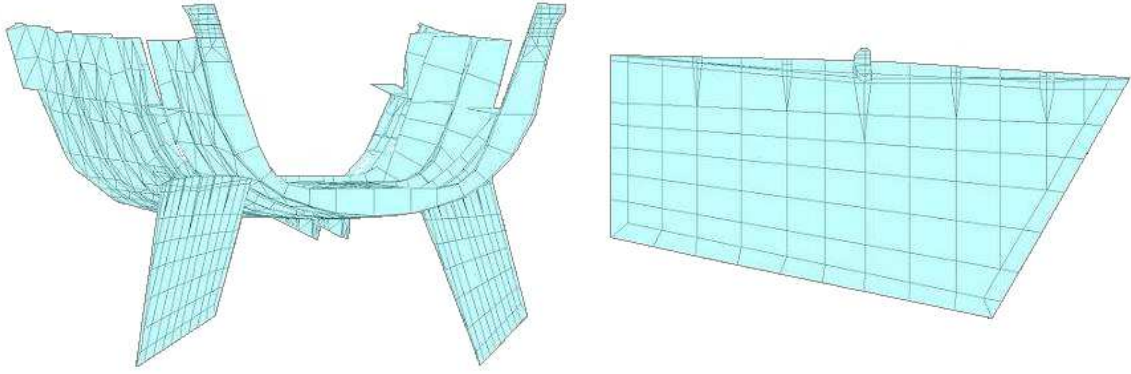
Figure 4.1:   Bottom Rear Aircraft Structure and Ventral Fin FEMs

configuration then modified again to incorporate structural changes to the engine access cover and ventral fins consistent with Block 40 upgrades [13]. Since no other models were available, a decision was made to manually detach a ventral fin and use it for the research and analysis to follow. The detached fin FEM is also shown in Figure 4.1.

4.1.1 Ventral Fin FEM.   The report and data which accompanied the FEM, including discussion of a documented ventral fin failure on F-16 tail number 89-2087, differences between the Block 40 and pre-Block 40 fins, and illustrations of the coarse grid model of the fin, primarily referenced the left side fin as opposed to the right [24] [34]. Consequently, the left side fin was selected for removal from the remainder of the FEM. In retrospect, it would have been more appropriate to remove the right side fin since the actual fin, which will be used in future flight testing to further develop the concepts presented in this thesis, is a right side fin. Nonetheless, the left side fin was removed from the FEM and altered slightly to better reflect the Block 15 configuration. According to Paul Ret, improvements made to the Block 40 fin included: "larger diameter bolts at forward secondary attachments, a thicker airfoil section with added rib material at the forward bolt, and 'wings' providing a larger moment arm between the bolt and compression bearing area" [24, page 3-1]. As depicted in Figure 4.2, the "wings" were removed from the FEM of the fin. The forward attachment bolt hole diameter, airfoil thickness, and rib configuration were left un-
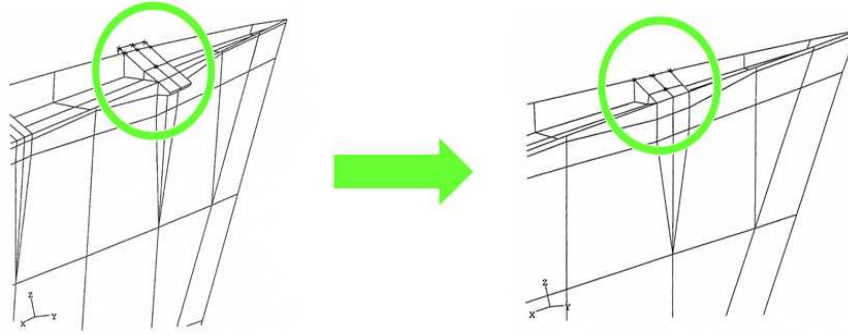
Figure 4.2:   Ventral Fin FEM Modification

changed, as the size of the bolt hole was deemed insignificant and specific information
on the changes made to the airfoil thickness and rib material was unavailable.

4.1.2   FEM Model Manual Tuning.   After removing the left side ventral
fin from the original FEM and modifying it to more accurately reflect the pre-Block
40 structural configuration, the model was tuned using published data from a Block
15 ground vibration test (GVT) and Block 30 NASTRAN model [24, page 4-3]. In
order to determine an appropriate course of action for tuning the model, a baseline
modal analysis was conducted using NASTRAN with the mounting surface of the
fin completely constrained. After determining that the baseline frequencies for the
first two modes were too high in comparison with published data, tuning springs
were added to the FEM along the mounting surface and bracket. The springs were
intended to model the flexibility of the fuselage along the mounting surface since those
effects had been eliminated when the fin was detached from the original FEM. They
also decreased the stiffness of the fin-to-fuselage connections and consequently each
of the modal frequencies. Initially, the springs were all combined into one set, though
that configuration was effective for tuning only one mode. Three sets of springs were
used for the next iteration as shown in Figure 4.3. One set was composed of a spring
attached to each of the nodes (with the exception of the end node) on the front of the
mounting surface relative to the bracket; one set was composed of springs attached
to two of the nodes comprising the surface of the mounting bracket where the bolts
would be located; and the final set was composed of a spring attached to each of the
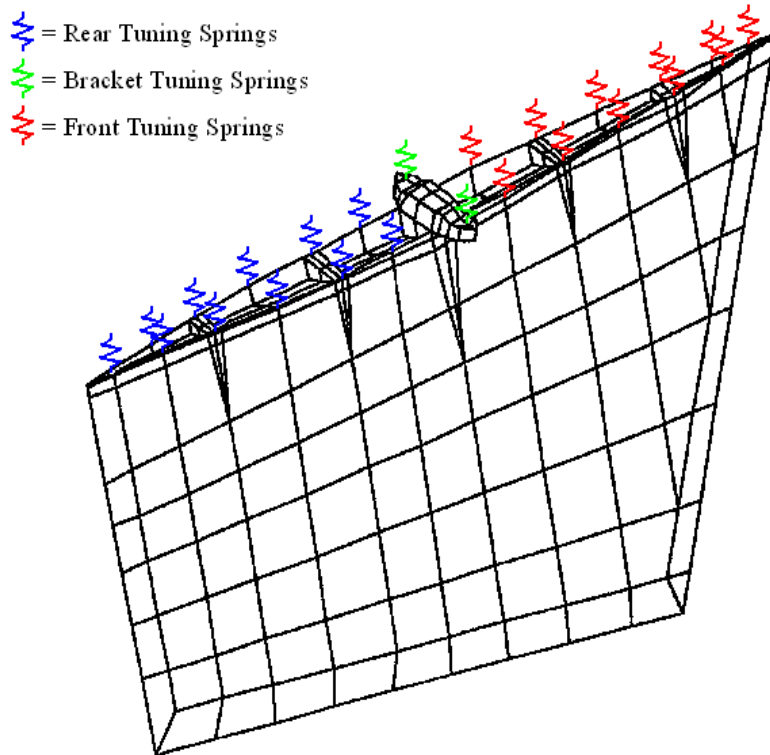
Figure 4.3:   Ventral Fin Manual Tuning Spring Locations

nodes (with the exception of the end node) on the rear portion of the mounting surface relative to the bracket. The objective in using the springs was to tune the first three modes. By manually adjusting the spring constants for each section, good results were obtained for the first two modes. However, it was not possible to improve Mode 3 concurrence with predictions since the starting value was too low and the springs were not capable of increasing the frequency of vibration.

4.1.3 FEM Model Optimization.   To assure reasonable matching of the modal frequencies with existing data, an optimization routine had to be run within NASTRAN. In reality, the optimization of the FEM model was conducted after analyzing PSD plots from existing flight test data, reviewing the history of ventral fin failures, and analyzing the initial flutter results from ZAERO (all of which are presented in the section titled "Critical Mode Selection").

The optimization was carried out by defining design variables, design constraints and a cost function, all of which were input into NASTRAN using the SOL 200 routine. The routine proceeded to optimize the eigenvalues (natural frequencies) for the vibration modes of the fin based upon the aforementioned optimization definitions. The design variables included the four different skin thicknesses located as shown in Figure 4.4 as well as the spring constants for each of the three sets of tuning springs which were introduced during the manual tuning of Modes 1 and 2. The actual regions of varying skin thickness were not altered from the original FEM. The design constraints were the frequency windows defined by the previously published Block 15 GVT and Block 30 NASTRAN modal data shown in Table 4.1. The Block 15 GVT data did not include a Mode 5 frequency. Therefore, a value of 225.0 Hertz was assumed in order to maintain the difference between Block 15 and Block 30 data as seen in Modes 3 and 4. A cost function as defined in equation (3.6) was also employed to minimize the changes in design variables. Two attempts were made. The first attempt optimized the first five modes, however, the resulting skin thicknesses were believed to be unreasonable. Subsequently, optimization of the fifth mode was deemed unnecessary based upon a review of power spectral density charts from existing flight test data, documentation of ventral fin failures including the specific geometric characteristics of those failures, and results of a flutter analysis which was undertaken using Zona's ZAERO program. Consequently, a second optimization was performed in an effort to optimize only the first four modes. After running the second optimization, a visual analysis of the resulting mode shapes was performed to ensure consistency with published GVT data.

Table 4.1:   Optimization Design Constraints

	Mode 1	Mode 2	Mode 3	Mode 4	Mode 5
Block 15 GVT	69.1 Hz	87.1 Hz	155.3 Hz	210.5 Hz	N/A
Block 30 NASTRAN	68.7 Hz	88.5 Hz	140.7 Hz	197.9 Hz	212.4
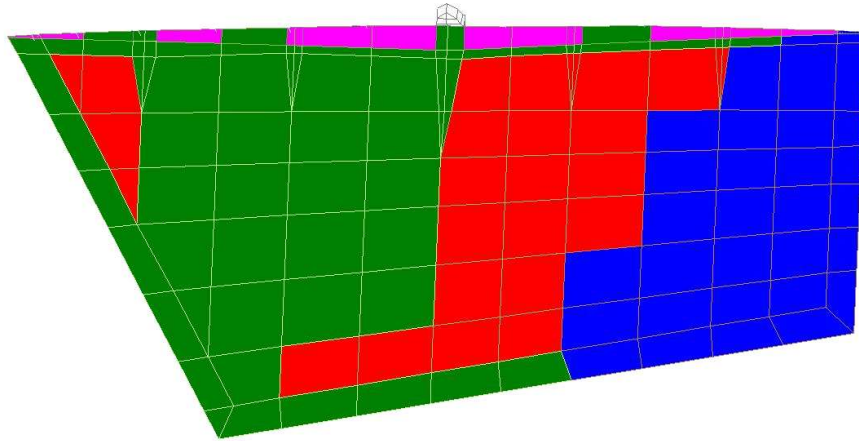
Figure 4.4:   Optimized Skin Thickness Locations

4.2   Critical Mode Selection

Selection of the most critical vibration modes of the ventral fin was an extremely important facet of the research and analysis, as consideration had to be given to TPS flight testing which will take place in the future. Coordination with the experts in charge of aircraft modification at TPS revealed that wiring within the aircraft will only allow for two sets of piezoelectric actuator patches. Therefore, selection of the two most dominant and potentially damaging modes became a top priority. Several factors were considered in selecting the critical modes.

4.2.1   Analysis of Power Spectral Density Plots.   First, PSD charts from existing flight test data (completed prior to the initial TPS ALC testing) were analyzed for trends indicating the most dominant modes of vibration. Three separate sets of data were analyzed. The first was from the F-16 LANTIRN Pod Turbulence Investigation, completed in May 1985 [8]. The second was from the Durability Patch Considerations Report, completed in January 1994 [25], and the final set was from a Royal Netherlands Air Force ventral fin test conducted between 1994 and 1995 [7].

4.2.2   History of Ventral Fin Failures.   The second factor considered in selecting the critical modes was the documentation detailing previous ventral fin failures. Specifically, the geometric characteristics of documented failures were compared

4-6

to FEM strain energy plots in an attempt to correlate predominant failure characteristics with the strain energy of specific modes.

4.2.3 Zona ZAERO Analysis.   The final factor considered in selecting the critical vibration modes was the result of a flutter analysis undertaken using Zona's ZAERO software [37]. As previously stated, ventral fin vibration is a buffet problem. Although an accurate representation of the buffet field created by the LANTIRN pod was not available, it was important to include aerodynamic effects in the analysis and selection of critical modes in some manner. Therefore, ZAERO was used to predict flutter conditions for the fin as well as the associated modal participation. Despite the fact that buffet and flutter are different aeroelastic phenomenon, the analysis was useful for understanding the general aeroelastic behavior of the fin and modal interaction prior to flutter onset.

Implementation of the ZAERO module began with the generation of a simple two-dimensional aerodynamic model. As shown in Figure 4.5, the aerodynamic model grid consisted of ten chordwise and four spanwise divisions for a total of 40 grid segments. Within ZAERO, the side of the grid representing the outboard edge of the ventral fin was oriented parallel to the streamwise flow, and a spline function was used to allow the aerodynamic and structural models to communicate throughout the flutter analysis. In order to perform the analysis, ZAERO required input of non-dimensional reduced frequencies defined as

$$k = \frac{\omega b}{V} \tag{4.1}$$

where k is the reduced frequency, ω is the harmonic oscillation frequency, b is the semi-chord characteristic length and V is the freestream velocity. A range of reduced frequencies was calculated to cover the first five modes and possible velocities (0.25 to 0.95 Mach) at which an actual ventral fin will likely be flight tested. Implementation of the software also included specification of two different "match-point" search
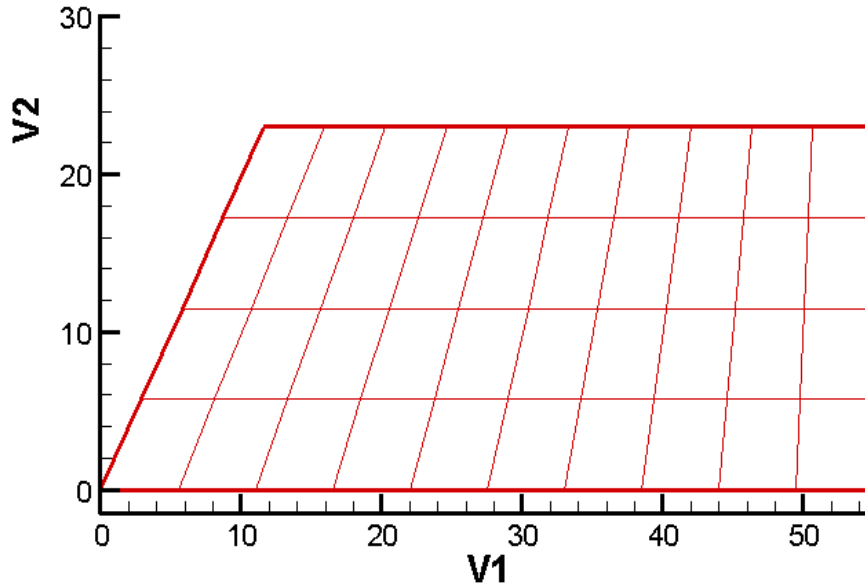
Figure 4.5:   ZAERO Aerodynamic Model Grid

methods used to locate flutter conditions. The first method specified a fixed density (or altitude) with varying Mach number and the second specified a fixed Mach number with varying density (altitude). While conducting the analysis, the primary emphasis was on two airspeeds, 0.85 and 0.95 Mach. At the time the research was conducted, 0.85 Mach was the highest Mach number at which the test aircraft used by TPS was cleared to fly. However, previous flight tests at which ventral fin buffet had been observed, as documented in Section 4.2.1, were accomplished at 0.95 Mach. Preliminary analysis using ZAERO was performed using the manually tuned (non-optimized) FEM, as optimization of the FEM modal parameters had not yet been performed. Initial results, as further detailed in Chapter IV, revealed a Mode 3 instability. However, the Mode 3 frequency for the ventral fin FEM was inaccurate as it had not been tuned to a historically reasonable value. Consequently the FEM was optimized as discussed in Section 4.1.3., and an additional ZAERO analysis was conducted for 0.85 and 0.95 Mach using the optimized FEM.

4.3 Piezoelectric Actuator "Patch" Design

After completing the attempts at critical mode selection detailed above, Modes 1, 2 and 4 appeared equally critical. Consequently a decision was made to proceed with the design and implementation of piezoelectric actuator patches within the ventral fin FEM using a thermal analogy. The assumption was that after designing patches for the aforementioned modes and integrating them into the FEM, it would be possible to use the ASE Module within ZAERO to analyze the patch layout for each mode individually and determine the relative effectiveness of each one in terms of modal stability. Though Mode 3 was not believed to be one of the most critical modes of vibration per the previous analyses, it was included in the initial patch placement and design process for the sake of completeness.

4.3.1 Considerations for Patch Placement. Several factors were taken into account when designing the patch layout for each of the first four modes. First, consideration was given to the location of pressure tap holes and accelerometers on the existing Block 15 ventral fin currently instrumented for flight testing, as shown in Figure 4.6). Patch placements were chosen to avoid interference with those locations in order to maintain consistency in the instrumentation layout between past and future testing. Note that Figure 4.6 depicts a right side ventral fin, as it is was produced from mechanical drawings of the actual fin which will be used for flight testing. As previously mentioned, the ventral fin FEM used throughout this research was representative of a left side fin. Consequently, a mirror image of the instrumentation locations shown were assumed for the FEM.

4.3.2 Placement via Strain Analyses. After noting the aforementioned instrumentation locations, FEM strain energy plots for the first four vibration modes were produced and analyzed from the optimized FEM to determine the predicted locations of concentrated strain energy for each mode. By determining areas of concentrated strain energy, it was possible to choose the general patch placement locations for each mode based upon existing FEM nodes. The patches were located in such a
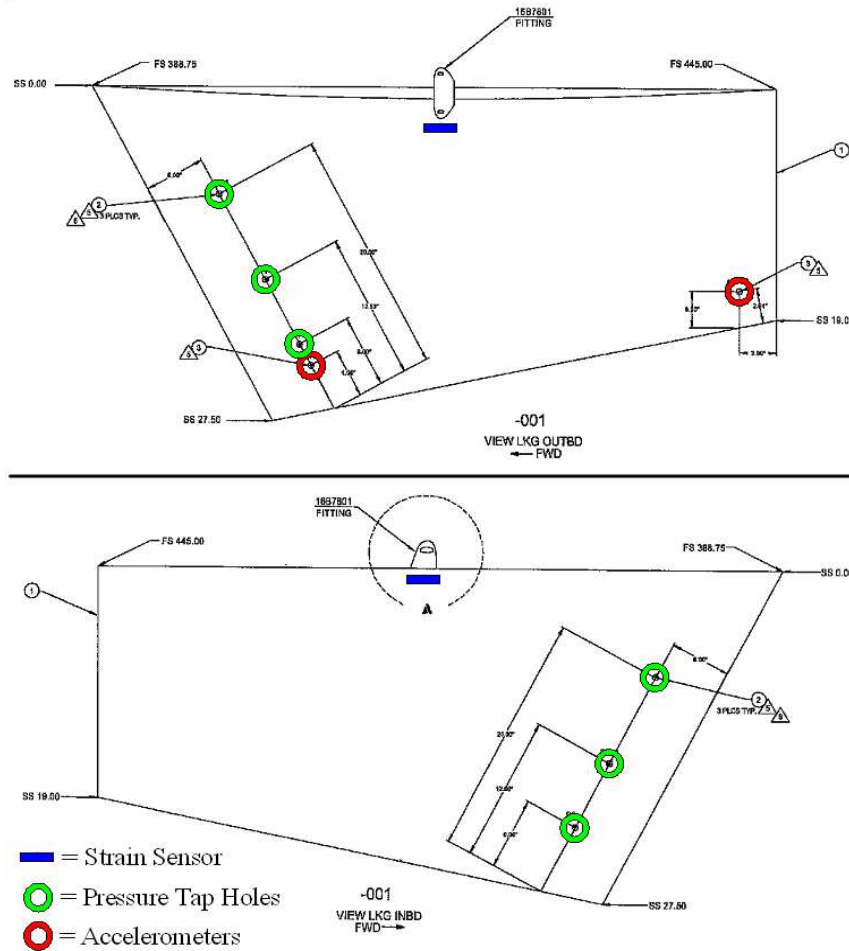
Figure 4.6:   Locations of Pressure Tap Holes and Accelerometers

manner as to cover the regions of highest strain density while avoiding the existing instrumentation locations detailed in Section 4.3.1.

After determining the general patch placement locations, plots of the major and minor principal strain vectors for each mode were produced and used to determine the proper fiber direction for each of the actuators, as well as the number of patch layers required on each side of the fin for each mode. Several steps were taken to complete this process. First, a new patch coordinate system was defined within the FEM relative to the ventral fin as shown in Figure 4.7. This coordinate system was used in conjunction with the plots detailing the principal strain vectors for each of the first four modes in the regions of proposed patch application, allowing manual

4-10

measurement of the θ angle for each major strain vector. The angles of the major strain vectors were averaged for the elements composing each proposed patch application area, providing a single specific fiber direction relative to the aforementioned coordinate system for each patch. Plots from both the manually spring-tuned version and the optimized version of the FEM were analyzed and compared in this way for differences. Although the optimized model was preferred for use throughout the remainder of the research, because of favorable modal properties, the thickness of the skin elements had been changed from the original FEM of the fin during the optimization process. Consequently, there was a concern that those changes could have had a significant impact on the characteristics of the principal strains throughout the FEM. In actuality, the differences in the strain characteristics were minimal, so a decision was made to use the angles found through analysis of the optimized model, rounding off to the nearest five degrees in the direction of each corresponding non-optimized model angle value. For mode 2, the optimized angle value was so close to an even 15 degrees that it was not rounded toward the unoptimized value. In order to determine the number of patch layers required, major and minor principal strain vector magnitudes were visually compared for each mode. If the differences in magnitude were significant, one patch was used per side with the fiber direction oriented as determined by the major strain vector θ angle. If the magnitudes were similar, two patches were used per side with the fiber direction of one layer oriented as determined by the major strain vector and the fiber direction of the second layer oriented perpendicular to the first.

4.3.3 Implementation within FEM. The mathematical basis for the piezoelectric patch design and implementation was presented in Section III. A thermal analogy for the actuators was developed because NASTRAN does not allow for piezoelectric attributes within element property fields. It does, however, allow for thermal properties. Therefore, it made sense to develop a thermal analogy in which $\Delta V \sim \Delta T$. The thermal coefficients for the analogy were calculated using actual piezoelectric ac-

4-11

tuator properties listed in the MFC engineering properties data sheet provided by the Smart Material corporation [29]. An assumption was made that orthotropic actuators will be used for the actual fin in order to take advantage of the benefits outlined in Section II. Consequently, the thermal analogy was implemented in such a way to ensure that positive strains in the fiber direction of a patch would be accompanied by negative strains in the plane perpendicular to the fiber direction and vice versa.

When integrating the patches into the FEM, the patch thickness (0.012 inches) and the average skin thickness within each specific area of proposed patch application were used to determine an appropriate offset from the center of each skin element to the center of each patch element. This was done to ensure the patch elements laid upon the surface of the normal skin elements as they will on the actual fin. When two layers of patches were used, the same methodology was employed to ensure the top layer laid upon the surface of the bottom layer.

After the FEMs of the patches for each particular mode were constructed, they were individually tested by applying a 150 Volt signal via the thermal analogy. A 150 Volt signal was used because TPS personnel estimated that the voltage to be used on the actuators will be in the 150-to-200 Volt range. For modes with one layer per each side of the fin, opposite voltage polarities were used from one side to the other. For modes with two layers per side, the layers on a given side had opposite polarity as did a given layer from one side to the other. The resulting fin deformations for each mode
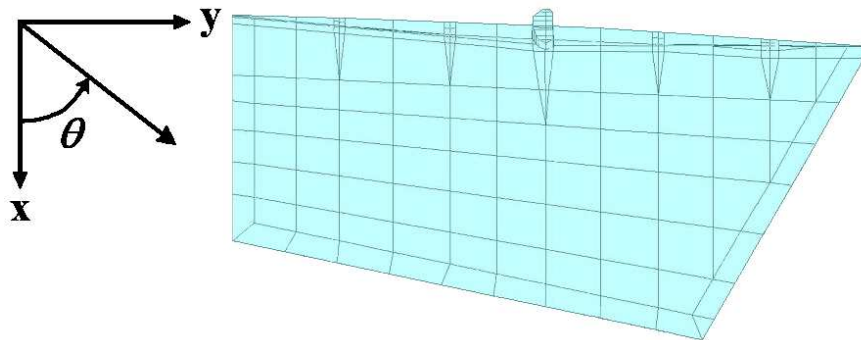
Figure 4.7:   Piezoelectric Patch Fiber Coordinate System

4-12

were observed to ensure consistency with the deflections required to counter modal vibrations.

Finally, each possible two-mode combination of patches was applied to the ventral fin FEM individually, and a modal analysis was conducted without piezoelectric actuation to assess the degree to which the patches increased the stiffness of the fin and, therefore, the modal frequencies. The mass density of the actuators and bonding material (4.75 grams per cubic centimeter) was also included in the analysis.

4.4 Critical Mode Selection Revisited

4.4.1 ZAERO ASE Analysis. After the piezoelectric actuator patch layouts were designed for the first four modes, a final ZAERO analysis was conducted in the interest of comparing the effectiveness of the patches for Modes 1, 2, and 4 using the ASE module. The ASE module was selected for the final critical mode selection process because it allowed analysis of a closed-loop control system which will be required when the piezoelectric actuators are flight tested. The ASE module was integrated with the flutter analysis and predictions were obtained after the required control parameters and components were defined. Patch-induced deformation was defined as the control surface and the mid-plane FEM nodes nearest the accelerometer locations depicted in Figure 4.6 were selected as the locations for acceleration feedback. Specifically, the aft accelerometer location was used for Mode 1, and the forward accelerometer location was used for Modes 2 and 4. Figure 4.8 depicts the control schematic. Note that the ASE module effectively completed the feedback loop by activating the piezoelectric actuators and determining the resulting acceleration. The default actuator transfer function,

$$\frac{A_0}{s^3 + A_2 s^2 + A_1 s + A_0} \tag{4.2}$$

was employed throughout the analysis, where $A_0 = 27\omega_{max}^3$, $A_1 = 13.5\omega_{max}^2$, $A_2 = 4.5\omega_{max}$ and w_{max} was the frequency of the highest normal mode used in the analysis.
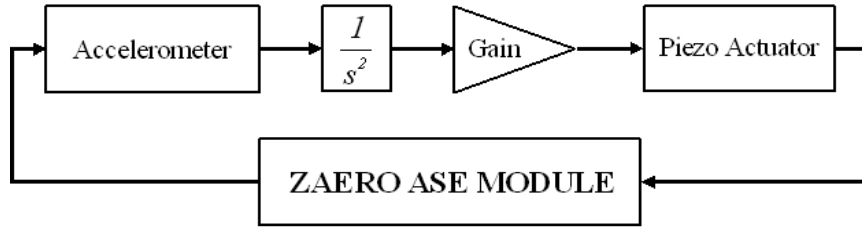
Figure 4.8:   ZAERO ASE Module Control Schematic

An ASE analysis was conducted for each piezoelectric actuator patch individually attached to the ventral fin using simulated flight conditions of 0.95 Mach and altitudes ranging from -100,000 feet to 6,000 feet mean sea level (MSL). The results at 5,000 feet MSL were analyzed to compare changes in aeroelastic stability for each set of patches at a realistic flight altitude using a range of control system gains from -25 to 25.

4.4.2   ALC Flight Testing.   Finally, 96 PSD plots from the ALC testing which was conducted by TPS students in October 2005 were referenced in an effort to determine which ventral fin vibration modes were most dominant in flight, while confirming that the modal frequencies seen were reasonably close to those predicted by the FEM [14]. The plots had been generated from data produced by a strain sensor and the forward accelerometer depicted in Figure 4.6. The strain sensor was comprised of four general purpose constantan strain gages arranged in a full Wheatstone Bridge configuration; two gages were installed on the inboard side of the central mounting bracket and two adjacent gages were installed on the outboard side of the bracket [2]. The data used to produce the plots were collected throughout a flight envelope ranging from 0.3 to 0.9 Mach at altitudes from 5,000 to 35,000 feet MSL. For each plot, the two most dominant modes, in terms of magnitude without the active flow control actuators operating, were noted and recorded. The modal frequencies for the first five modes were determined by analyzing two plots with well defined peaks which were produced from data gathered at 0.6 Mach and 20,000 feet MSL altitude.

V. Results and Analysis

This chapter presents a complete summary of the results of the research conducted in support of this thesis. The objective was to determine the natural modes of vibration that were most critical in the buffet response of the F-16 ventral fin, and design piezo-electric actuators capable of reducing that buffet in support of future flight testing and subsequent technology development. The research was essentially divided into four segments. The FEM of the ventral fin was successfully modified, tuned and optimized to ensure its modal characteristics were consistent with published data from a Block 15 GVT test and a Block 30 FEM. An initial attempt at critical mode selection through the analysis of historical data and a set of ZAERO analyses showed Modes 1, 2 and 4 to be the most critical, though it was not possible to choose the two most dominant modes. Next, the design and implementation of piezoelectric actuator patch layouts for the first four modes within the FEM was successfully accomplished. Finally, the second phase of critical mode selection was completed, providing additional justification for selecting Modes 1, 2 and 4 as the most critical. Data collected from the TPS ALC project during this phase indicated that Modes 1 and 4 were the most observable for the actual ventral fin, given the existing instrumentation locations. However, they were not necessarily the most critical modes.

5.1   FEM Validation

Validation of the ventral fin FEM was achieved by performing a series of modal analyses using MSC.Nastran to ensure the vibrational properties of the fin were consistent with published data. The results of the first modal analysis, which was performed on the fin with the mounting surface completely constrained, provided a starting point from which to tune the model using the springs described in Section 4.1.2. Although the tuning springs were useful for tuning the first two modes of vibration, they were found to be insufficient for tuning the others. Optimization of the FEM was necessary in order to obtain accurate modal properties for the first four modes, and the results

of the optimization routine provided the required validation of the accuracy of the ventral fin FEM.

5.1.1   FEM Model Manual Tuning.   The first modal analysis on the ventral fin FEM was completed with the mounting surface completely constrained. The results of the analysis were compared to published data from a Block 15 GVT and Block 30 NASTRAN model [24, page 4-3]. Table 5.1 summarizes the results of that analysis. Whereas Modes 1, 2, and 5 appeared to be too high in relation to the published data, Modes 3 and 4 appeared to be too low.

The first attempt at manually tuning the fin FEM was conducted using one set of tuning springs with a single spring constant. Using this configuration with a spring constant of 7.85×10^6 pounds-force per inch, Mode 1 was tuned to match the Block 30 NASTRAN historical data as shown in Table 5.1.

The second attempt at manually tuning the fin FEM was conducted using three sets of tuning springs as shown in Figure 4.3 with a separate spring constant for each set. Using this configuration with a front set spring constant of 7.2×10^{13} pounds-force per inch, a bracket set spring constant of zero pounds-force per inch, and a rear set spring constant of 3.9×10^6 pounds-force per inch, Modes 1 and 2 were tuned to closely approximate the Block 30 NASTRAN historical data as shown in Table 5.1.

Although manual tuning was fairly effective for the first two modes and possibly the fifth by chance, it was clearly inadequate for Modes 3 and 4. In order to accurately tune the first four modes, an optimization strategy had to be employed.

Table 5.1:   Modal Characteristics - Baseline and Spring-Tuned Ventral Fin FEM

	Mode 1	Mode 2	Mode 3	Mode 4	Mode 5
Block 15 GVT	69.1 Hz	87.1 Hz	155.3 Hz	210.5 Hz	N/A
Block 30 NASTRAN	68.7 Hz	88.5 Hz	140.7 Hz	197.9 Hz	212.4 Hz
Fin FEM - Baseline	74.3 Hz	94.9 Hz	126.9 Hz	187.4 Hz	236.3 Hz
Fin FEM - 1 Spring Set	68.7 Hz	84.5 Hz	122.4 Hz	182.0 Hz	219.0 Hz
Fin FEM - 3 Spring Sets	68.7 Hz	88.9 Hz	122.6 Hz	182.5 Hz	217.9 Hz

5.1.2 FEM Model Optimization. The first attempt at optimization of the
ventral fin FEM was performed using the frequency windows for all five modes shown
in Table 4.1 as design constraints. As mentioned in Section 4.1.3, a frequency of 225
Hertz was assumed for the missing Mode 5 value. Results of the initial optimization
attempt are presented in Table 5.2. Table 5.3 summarizes the design variable changes
implemented by NASTRAN in order to achieve the modal values listed in Table 5.2.
Note that the initial value for the bracket springs constant was arbitrarily set to 5.0
x 10^6 since the optimization routine would not run with it set to zero. In reference
to the skin thickness regions shown in Figure 4.4 and listed in Table 5.3, Region 1 is
red, Region 2 is green, Region 3 is blue, and Region 4 is magenta.

While the majority of the design variable changes for the first optimization
attempt appeared to be reasonable, the change in the skin thickness for Region 1 was
not. A 348.35% increase was simply believed to be too large to safely assume that
it would not have a detrimental impact on the realism of the fin model and, hence,
the remainder of the research. Consequently, a second optimization attempt was
performed without incorporating the Mode 5 frequency window as a design constraint

Table 5.2:   Modal Characteristics - First Optimization Attempt

	Mode 1	Mode 2	Mode 3	Mode 4	Mode 5
Block 15 GVT	69.1 Hz	87.1 Hz	155.3 Hz	210.5 Hz	N/A
Block 30 NASTRAN	68.7 Hz	88.5 Hz	140.7 Hz	197.9 Hz	212.4 Hz
Ventral Fin FEM	68.8 Hz	88.6 Hz	140.8 Hz	206.9 Hz	225.1 Hz

Table 5.3:   First Optimization Design Variable Changes

	Initial Value	Optimized Value	% of Initial Value
Rear Springs Constant	3.9000 x 10^6	4.3649 x 10^4	1.12
Bracket Springs Constant	5.0000 x 10^6	5.3370 x 10^6	106.74
Front Springs Constant	7.2000 x 10^{13}	7.1993 x 10^{13}	98.62
Skin Thickness - Region 1	0.016	0.055736	348.35
Skin Thickness - Region 2	0.040	0.029281	73.20
Skin Thickness - Region 3	0.050	0.069290	138.58
Skin Thickness - Region 4	0.080	0.079832	99.79

for the reasons detailed in Section 4.1.3. Results of the second optimization attempt are presented in Table 5.4. Table 5.5 also summarizes the design variable changes implemented by NASTRAN in order to achieve the modal values listed in Table 5.4.

For the second optimization attempt, the changes in skin thickness for Regions 1 and 3 were both higher than desired. They were, however, determined to be acceptable under the condition that future efforts to characterize the strain energy and principal strain vectors within the fin FEM would take into account a comparison of the characteristics of both the optimized and non-optimized versions of the model in order to ensure that the differences resulting from the changes in skin thickness were acceptable. Overall, the optimization process was successful considering the modal values which were obtained.

After completing the optimization routines, a visual analysis of the resulting mode shapes was performed to ensure consistency with published GVT data. A comparison of the mode shapes is shown in Figures 5.1 through 5.4. Despite very slight differences which can be seen in the aforementioned figures, the overall agreement between the published GVT data and optimized model was very good.

Table 5.4: Modal Characteristics - Second Optimization Attempt

	Mode 1	Mode 2	Mode 3	Mode 4	Mode 5
Block 15 GVT	69.1 Hz	87.1 Hz	155.3 Hz	210.5 Hz	N/A
Block 30 NASTRAN	68.7 Hz	88.5 Hz	140.7 Hz	197.9 Hz	212.4 Hz
Ventral Fin FEM	69.1 Hz	88.6 Hz	140.6 Hz	208.2 Hz	248.2 Hz

Table 5.5: Second Optimization Design Variable Changes

	Initial Value	Optimized Value	% of Initial Value
Rear Springs Constant	3.9000×10^6	1.2044×10^5	3.09
Bracket Springs Constant	5.0000×10^6	5.0260×10^6	100.52
Front Springs Constant	7.2000×10^{13}	7.200×10^{13}	100.00
Skin Thickness - Region 1	0.016	0.028443	177.77
Skin Thickness - Region 2	0.040	0.034401	86.00
Skin Thickness - Region 3	0.050	0.103930	207.86
Skin Thickness - Region 4	0.080	0.077375	96.72

GVT MODE 1
f=69.1 Hz
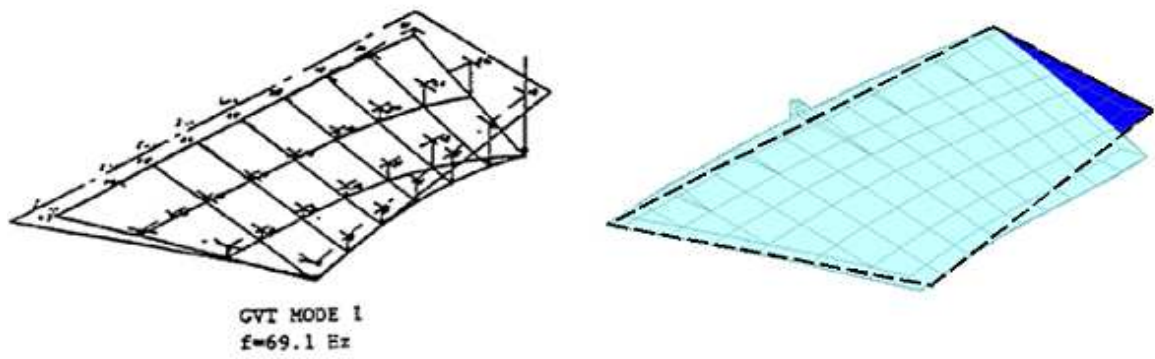
Figure 5.1:   Mode 1 Shape Comparison

GVT MODE 2
f=87.1 Hz
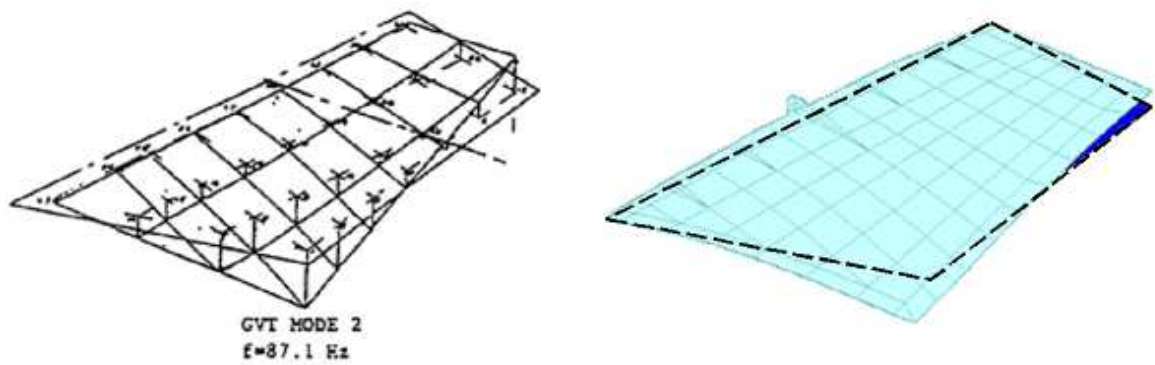
Figure 5.2:   Mode 2 Shape Comparison

GVT MODE 3
f=155.3 Hz
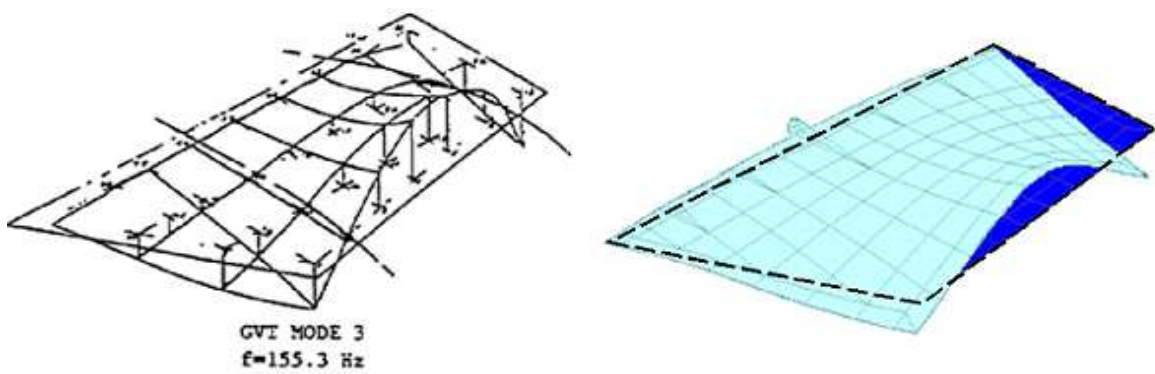
Figure 5.3:   Mode 3 Shape Comparison

GVT MODE 4
f=210.5 Hz
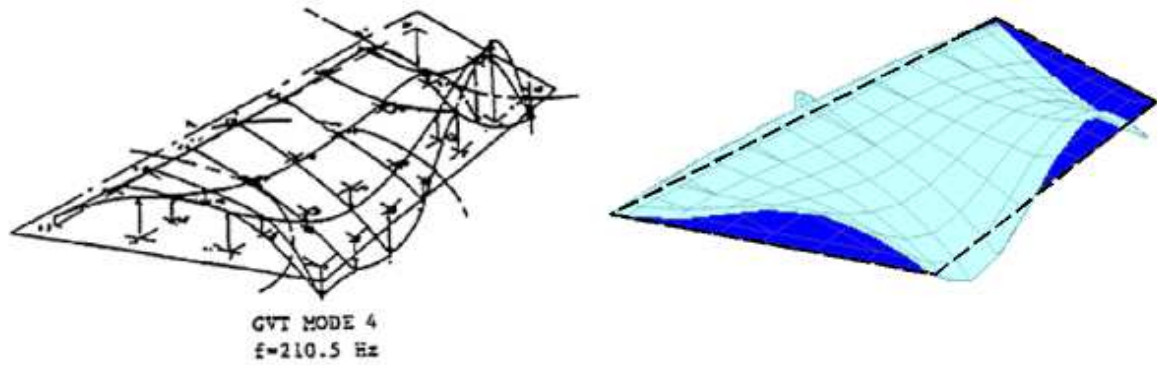
Figure 5.4:   Mode 4 Shape Comparison

5.2   Critical Mode Selection

Although the objective of the initial critical mode selection process was to select the two most critical modes of vibration, the results of the process were only sufficient for determining the three most critical modes.

5.2.1   Analysis of Power Spectral Density Plots.   Representative examples of the PSD plots from each of three sources of historical flight test data are shown in Figures 5.5 through 5.7. Within each figure, the location of the sensor used to produce the data is highlighted using a green circle overlayed on a geometric representation of the ventral fin. Additionally, the dominant modal frequencies for each plot are highlighted with a red circle and identified with text. Although each of the first five modes were visible in various plots viewed during the analysis, Modes 1, 2 and 4 clearly stood out as the most dominant modes.

5.2.2   History of Ventral Fin Failures.   Comparisons of strain energy plots from the ventral fin FEM to the geometric characteristics of historically documented failures were revealing. The documentation showed a definite tendency toward failure in the forward half of the fins as depicted in Figure 5.8. Furthermore, a comparison of the optimized FEM strain energy plots with the documented failures indicated a strong correlation between the typical failure "shape" of actual ventral fins and the Mode 4 strain energy distribution as shown in Figure 5.9.

Figure 5.5:   Left Side Fin Root Bending Moment - 0.95 Mach, 5,000 ft [25]

Figure 5.6:   Left Side Fin Rosette Stress - 0.95 Mach, 5,000 ft, Slow Accel [8]

Figure 5.7:   Right Side Fin Main Attachment Strain - 0.95 Mach, 10,000 ft [7]

Figure 5.8:   Typical Ventral Fin Failure Geometry

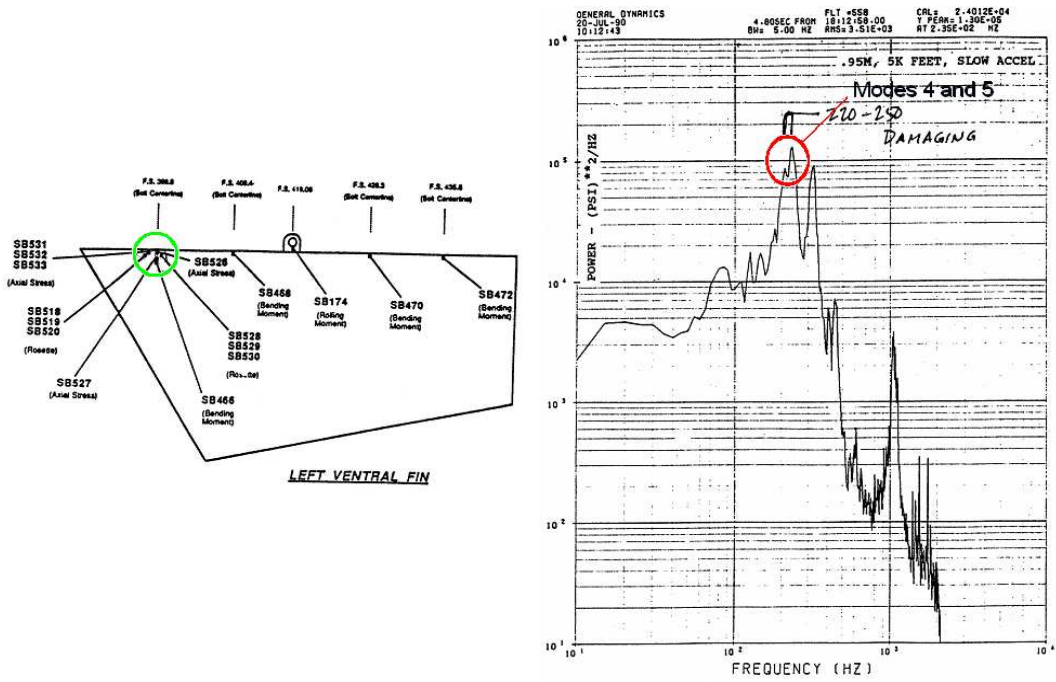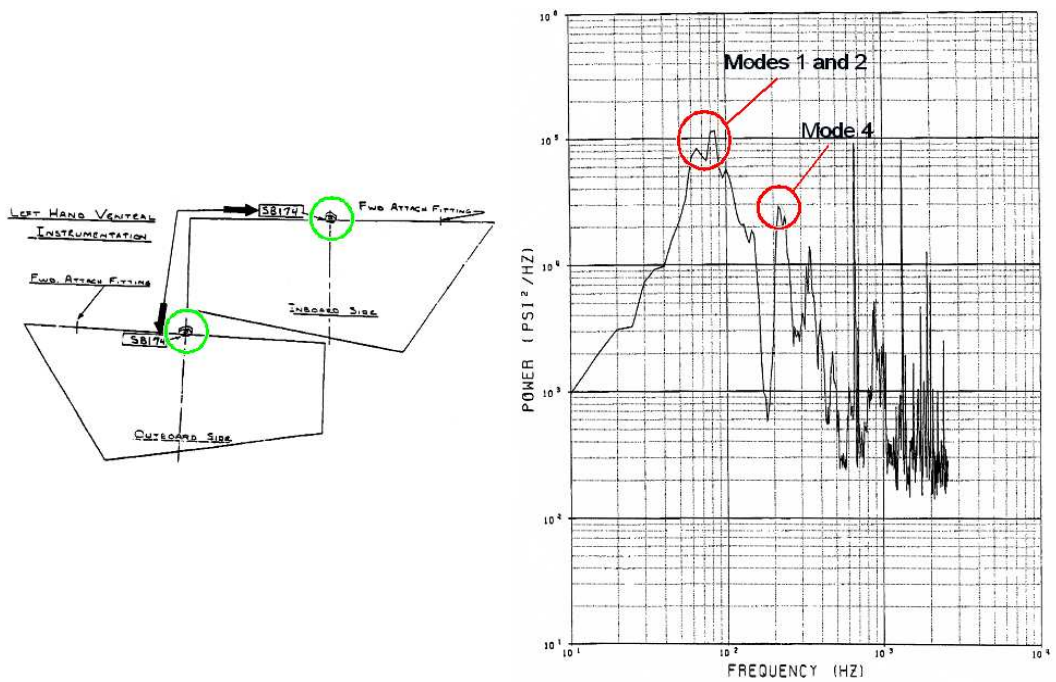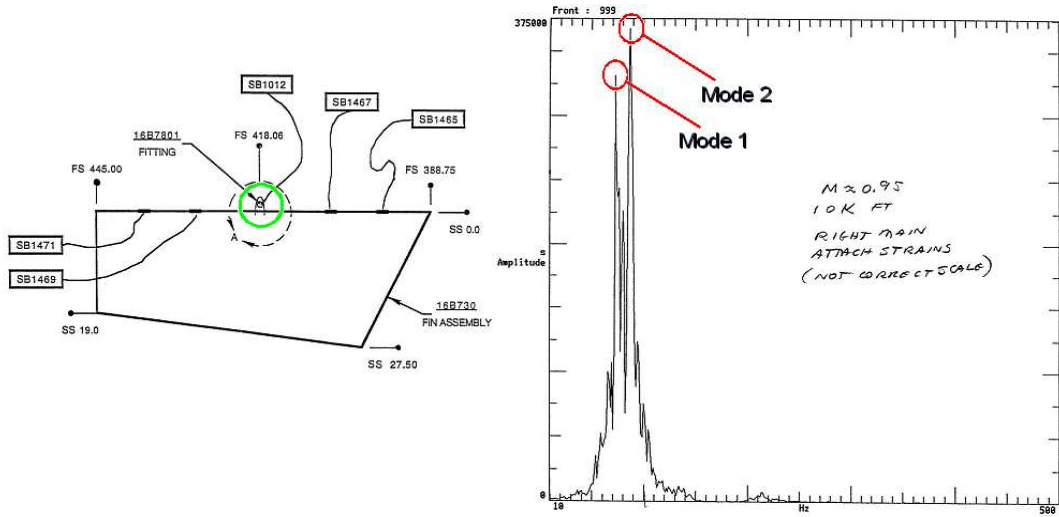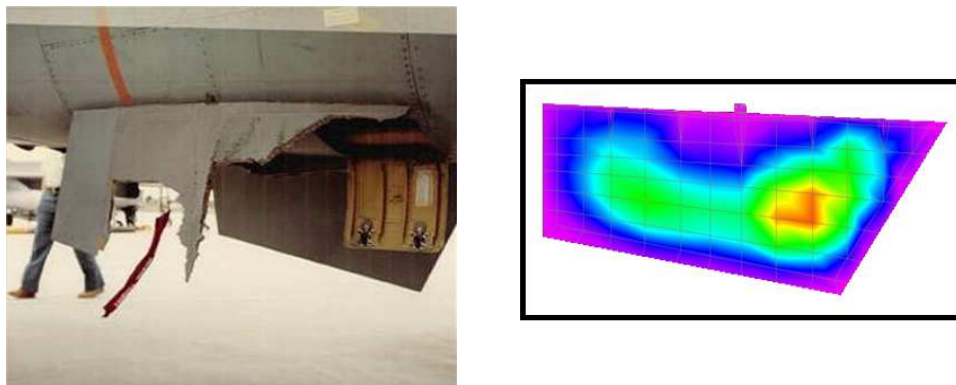

Figure 5.9:   Comparison of Typical Failure to Mode 4 Strain Energy Distribution

5.2.3 Zona ZAERO Analysis. The results of the first ZAERO analysis conducted upon the non-optimized model of the fin, using the method of fixed density with varying Mach number, indicated a complete absence of aeroelastic instability. The second analysis was completed using a fixed Mach number of 0.85 and varying density (or altitude). The results of that analysis are depicted in Figure 5.10. The top half of the figure is a plot of aerodynamic damping on the vertical axis versus velocity on the horizontal axis, and the bottom half of the figure is a plot of frequency on the vertical axis versus velocity on the horizontal axis. Although the horizontal axis for both plots is shown as velocity in units of inches per second, it is also representative of increasing density with decreasing altitude. This is due to the fact that the velocity for a given Mach number is proportional to the square root of the air density. Therefore, the horizontal axis for both plots in Figure 5.10 can be interpreted as altitude ranging from 5,000 feet MSL on the left to -100,000 feet MSL on the right. For the top plot, positive and negative damping are representative of stable and unstable conditions, respectively.

Interpretation of the top plot led to the conclusion that a Mode 3 instability was predicted at a dynamic pressure corresponding to an altitude of approximately -80,000 feet MSL. Modes 1, 3 and 4 were predicted to be the primary contributors to the instability per the modal participation factors, which made sense given further analysis of the plots. The top plot shows Modes 1 and 4 becoming more stable as Mode 3 becomes unstable which would correlate with a transfer of energy between the modes. In addition, the bottom plot shows the frequencies of the three modes coalescing near the point of instability, which is typical of modal interaction prior to such an instability. The instability occurred at a frequency of 110.7 Hertz, approximately halfway between the starting values for Modes 2 and 3. No aeroelastic instabilities were predicted to occur at or above sea level.

As a result of that analysis, a decision was made to optimize the ventral fin FEM as discussed in Section 4.1.3 since the Mode 3 starting frequency used by ZAERO to predict the instability was inaccurate relative to the previously discussed Block 15
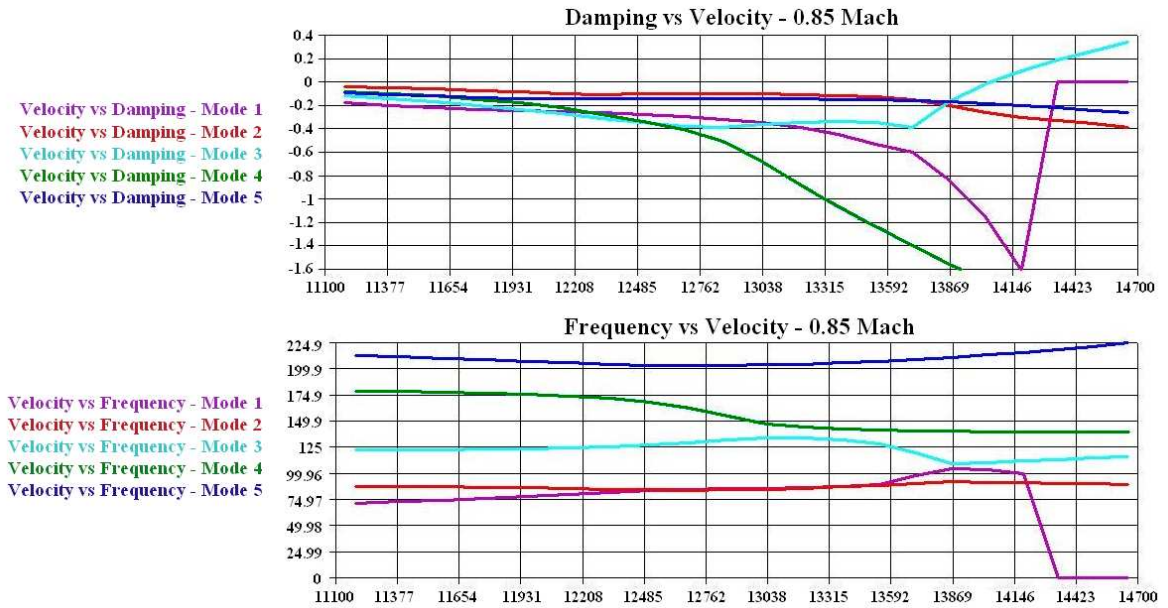
Figure 5.10:   ZAERO Analysis of Non-optimized Fin - Mode 3 Instability

GVT and Block 30 NASTRAN FEM data. After completing the FEM optimization, another ZAERO analysis was performed using the optimized model of the fin at 0.85 Mach with variable density. As depicted in Figure 5.11, the optimization of the FEM resulted in considerable changes to the predicted aeroelastic stability of the fin. Specifically, as shown by the purely negative damping values in the top plot, no instabilities were predicted to occur.

Consequently, a final ZAERO analysis was performed using the optimized model of the fin at 0.95 Mach with variable density in order to simulate the higher dynamic pressures likely needed to induce an instability. As shown in Figure 5.12, the analysis revealed a Mode 2 instability, which was predicted to occur at a dynamic pressure corresponding to an altitude of approximately -90,000 feet MSL. Modes 1 through 4 were all predicted to be contributors to the instability per the modal participation factors and as supported by the manner in which the frequencies for those modes are shown to be coalescing in the bottom plot. The instability occurred at a frequency of 103.0 Hertz, once again between the starting values for Modes 2 and 3. As noted for the analyses conducted on the non-optimized version of the fin, no aeroelastic instability was predicted to occur at or above sea level.
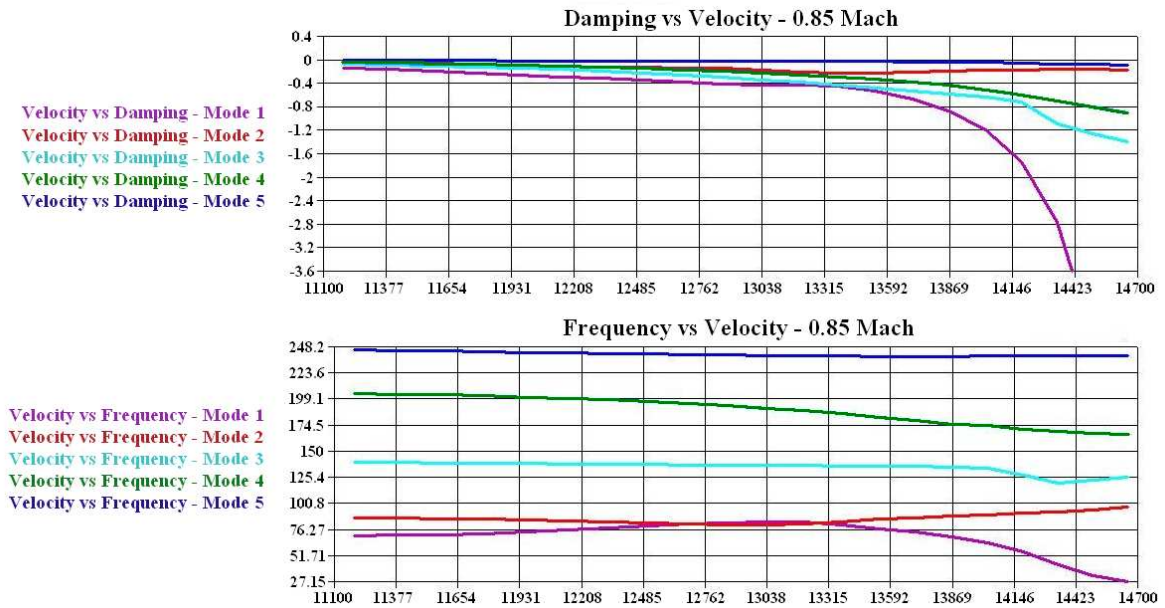
Figure 5.11: ZAERO Analysis of Optimized Fin - No Instabilities

Although the results of the ZAERO analyses supported selection of Mode 2 as one of the most critical modes, they did not provide the degree of justification required to eliminate Mode 1 or 4. In retrospect, it may have proved useful to conduct additional analyses using finer aerodynamic grids until changes in the predicted instability frequency were less than five percent from one run to the next. As a minimum, conducting additional analyses with a refined aerodynamic grid would have provided additional confidence in the accuracy and suitability of the ZAERO results.

5.3 Piezoelectric Actuator "Patch" Design

The process of designing and integrating piezoelectric patches into the ventral fin FEM for each of the first four modes of vibration was very successful, and the resulting patch layouts proved to be useful in completing the second phase of critical mode selection. The results obtained through this process were specific to a left side ventral fin due to the nature of the FEM used. However, the results presented can be confidently applied to further development and implementation of the technology using the actual right side ventral fin available for flight testing.

5-11
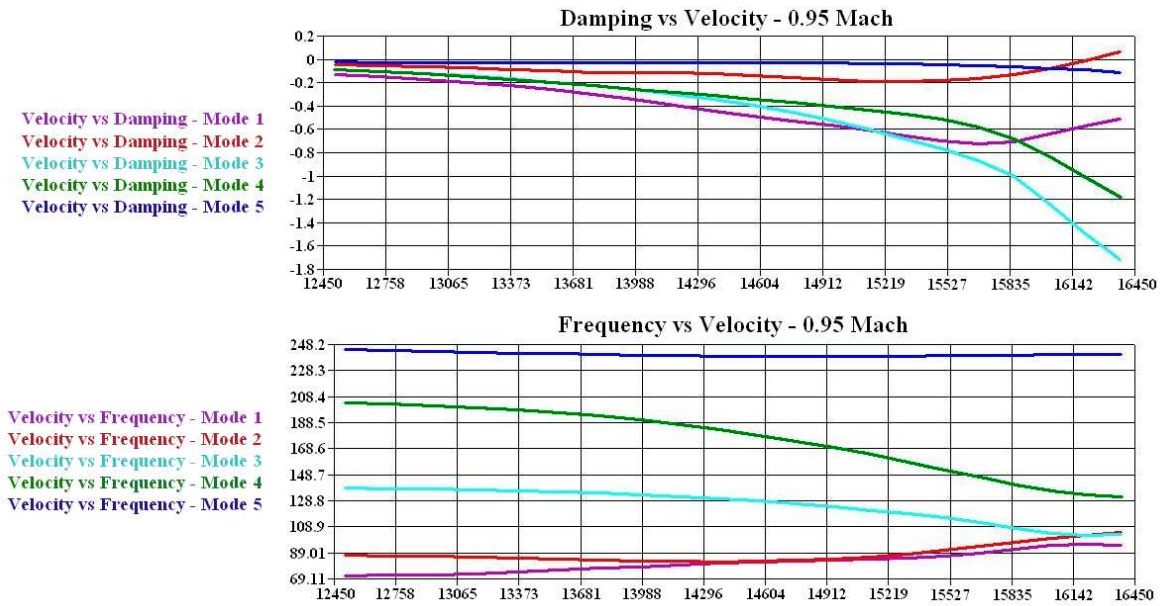
Figure 5.12:   ZAERO Analysis of Optimized Fin - Mode 2 Instability

5.3.1 Placement via Strain Analysis.   Figures 5.13 through 5.16 depict the predicted strain energy and suggested patch placement locations for Modes 1 through 4. These locations were determined through modal analysis of the optimized model using NASTRAN and subsequent visual identification of the regions of highest strain energy. Note that the patch locations were chosen in such a way as to encompass continuous regions containing the highest strain energy for each mode, while keeping the patches to a reasonable size. According to the Smart Material corporation, they are capable of manufacturing an array of MFCs up to a maximum size of approximately 18 inches by 12 inches [6]. In order to implement the patches within the FEM, existing skin elements and nodes needed to be used to define the locations of the patches, hence the irregular shape for the Mode 4 patch outline represented by the black solid line in Figure 5.16. However, in the event that the Mode 4 patches are selected for use on the actual ventral fin, they should be manufactured and applied to match a mounting position similar to the one represented by the dotted red line.

Principal strain plots from both the optimized and non-optimized versions of the FEM were produced and used to compare the major and minor strain vectors for each mode via the method detailed in Section 4.3.2. An example of the type of plots

5-12
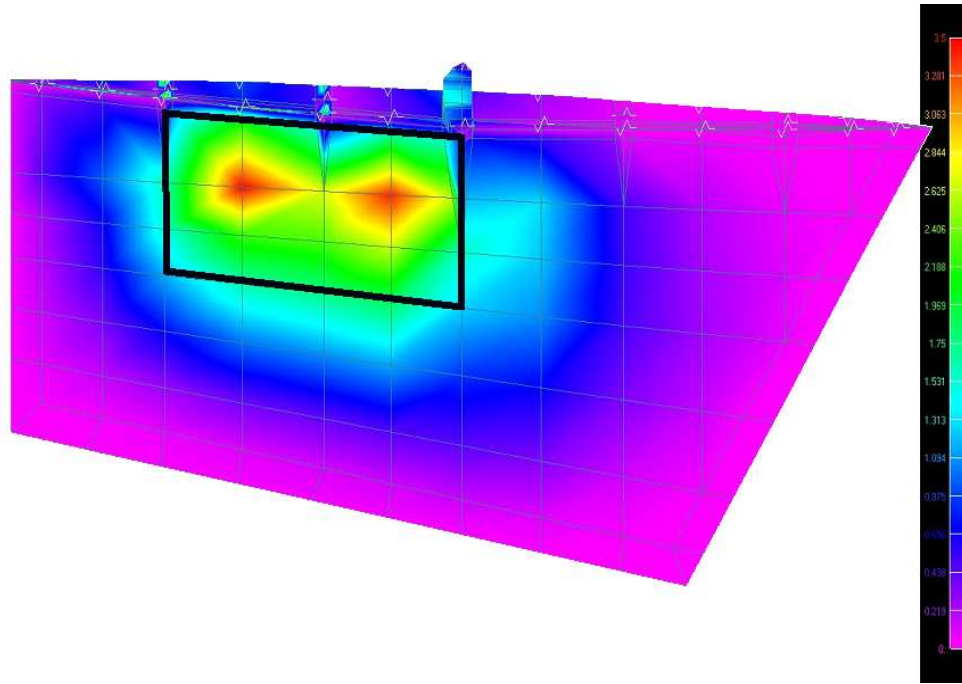
Figure 5.13:   Mode 1 Strain Energy Plot and Suggested Patch Location
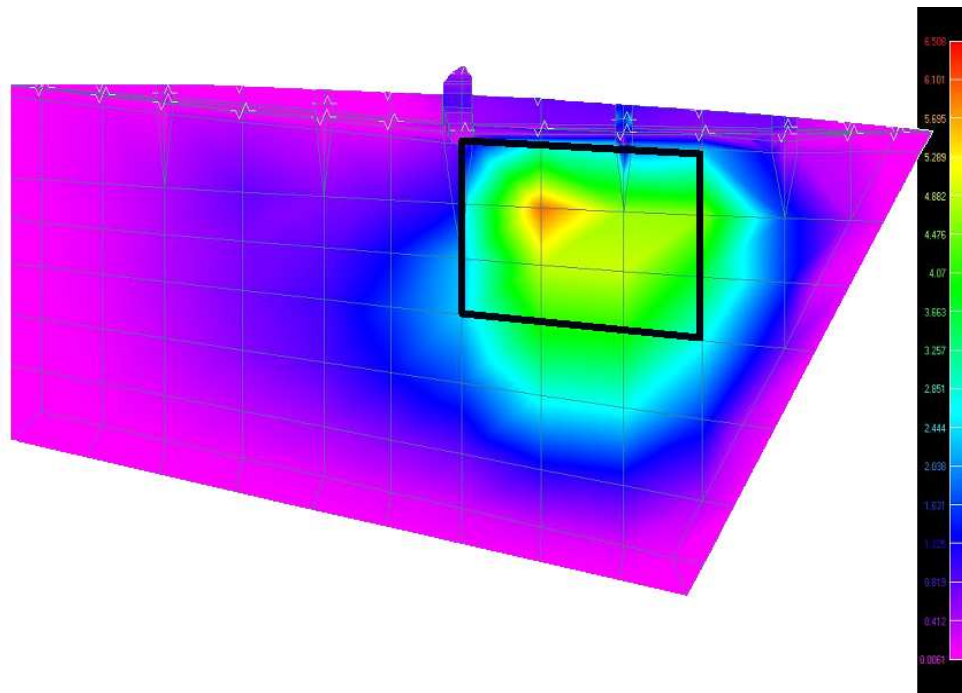
Figure 5.14:   Mode 2 Strain Energy Plot and Suggested Patch Location
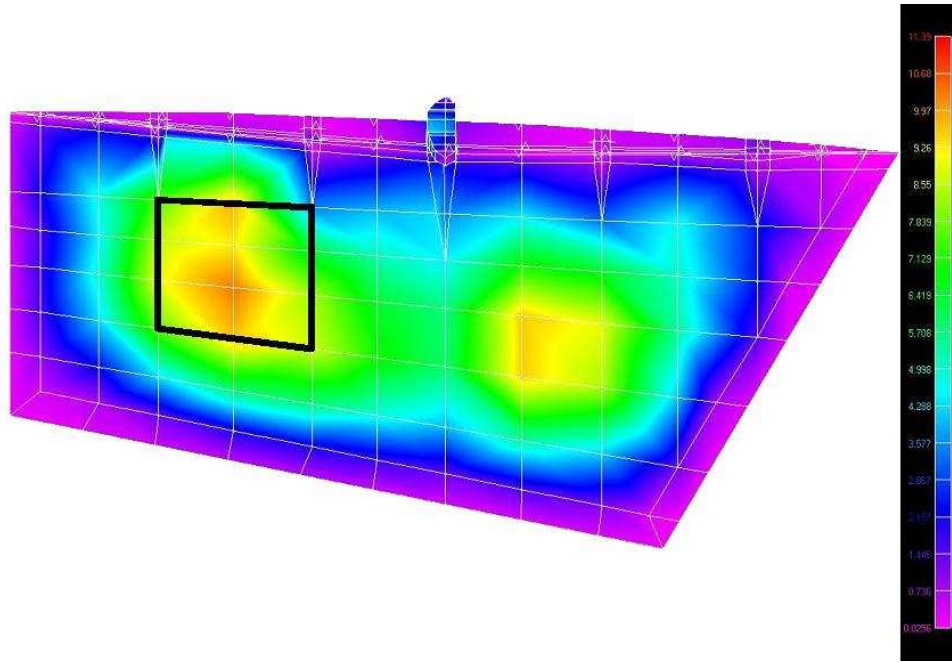
Figure 5.15:   Mode 3 Strain Energy Plot and Suggested Patch Location
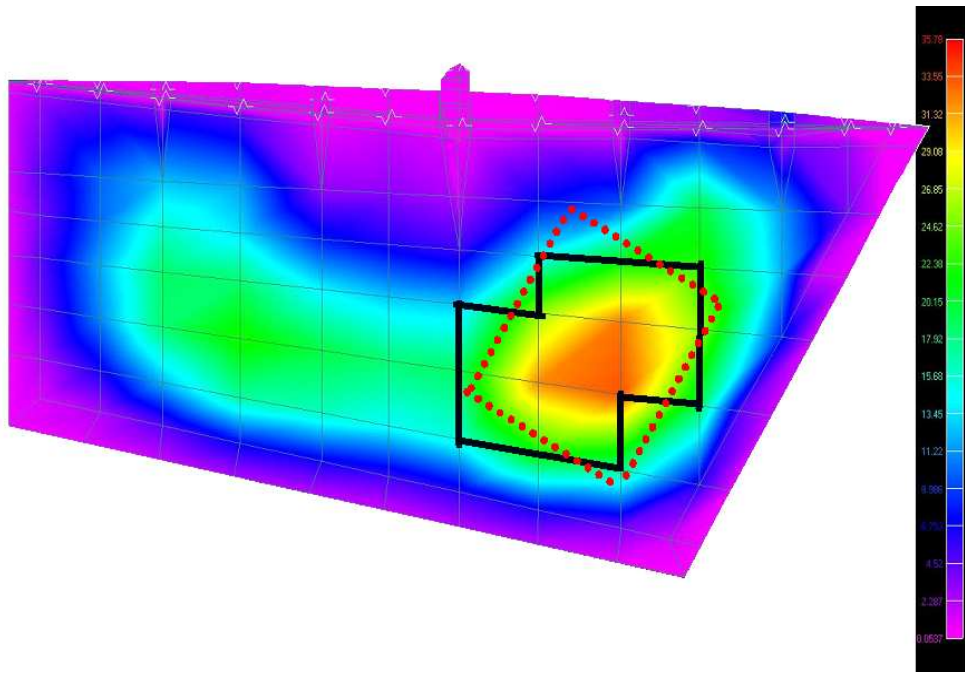
Figure 5.16:   Mode 4 Strain Energy Plot and Suggested Patch Location

Output Set Mode 4, 208.1706 Hz
StdContourVec: Plate Mid MajorPrn Strain
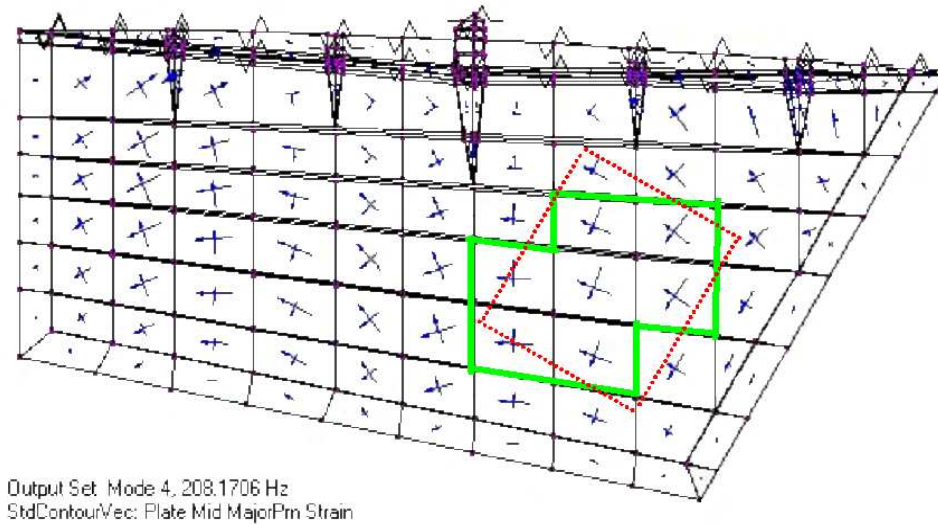
Figure 5.17:   Example of Principal Strain Vector Plot - Mode 4

produced is shown in Figure 5.17. Tables 5.6 and 5.7 summarize the results of the
principle strain analysis including the selected number of patch layers for each mode
and the recommended fiber direction for each patch layer relative the coordinate
system shown in Figure 4.7. Fortunately, the differences between the major strain
vector angles for the non-optimized and optimized versions of the model were generally
less than 7 degrees; the greatest difference was 16.7 degrees for Mode 4.

5.3.2 Implementation within FEM.   A summary of the piezoelectric con-
stants used and the coefficients of thermal expansion resulting from implementation
of the thermal analogy detailed in Section 3.5 are listed in Table 5.8. Note that the

Table 5.6:   Major Principal Strain Angles for Patch Locations

	Mode 1	Mode 2	Mode 3	Mode 4
Non-optimized	145.6 deg	10.2 deg	106.6 deg	142.6 deg
Optimized	138.9 deg	14.4 deg	112.6 deg	159.3 deg

Table 5.7:   Recommended Patch Parameters

	Mode 1	Mode 2	Mode 3	Mode 4
Patch Layers per Side	1	1	2	2
Fiber Direction - 1st Layer	140.0 deg	15.0 deg	110.0 deg	155.0 deg
Fiber Direction - 2nd Layer	N/A	N/A	20.0 deg	65.0 deg

Table 5.8:   MFC Actuator Properties and Coefficients of Thermal Expansion

d_{33} **(Fiber Direction)**	4.0×10^2 pC/N
d_{31} **(Electrode Direction)**	-1.7×10^2 pC/N
α_{33} **(Fiber Direction)**	1.312×10^{-6} in/Δ deg
α_{31} **(Electrode Direction)**	-5.58×10^{-7} in/Δ deg

Smart Material corporation's actuator data sheet was used to obtain the actuator properties and "low-field" electrical constants were assumed [29]. Given the thickness of the actuators, they will likely always be operating at less than 300 Volts which is the cut-off between high and low-field operation.

Successful integration of the actuator patches for each mode as well as implementation of the thermal analogy was verified through visual analysis of the ventral fin FEM deflections resulting from simulated input of a 150 Volt signal. Figures 5.18 through 5.21 show the resulting deflections in comparison with published GVT data. For Mode 1, the deflection produced by the actuator patch closely approximated the known mode shape. For Modes 2 through 4, the patch configurations simply were not capable of replicating the complex shape characteristic of those higher frequency vibration modes. They did, however, closely match the mode shapes within their specific regions of application, thereby meeting the objective of countering principal strains within the areas of highest strain density.
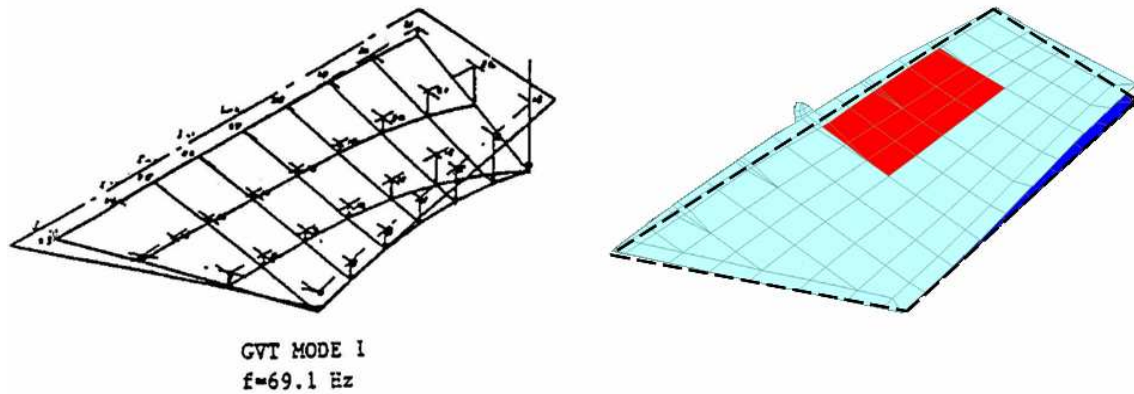
Figure 5.18:   Mode 1 Patch Deflection
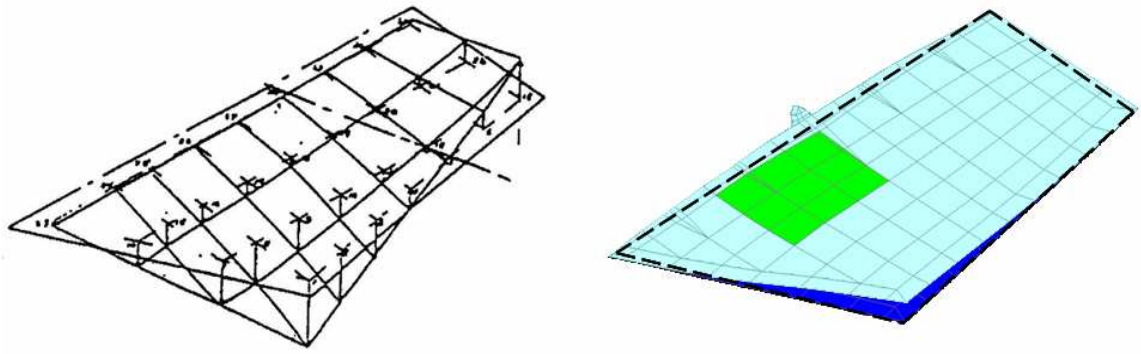
Figure 5.19:   Mode 2 Patch Deflection
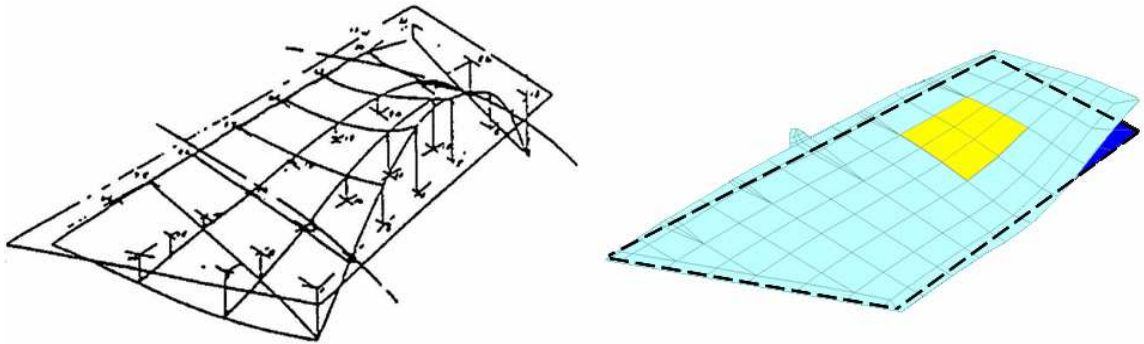
Figure 5.20:   Mode 3 Patch Deflection
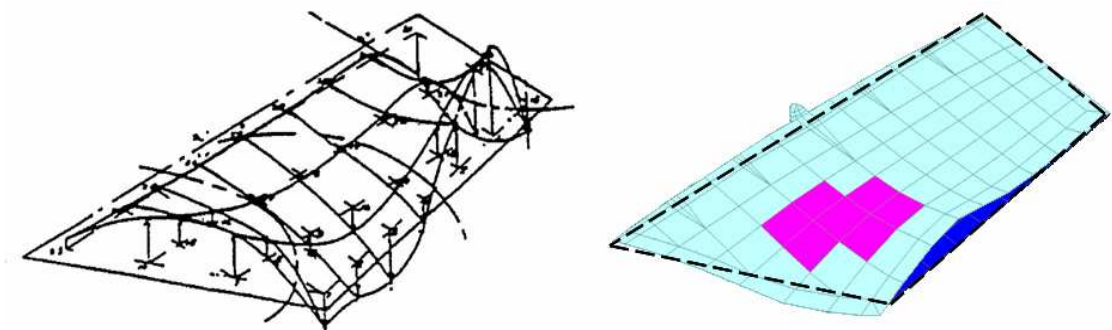
Figure 5.21:   Mode 4 Patch Deflection

The results of the modal analysis conducted to determine the extent to which each possible two-mode combination of patches increased the stiffness of the optimized FEM and, therefore, the modal frequencies, are summarized in Table 5.9. The predicted increases in stiffness were fairly negligible with an overall average frequency increase of 2.44 percent. The greatest percentile increase occurred for Mode 2 using the actuator patch combination for Modes 2 and 4. The predicted modal frequency increase for that particular case was approximately 4.28 percent. These results supported a decision to proceed with the final phase of critical mode selection, under the assumption that stiffness increases resulting from piezoelectric patch integration within the FEM would have a minimal impact on the results of the ZAERO ASE analysis.

Although the actuator patch implementation process was very successful, it would have been beneficial to investigate several other concepts including: the effects of adding additional layers of actuator patches, use of variable fiber angles within each patch application area since the principal strain vectors varied within each area, and estimation of the specific power requirements for the proposed patch layouts using frequencies and deflections to determine the energy used over a given time period.

Table 5.9:   Modal Frequencies for Possible Actuator Patch Combinations

Patch Combination	Mode 1 (Hertz)	Mode 2 (Hertz)	Mode 3 (Hertz)	Mode 4 (Hertz)
None (Fin Only)	69.1	88.6	140.6	208.2
Modes 1 & 2	71.2	91.5	143.2	210.6
Modes 1 & 3	71.6	89.4	144.9	211.5
Modes 1 & 4	71.1	90.3	144.6	214.5
Modes 2 & 3	70.1	91.4	144.2	211.6
Modes 2 & 4	69.6	92.3	143.7	214.4
Modes 3 & 4	70.1	90.1	145.7	215.7

5.4 Critical Mode Selection Revisited

The second attempt at critical mode selection provided additional insight into determination of which modes would be the most appropriate for demonstration of the effectiveness of piezoelectric actuators in future flight testing. The ZAERO ASE analysis demonstrated the potential effectiveness of Mode 1 and 2 patches for increasing the stability of their respective modes using a simple control algorithm, and it also showed that Modes 2 and 4 were in the greatest need of actuator patches to preserve their aeroelastic stability. Subsequently, analysis of PSD plots produced by TPS during ALC testing showed that Modes 1 and 4 were the most observable in terms of their power magnitudes in comparison with the other modes. This was due to the location of the instrumentation used to collect the data. The PSD plots also provided evidence that the natural modes of vibration for the actual ventral fin were significantly different than those predicted by the optimized ventral fin FEM.

5.4.1 Zona ZAERO ASE Analysis. Figures 5.22 through 5.24 depict the results of the ZAERO ASE analysis for all three sets of patches. Overall, the patches for Modes 1 and 2 appeared to be the most effective in consideration of the fact that changes in gain for each set correlated with a strong potential for an increase in stability of the respective mode. However, Modes 2 and 4 were in most need of patches to preserve stability due to their smaller stability margin based on the aerodynamic damping. Therefore, Modes 2 and 4 were tentatively selected as the most critical modes pending a review of the data gathered from the actual ventral fin during TPS ALC testing in October of 2005.

Although the ASE analysis proved to be useful, the configuration of the control scheme was not optimal. If additional ASE analyses are conducted in the future, a band-pass filter should be incorporated into the control scheme following the sensor. Using the current control scheme, the accelerometers sense the frequencies for all of the vibration modes when they should only be sensing a specific frequency range for each patch.
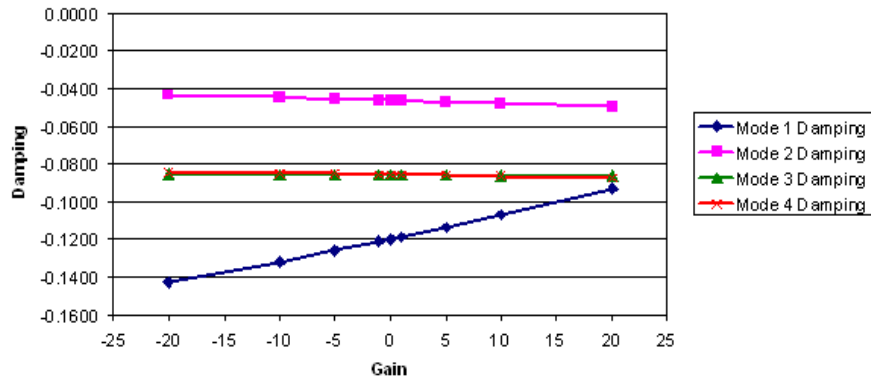
Figure 5.22:   Results of ZAERO ASE Analysis Using Mode 1 Patches
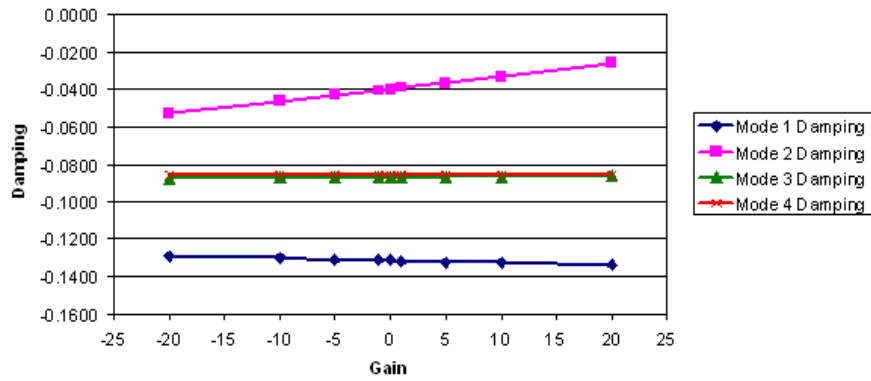
Figure 5.23:   Results of ZAERO ASE Analysis Using Mode 2 Patches
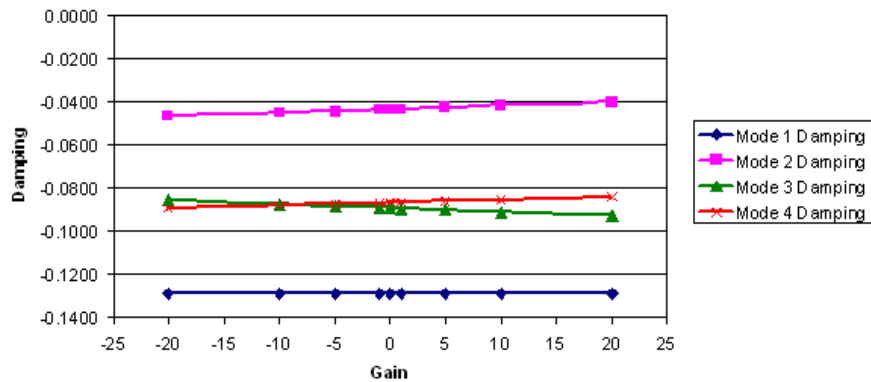
Figure 5.24:   Results of ZAERO ASE Analysis Using Mode 4 Patches

5.4.2 ALC Flight Testing. Analysis of the PSD plots produced during TPS ALC testing proved to be very useful. The plots generated from the strain gage data, as shown by the examples in Figures 5.25 and 5.26, clearly showed Mode 1 to be most dominant. Of the 48 plots reviewed, Mode 1 had the highest power in 47 of them, with Mode 2 being the second most dominant mode over 50 percent of the time. However, as the Mach number increased for a given altitude, the frequency peaks for Mode 2 appeared to shrink and become insignificant in comparison with the Mode 1 peaks.
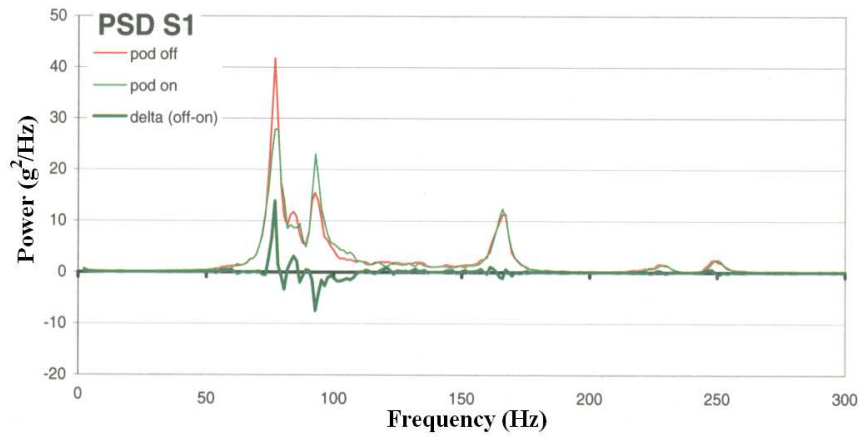
Figure 5.25:   Strain Gage PSD Plot - 10,000 ft, 0.4 Mach [14]
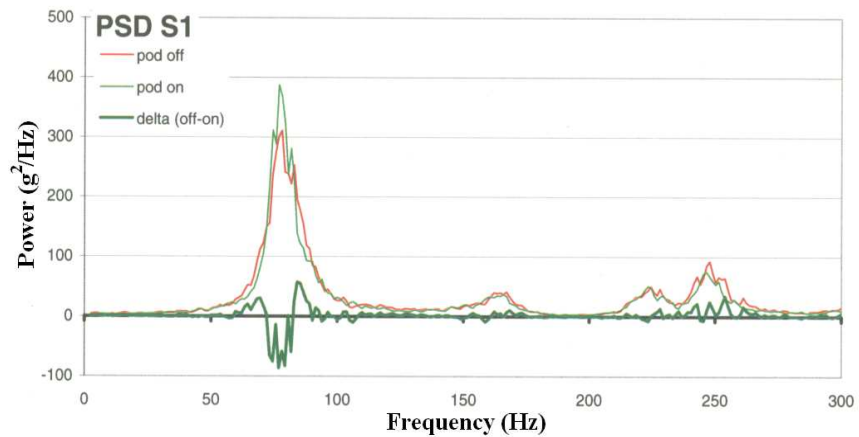
Figure 5.26:   Strain Gage PSD Plot - 10,000 ft, 0.85 Mach [14]

Similar characteristics were observed in the plots generated from the forward accelerometer as shown in Figures 5.27 and 5.28. Mode 3 was generally the second most dominant mode at Mach numbers below 0.7, and Mode 5 was generally the second most dominant mode at Mach numbers at or above 0.7.

Without question, the location of the strain sensor adjacent to the central mounting bracket and the location of the forward accelerometer as depicted in Figure 4.6 played a significant role in their ability to sense particular modes. As a result, the instrumentation showed different modes to be most dominant for equivalent flight conditions. So although Modes 1 and 4 appeared to be most the most dominant, it is very likely that they were simply the most observable for their respective sensors.
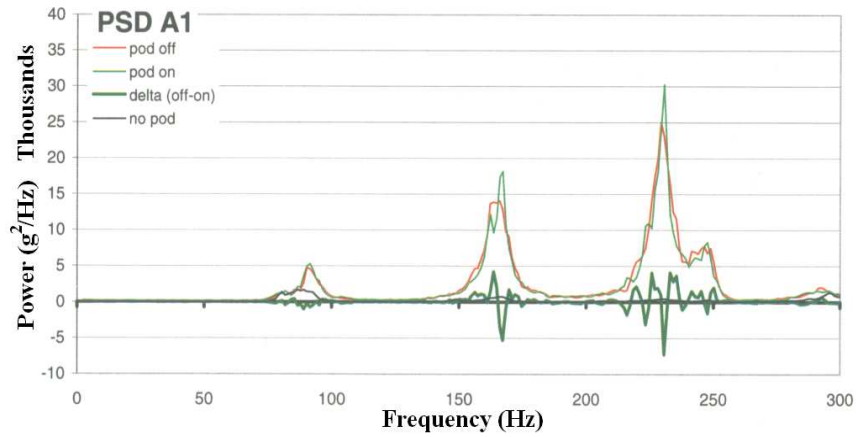
Figure 5.27:   Forward Accelerometer PSD Plot - 10,000 ft, 0.5 Mach [14]
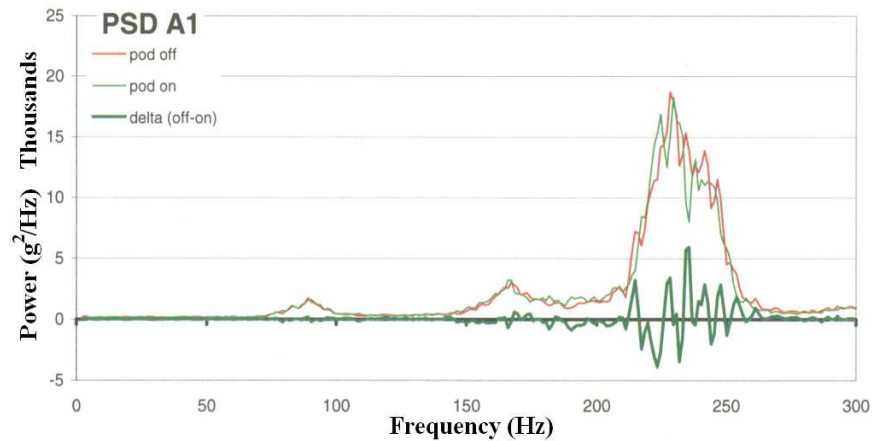
Figure 5.28:   Forward Accelerometer PSD Plot - 10,000 ft, 0.85 Mach [14]

Consideration of both the ZAERO ASE analysis results and the PSD plots from the TPS ALC testing provided additional justification for selecting Modes 1, 2 and 4 as the most critical ventral fin vibration modes. However, it was not possible to say with absolute certainty that any two of those modes were more critical than the other. In order to make such a determination, the observability of each mode given the existing instrumentation locations will need to be determined and compared.

The natural frequencies of the first five modes of vibration, as summarized in Figure 5.29, Figure 5.30 and Table 5.10, were found to be significantly different than the historical values for the Block 15 GVT, the Block 30 NASTRAN FEM, and the optimized version of the ventral fin FEM used throughout this research. The reason
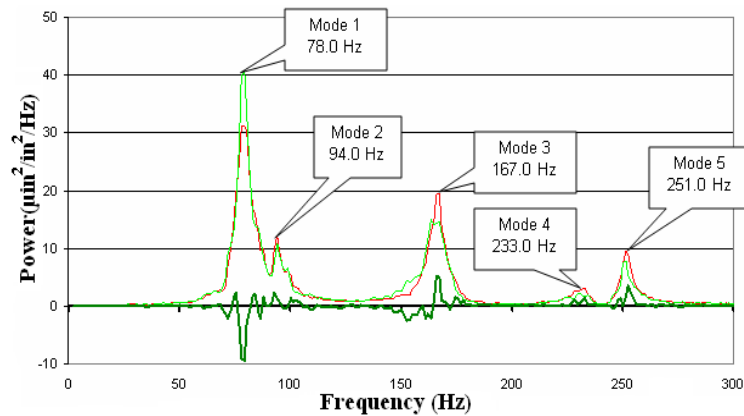
Figure 5.29:   Natural Modes via Strain Gage - 20,000 feet, 0.6 Mach [14]
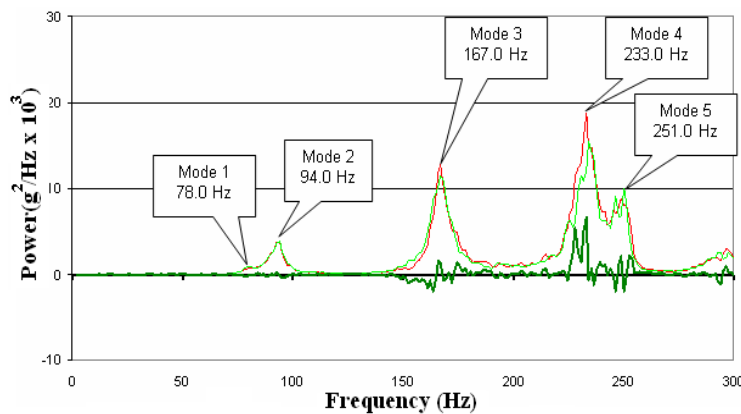
Figure 5.30:   Natural Modes via Forward Accelerometer - 20,000 feet, 0.6 Mach [14]

5-23

Table 5.10:   Ventral Fin Modal Characteristics versus Historical Data and FEM

	Mode 1	Mode 2	Mode 3	Mode 4	Mode 5
Block 15 GVT	69.1 Hz	87.1 Hz	155.3 Hz	210.5 Hz	N/A
Block 30 NASTRAN	68.7 Hz	88.5 Hz	140.7 Hz	197.9 Hz	212.4 Hz
Optimized FEM	69.1 Hz	88.6 Hz	140.6 Hz	208.2 Hz	248.2 Hz
Actual Ventral Fin	78.0 Hz	94.0 Hz	167.0 Hz	233.0 Hz	251.0 Hz

for those differences is not fully understood, though it could have been due to structural differences between the actual ventral fin and the FEM. Regardless, it would be beneficial to conduct a GVT of the actual ventral fin and use the resulting data for comparison to the modal characteristics of the FEM. After performing the comparison, further refinement of the model and reaccomplishment of the design and implementation process for the actuator patches would likely be required to ensure optimal effectiveness of the patches when they are eventually manufactured and tested.

VI. Summary and Recommendations

The overall objective of the research presented in this thesis was to determine which natural modes of vibration were the most critical in the buffet response of the F-16 ventral fin, and design piezoelectric actuators capable of reducing that buffet in support of future flight testing and subsequent technology development. The steps which were accomplished in order to meet that objective resulted in the successful development and analysis of a useful ventral fin FEM, an initial determination of the three most critical vibration modes in the buffet response of the ventral fin, a successful design and integration process for incorporating piezoelectric actuators into the FEM, and a final confirmation of the three most critical, or at least the most suitable, modes for follow-on research and testing. The results of this research will provide a solid foundation from which to develop and conduct the additional research necessary to ensure successful flight testing and evaluation of active structural control technology.

6.1 Summary

The primary goal of this research was to obtain an accurate FEM of a Block 15 ventral fin which would be representative of the actual test article to be used in future flight testing. Although an existing Block 15 FEM was not available, the alteration, tuning, and optimization procedures documented in this thesis were shown to be sufficient for converting an existing Block 40 model into a usable, representative Block 15-representative model. Manual tuning of the model through the use of springs attached to the mounting surface was found to be marginally effective, since only the first two modes of vibration were tunable to published modal data. However, the SOL 200 optimization routine within MSC.Nastran was found to be effective for tuning each of the first four modes while using the spring constants for the aforementioned springs as well as the skin thicknesses of each skin element as design variables. Subsequently, the mode shapes for each of the first four modes of the optimized model were found to be in very close agreement with published modal data.

6-1

Selection of the two most critical vibration modes in the buffet response of the ventral fin was a significant challenge. A review of the PSD plots from three sources of historical flight test data showed Modes 1, 2 and 4 to be the most dominant in terms of relative power magnitudes, but was insufficient for determining the two most critical modes amongst those three. Comparisons of strain energy plots from the ventral fin FEM to the geometric characteristics of historically documented failures were, however, quite revealing as they showed a strong correlation between the typical failure "shape" of actual ventral fins and the Mode 4 strain energy distribution. Still, the comparisons were inadequate for eliminating one of the other two modes.

The initial ZAERO analyses conducted on the non-optimized version of the ventral fin FEM indicated the possibility of a Mode 3 instability. That result provided the necessary justification for tuning the FEM using an optimization routine since the natural frequency of vibration for Mode 3 of the non-optimized model was inaccurate in comparison with published data. Further ZAERO analyses using the optimized model indicated the possibility of a Mode 2 instability at a dynamic pressure corresponding to an altitude of approximately -90,000 feet MSL at 0.95 Mach. However, Modes 1 through 4 were all predicted to be contributors to the instability. So although the analyses supported selection of Mode 2 as one of the most critical modes, they did not provide the degree of justification required to eliminate Mode 1 or 4. In retrospect, it may have proved useful to conduct additional analyses using finer aerodynamic grids until changes in the predicted instability frequency were less than five percent from one run to the next. As a minimum, conducting additional analyses with a refined aerodynamic grid would have provided additional confidence in the accuracy and applicability of the ZAERO results.

The design and integration of suitable piezoelectric actuator patches within the ventral fin FEM was successfully accomplished while taking into account existing instrumentation locations. Visual evaluation of strain energy plots from the optimized model provided a clear indication of the regions of highest strain energy density and, thus, the ideal locations for actuator patch placement for each of the first four modes

of vibration. Comparisons of the principal strain vectors for each mode from both the optimized and non-optimized versions of the FEM showed that the skin thickness changes implemented within the optimized model did not result in significant changes to the predicted directions of principal strain. Additionally, manual measurement of the vector angles using the newly defined actuator patch coordinate system proved to be an effective method for determining and designating the fiber angles for each patch layer within the FEM. Use of a thermal analogy within NASTRAN to simulate the piezoelectric characteristics of the patches was also found to be highly effective. The fin deflections resulting from the application of a simulated voltage to each individual patch closely approximated the characteristic ventral fin mode shapes within the specific regions of actuator patch application. Finally, each possible two-mode combination of patches was found to have a minimal effect on the stiffness of the ventral fin FEM and, therefore, the natural frequencies of vibration. Although the actuator patch implementation process was very successful, it would have been beneficial to investigate several other concepts including: the effects of adding additional layers of actuator patches, estimation of the interlaminar shear between the patches and the FEM skin elements, use of variable fiber angles within each patch application area since the principal strain vectors were varied within each area, and estimation of the specific power requirements for the proposed patch layouts using frequencies and deflections to determine the energy used over a given time period.

The research concluded with the second phase of critical mode selection, which was found to be as challenging as the first. Although the ZAERO ASE analysis demonstrated the potential effectiveness of Mode 1 and 2 patches for increasing the stability of their respective modes using a simple control algorithm, it also showed that Modes 2 and 4 were in the greatest need of actuator patches to preserve their aeroelastic stability. The ZAERO ASE analysis methodology could have been improved by incorporating a band-pass filter into the control scheme to ensure the accelerometers were sensing the appropriate frequencies for each set of patches.

In order to attempt to arrive at a final decision regarding the two most critical modes of vibration, PSD plots produced by TPS during the timeframe of this research were analyzed. The plots produced from strain gage and forward accelerometer flight test data showed that Modes 1 and 4 were the most observable, respectively, in terms of their power magnitudes. However, this was likely due to the location of the instrumentation used to obtain the data.

The TPS data also provided evidence that the natural modes of vibration for the actual ventral fin were significantly different than those predicted by the optimized ventral fin FEM. The reason for those differences is not fully understood, though it could have been due to structural differences between the actual ventral fin and the FEM. Regardless, it would be beneficial to conduct a GVT of the actual ventral fin and use the resulting data for comparison to the modal characteristics of the FEM.

6.2   Recommendations

In consideration of the aforementioned conclusions, the following recommendations are presented for future research and development of the technology needed to alleviate buffet-induced ventral fin vibration through the use of piezoelectric actuators.

1. Conduct a GVT on the actual ventral fin which will be used for flight testing.

2. Refine the FEM to match the modal parameters obtained from the GVT on the actual ventral fin.

3. Reaccomplish the process for locating and integrating the piezoelectric actuator patches within the FEM.

4. Calculate the observability of Modes 1, 2 and 4 for the existing instrumentation configuration of the actual ventral fin in order to determine which two modes are the most critical.

5. Investigate the potential benefits and drawbacks of adding additional layers of actuator patches for each mode.

6. Investigate the feasibility and benefits of using variable actuator fiber angles within each patch application area since the strain angles vary within each region.

7. Construct and implement a final actuator patch design, taking into account the previous recommendations.

8. Conduct an estimation of the actual power requirement for the preferred piezo-electric actuator patch combination and layout. One possible approach would be to determine the strain energy expended over a given period of time through identification of fin deflections for the frequencies of interest.

9. Conduct additional ZAERO analyses, as required for confirmation of the two most critical modes, using progressively finer aerodynamic grids until the results converge to within 5 percent change from one analysis to the next. This will provide additional confidence in the accuracy and applicability of the ZAERO results.

10. Incorporate a band-pass filter into the control scheme prior to conducting further analyses using the ZAERO ASE module. The recommended control schematic is depicted in Figure 6.1, where the transfer function for the bandpass filter is of the form

$$TF(s) = K\frac{(s^2 + 2\zeta_{num}\omega_n + \omega_n^2)}{s^2 + 2\zeta_{den}\omega_n + \omega_n^2} \tag{6.1}$$

K is the gain for transfer function, ζ_{num} and ζ_{den} are damping ratios for the numerator and denominator of the transfer function, and ω_n is the frequency for the vibration mode of interest. The recommended values for K, ζ_{num} and ζ_{den} are 0.2, 0.25 and 0.05 respectively. Although it is possible to enter a specific transfer function for the piezoelectric actuator, the default ASE module actuator transfer function can be used with minimal impact to the dynamics of the control system [37, page 4-42].
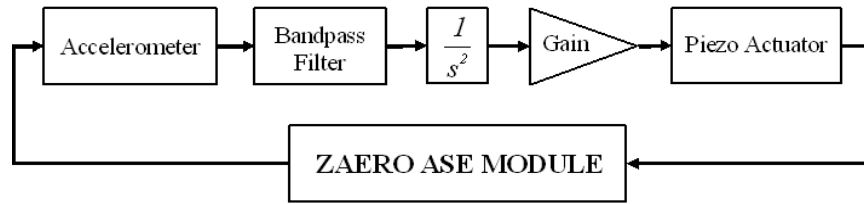
Figure 6.1:   Recommended ZAERO ASE Module Control Schematic

11. Design and implement the actual control system after the actuators have been
    built and applied to the ventral fin. A suggested feedback control loop is shown
    in Figure 6.2, in which $\ddot{z}$ represents the acceleration perpendicular to the sur-
    face of the ventral fin. The transfer function for the bandpass filter should be
    of the same format as that shown in equation (6.1). The transfer function for
    the piezoelectric actuator would relate a change in strain within the actuator
    to the position of the accelerometer, and the transfer function for the ventral
    fin would relate the acceleration of the sensor to the change in strain of the
    actuator. Those two transfer functions, or their combined effect, can be deter-
    mined experimentally after the actuators are applied to the actual ventral fin
    as discussed by Robert Moses [17].
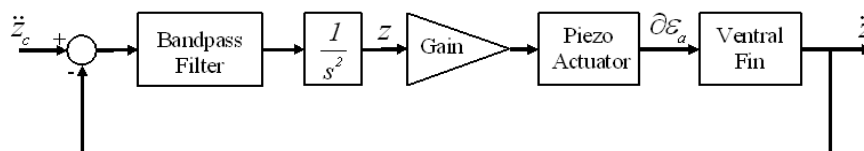
Figure 6.2:   Recommended Feedback Control Loop

Appendix A. Finite Element Model and ZAERO Codes

A.1 Optimized Ventral Fin FEM Code

The following code is an abbreviated version of that used to determine the modal characteristics of the optimized ventral fin FEM.

```
$   EXECUTIVE CONTROL   $
ID THESIS, VENTRAL FIN OPTIMIZED
SOL SEMODES
CEND


$   CASE CONTROL   $
TITLE = MODE DETERMINATION
SUBTITLE = COUPLED MASS
SPC = 10
METHOD = 20
DISP = ALL
STRESS = ALL
STRAIN = ALL
ESE = ALL
ECHO = SORT


BEGIN BULK

$   PROCESSING PARAMETERS   $
PARAM,POST,-1
PARAM,OGEOM,NO
PARAM,AUTOSPC,YES
PARAM,K6ROT,100.
PARAM,MAXRATIO,1.E+8
PARAM,GRDPNT,0
PARAM,COUPMASS, -1
PARAM,WTMASS, 0.002588
```

```
$   COORDINATE SYSTEM DEFINITIONS    $
CORD2R      9000       0   398.8 -17.385  -27.46  430.55 252.494 266.232+CS  6Y0
+CS  6Y0 797.533-46.2946-44.0008
CORD2R      9001       0   418.06 -14.696 -27.644 405.545 273.152 276.891+CS  6Y1
+CS  6Y1 834.056-42.8428 16.0562




$*******************************************************
$*     ADDITIONAL PROPERTY, MATERIAL, CONSTRAINT        *
$*     GRID POINT, AND ELEMENT DEFINITIONS GO HERE      *
$*******************************************************

$   TUNING SPRINGS    $
cELAS1, 301, 5000, 910380, 3, 945380, 3
CELAS1, 302, 5000, 910280, 3, 945280, 3
CELAS1, 303, 5000, 910379, 3, 945379, 3
CELAS1, 304, 5000, 910279, 3, 945279, 3
CELAS1, 305, 5000, 910278, 3, 945278, 3
CELAS1, 306, 5000, 910378, 3, 945378, 3
CELAS1, 307, 5000, 910277, 3, 945277, 3
CELAS1, 308, 5000, 910377, 3, 945377, 3
CELAS1, 309, 5000, 910276, 3, 945276, 3
CELAS1, 310, 5000, 910376, 3, 945376, 3
CELAS1, 311, 5000, 910275, 3, 945275, 3
CELAS1, 312, 5000, 910375, 3, 945375, 3

CELAS1, 313, 5001, 910443, 3, 945512, 3
CELAS1, 314, 5001, 910449, 3, 945511, 3

CELAS1, 315, 5002, 910273, 3, 945273, 3
CELAS1, 316, 5002, 910373, 3, 945373, 3
CELAS1, 317, 5002, 910272, 3, 945272, 3
CELAS1, 318, 5002, 910372, 3, 945372, 3
CELAS1, 319, 5002, 910271, 3, 945271, 3
CELAS1, 320, 5002, 910371, 3, 945371, 3
```

```
CELAS1, 321, 5002, 910292, 3, 945292, 3
CELAS1, 322, 5002, 910392, 3, 945392, 3
CELAS1, 323, 5002, 910291, 3, 945291, 3
CELAS1, 324, 5002, 910391, 3, 945391, 3
CELAS1, 325, 5002, 910290, 3, 945290, 3
CELAS1, 326, 5002, 910390, 3, 945390, 3


$   OPTIMIZED TUNING SPRING PROPERTY FIELDS   $
PELAS, 5000, 120435.9
PELAS, 5001, 5026000.
PELAS, 5002, 7.2E13


$   OPTIMIZED SKIN ELEMENT PROPERTY FIELDS   $
PSHELL    909210    91030.028443    9103    1.                    0.
PSHELL    909213    91030.034401    9103    1.                    0.
PSHELL    909810    9803 0.10393    9803    1.                    0.
PSHELL    911401    93010.077375    9301    1.                    0.


$   MODAL ANALYSIS FOR THE FIRST FIVE MODES OF VIBRATION   $
EIGRL, 20, , , 5, , , , MAX


ENDDATA
```

A.2 FEM Code for Piezoelectric Actuator Patches

The following codes are an example of those used to integrate the piezoelectric actuator patches into the optimized ventral fin FEM.

A.2.1 Main Code for Mode 1.

```
$   EXECUTIVE CONTROL   $
ID THESIS, VENTRAL FIN WITH PATCHES
SOL SESTATIC
CEND


$   CASE CONTROL   $
TITLE = STATIC DEFLECTION CHECK
SUBTITLE = MODE 1
SPC = 10
$METHOD = 20
TEMPERATURE(LOAD) = 30
DISP = ALL
STRESS = ALL
STRAIN = ALL
ESE = ALL
ECHO = SORT


BEGIN BULK

$   DEFINE NEW COORD SYSTEM TO SPECIFY FIBER DIRECTION IN PIEZO ELEMENT   $
CORD2R, 1, , 444.99, -21.918, -43.955, 444.99, -20.918, -43.955, +C1A
  +C1A, 444.99, -21.918, -44.955

$   LOAD MODE 1 PATCH DEFINITION FILE   $
INCLUDE 'mode1patchstatic.dat'

$   DEFINE THE PIEZO MATERIAL PROPERTIES   $
MAT8, 5000, 4.4005E6, 2.3148E6, 0.31, 8.0061E5, , , , +M8A
  +M8A,  1.312E-6, -5.58E-7
```

A-4

```
$   DEFAULT TEMPERATURE FOR NON-SPECIFIED ELEMENTS   $
TEMPD, 30, 0.0


$***********************************************************
$*             BEGIN ORIGINAL STRUCTURAL FILE            *
$***********************************************************
```

A.2.2   Patch Definition Code for Mode 1.

```
$   DEFINE THE PIEZO PATCH ELEMENTS FOR MODE 1   $
CTRIA3, 1, 10140, 917071, 917072, 910358, 1, 0.0265
CQUAD4, 2, 10140, 910357, 910358, 917071, 917068, 1, -0.0265
CQUAD4, 3, 10140, 910356, 910357, 917068, 917064, 1, -0.0265
CTRIA3, 4, 10140, 917062, 917064, 910356, 1, 0.0265
CTRIA3, 5, 10140, 917060, 917062, 910356, 1, 0.0265
CQUAD4, 6, 10140, 910355, 910356, 917060, 917039, 1, -0.0265
CQUAD4, 7, 10140, 910485, 910355, 917039, 917037, 1, -0.0265
CQUAD4, 8, 10140, 910354, 910485, 917037, 917035, 1, -0.0265
CQUAD4, 9, 10140, 910357, 910358, 910348, 910347, 1, 0.0265
CQUAD4, 10, 10140, 910356, 910357, 910347, 910346, 1, 0.0265
CQUAD4, 11, 10140, 910355, 910356, 910346, 910345, 1, 0.0265
CQUAD4, 12, 10140, 910485, 910355, 910345, 910344, 1, 0.0265
CTRIA3, 13, 10140, 910354, 910485, 910344, 1, 0.0265
CQUAD4, 14, 10140, 910347, 910348, 910338, 910337, 1, 0.0265
CQUAD4, 15, 10140, 910346, 910347, 910337, 910336, 1, 0.0265
CQUAD4, 16, 10140, 910345, 910346, 910336, 910335, 1, 0.0265
CQUAD4, 17, 10140, 910344, 910345, 910335, 910334, 1, 0.0265
CQUAD4, 18, 10140, 910482, 910254, 917034, 917036, 1, -0.0265
CQUAD4, 19, 10140, 910255, 910482, 917036, 917038, 1, -0.0265
CQUAD4, 20, 10140, 910256, 910255, 917038, 917061, 1, -0.0265
CTRIA3, 21, 10140, 917061, 917063, 910256, 1, -0.0265
CTRIA3, 22, 10140, 917063, 917065, 910256, 1, -0.0265
CQUAD4, 23, 10140, 910257, 910256, 917065, 917066, 1, -0.0265
CQUAD4, 24, 10140, 910258, 910257, 917066, 917069, 1, -0.0265
CTRIA3, 25, 10140, 917069, 917074, 910258, 1, -0.0265
```

```
CTRIA3, 26, 10140, 910254, 910482, 910244, 1, -0.0265
CQUAD4, 27, 10140, 910482, 910255, 910245, 910244, 1, -0.0265
CQUAD4, 28, 10140, 910255, 910256, 910246, 910245, 1, -0.0265
CQUAD4, 29, 10140, 910256, 910257, 910247, 910246, 1, -0.0265
CQUAD4, 30, 10140, 910257, 910258, 910248, 910247, 1, -0.0265
CQUAD4, 31, 10140, 910244, 910245, 910235, 910234, 1, -0.0265
CQUAD4, 32, 10140, 910245, 910246, 910236, 910235, 1, -0.0265
CQUAD4, 33, 10140, 910246, 910247, 910237, 910236, 1, -0.0265
CQUAD4, 34, 10140, 910247, 910248, 910238, 910237, 1, -0.0265


$   MODE 1 PIEZO PCOMP PROPERTIES - PROPERTY NUMBER INFERS FIBER ANGLE   $
PCOMP, 10140, -0.006, , , , 0.0, , , +PCA
  +PCA, 5000, 0.012, 140.0


$   FORM TEMPERATURE ANALOGY TO REPRESENT VOLTAGE LOAD IN MODE 1 PIEZOS   $
TEMPP1, 30, 1, 150.0, , , , , , , +TPA
  +TPA, 2, THRU, 17
TEMPP1, 30, 18, -150.0, , , , , , , +TPB
  +TPB, 19, THRU, 34
```

A-6

A.3 ZAERO Flutter Analysis Code

The following code is an example of those used to conduct the flutter analyses which were employed during the first phase of critical mode selection. The particular code shown is the one used to detect a Mode 2 instability for the optimized ventral fin FEM at 0.95 Mach and a dynamic pressure corresponding to approximately -90,000 feet MSL.

```
$   EXECUTIVE CONTROL    $
ASSIGN FEM=optimizedfin2.f06, PRINT=0, FORM=MSC, BOUND=SYM
DIAG 1
CEND

$   CASE CONTROL    $
TITLE= SUBSONIC FLUTTER ANALYSIS
SUBTIT= VENTRAL FIN (ZONA6 METHOD)
ECHO = SORT
SUBCASE = 1
LABEL = MATCH POINT FLUTTER MACH 0.8
FLUTTER = 10000
SUBCASE = 2
LABEL = MATCH POINT FLUTTER MACH 0.85
FLUTTER = 20000
SUBCASE = 3
LABEL = MATCH POINT FLUTTER MACH 0.9
FLUTTER = 30000
SUBCASE = 4
LABEL = MATCH POINT FLUTTER MACH 0.95
FLUTTER = 40000

$   BULK DATA    $

BEGIN BULK

CORD2R, 9002, 0, 390.003, -17.561, -27.695, 389.8731, 170.5019, -78.0359, +CS6Y3
+cS6Y3, 398.243, -17.456, -27.241
```

```
AEROZ, 9002, YES, NO, SLIN, IN, 55.0, 23.0, 1265.0, +AZ1
+AZ1, 0.0, 0.0, 0.0


MKAEROZ, 25, 0.25, 0, 0, SAVE, FLUTTER2, 5.AIC, 0, +MK0
+MK0, 0.82, 2.187, 3.554, 4.921, 6.288, 7.655, 9.022, 10.389, +MK1
+MK1, 11.756, 13.12


MKAEROZ, 50, 0.50, 0, 0, SAVE, FLUTTER5, 0.AIC, 0, +MK2
+MK2, 0.82, 1.458, 2.096, 2.734, 3.372, 4.010, 4.648, 5.286, +MK3
+MK3, 5.924, 6.56


MKAEROZ, 55, 0.55, 0, 0, SAVE, FLUTTER5, 5.AIC, 0, +MK4
+MK4, 0.82, 1.391, 1.962, 2.533, 3.104, 3.675, 4.246, 4.817, +MK5
+MK5, 5.388, 5.96


MKAEROZ, 60, 0.60, 0, 0, SAVE, FLUTTER6, 0.AIC, 0, +MK6
+MK6, 0.82, 1.336, 1.852, 2.368, 2.884, 3.400, 3.916, 4.432, +MK7
+MK7, 4.948, 5.47


MKAEROZ, 65, 0.65, 0, 0, SAVE, FLUTTER6, 5.AIC, 0, +MK8
+MK8, 0.82, 1.289, 1.758, 2.227, 2.696, 3.165, 3.634, 4.103, +MK9
+MK9, 4.572, 5.05


MKAEROZ, 70, 0.70, 0, 0, SAVE, FLUTTER7, 0.AIC, 0, +MK10
+MK10, 0.82, 1.249, 1.678, 2.107, 2.536, 2.965, 3.394, 3.823, +MK11
+MK11, 4.252, 4.68


MKAEROZ, 75, 0.75, 0, 0, SAVE, FLUTTER7, 5.AIC, 0, +MK12
+MK12, 0.82, 1.23, 1.64, 2.05, 2.46, 2.87, 3.28, 3.69, +MK13
+MK13, 4.1, 4.51


MKAEROZ, 80, 0.80, 0, 0, SAVE, FLUTTER8, 0.AIC, 0, +MK14
+MK14, 0.82, 0.954, 1.088, 1.222, 1.356, 1.490, 1.624, 1.758, +MK15
+MK15, 1.892, 2.02
```

```
MKAEROZ, 85, 0.85, 0, 0, SAVE, FLUTTER8, 5.AIC, 0, +MK16
+MK16, 0.82, 0.941, 1.062, 1.183, 1.304, 1.425, 1.546, 1.667, +MK17
+MK17, 1.788, 1.90


MKAEROZ, 90, 0.90, 0, 0, SAVE, FLUTTER9, 0.AIC, 0, +MK18
+MK18, 0.82, 0.929, 1.038, 1.147, 1.256, 1.365, 1.474, 1.583, +MK19
+MK19, 1.692, 1.80


MKAEROZ, 95, 0.95, 0, 0, SAVE, FLUTTER9, 5.AIC, 0, +MK20
+MK20, 0.82, 0.918, 1.016, 1.114, 1.212, 1.310, 1.408, 1.506, +MK21
+MK21, 1.604, 1.70


CAERO7, 1000, VENTRAL, 0, 5, 11, 0, 0, 0, +CA1
+CA1, 0.0, 0.0, 0.0, 55.0, 0, 0, , , +CA2
+CA2, 11.6, 23.0, 0.0, 43.4, 0, 0


SPLINE1, 10, , 0, 100, 200, 0.0, 0.01


PANLST1, 100, 1000, 1000, 1039


SET1, 200, 910201, 910202, 910203, 910204, 910205, 910206, 910207, +ST1
+ST1, 910208, 910209, 910210, 910211, 910212, 910213, 910214, 910215, +ST2
+ST2, 910216, 910217, 910218, 910219, 910220, 910221, 910222, 910223, +ST3
+ST3, 910224, 910225, 910226, 910227, 910228, 910229, 910230, 910231, +ST4
+ST4, 910232, 910233, 910234, 910235, 910236, 910237, 910238, 910239, +ST5
+ST5, 910240, 910241, 910242, 910243, 910244, 910245, 910246, 910247, +ST6
+ST6, 910248, 910249, 910250, 910251, 910252, 910253, 910254, 910255, +ST7
+ST7, 910256, 910257, 910258, 910259, 910260, 910271, 910272, 910273, +ST8
+ST8, 910274, 910275, 910276, 910277, 910278, 910279, 910280, 910281, +ST9
+ST9, 910282, 910283, 910284, 910285, 910286, 910289, 910290, 910291, +ST10
+ST10, 910292, 910400, 910402, 910403, 910404, 910405, 910406, 910407, +ST11
+ST11, 910408, 910409, 910410, 910411, 910412, 910413, 910414, 910415, +ST12
+ST12, 910416, 910417, 910418, 910419, 910420, 910421, 910422, 910424, +ST13
+ST13, 917022, 917025, 917026, 917028, 917030, 917032, 917034, 917038, +ST14
```

```
+ST14, 917063, 917066, 917074, 917078, 917081, 917084


$   MATCH-POINT FLUTTER ANALYSIS - SUBCASE 1   $


FLUTTER, 10000, SYM, 500, 0, 0, 0, 0, 0


FIXMATM, 500, 80, 0, SLIN, IN, 20.16, 0, 0, +FH1
+FH1,-114.0E4,-108.0E4,-102.0E4,-96.0E4,-90.0E4,-84.0E4,-78.0E4,-72.0E4,+FH2
+FH2,-66.0E4,-60.0E4,-54.0E4,-48.0E4,-42.0E4,-36.0E4,-30.0E4,-24.0E4,+FH3
+FH3,-18.0E4,-12.0E4,-6.0E4, 0.0, 6.0E4


$   MATCH-POINT FLUTTER ANALYSIS - SUBCASE 2   $


FLUTTER, 20000, SYM, 600, 0, 0, 0, 0, 0


FIXMATM, 600, 85, 0, SLIN, IN, 20.16, 0, 0, +FH1
+FH1,-114.0E4,-108.0E4,-102.0E4,-96.0E4,-90.0E4,-84.0E4,-78.0E4,-72.0E4,+FH2
+FH2,-66.0E4,-60.0E4,-54.0E4,-48.0E4,-42.0E4,-36.0E4,-30.0E4,-24.0E4,+FH3
+FH3,-18.0E4,-12.0E4,-6.0E4, 0.0, 6.0E4


$   MATCH-POINT FLUTTER ANALYSIS - SUBCASE 3   $


FLUTTER, 30000, SYM, 700, 0, 0, 0, 0, 0


FIXMATM, 700, 90, 0, SLIN, IN, 20.16, 0, 0, +FH1
+FH1,-114.0E4,-108.0E4,-102.0E4,-96.0E4,-90.0E4,-84.0E4,-78.0E4,-72.0E4,+FH2
+FH2,-66.0E4,-60.0E4,-54.0E4,-48.0E4,-42.0E4,-36.0E4,-30.0E4,-24.0E4,+FH3
+FH3,-18.0E4,-12.0E4,-6.0E4, 0.0, 6.0E4


$   MATCH-POINT FLUTTER ANALYSIS - SUBCASE 4   $


FLUTTER, 40000, SYM, 800, 0, 0, 0, 0, 0
```

A-10

```
FIXMATM, 800, 95, 0, SLIN, IN, 20.16, 0, 0, +FH1
+FH1,-114.0E4,-108.0E4,-102.0E4,-96.0E4,-90.0E4,-84.0E4,-78.0E4,-72.0E4,+FH2
+FH2,-66.0E4,-60.0E4,-54.0E4,-48.0E4,-42.0E4,-36.0E4,-30.0E4,-24.0E4,+FH3
+FH3,-18.0E4,-12.0E4,-6.0E4, 0.0, 6.0E4


$   PLOT CARDS   $


$   * PLOT AERO MODEL BY PLTAERO *   $
PLTAERO, 11, YES, 0, TECPLOT, VENTAERO, .PLT


$   * PLOT FLUTTER MODE BY PLTFLUT *   $
PLTFLUT, 12, 20000, 1, 8, 0.3, TECPLOT, FLUT1.PL, T


PLTMODE, 13, SYM, 1, , 0.3, FEMAP, MODE1.NE, U
PLTMODE, 14, SYM, 2, , 0.3, FEMAP, MODE2.NE, U


$   * V-G PLOT *   $
PLTVG, 15, 10000, 5, V, FEMAP, Opt80VG1, .NEU
PLTVG, 16, 20000, 5, V, FEMAP, Opt85VG1, .NEU
PLTVG, 17, 30000, 5, V, FEMAP, Opt90VG1, .NEU
PLTVG, 18, 40000, 5, V, FEMAP, Opt95VG1, .NEU


ENDDATA
```

A.4 ZAERO ASE Analysis Code

The following code is an example of those used to conduct the closed loop ASE flutter analyses which were employed during the second phase of critical mode selection. The particular code shown is the one used to investigate the stability of the Mode 1 patch layout at 0.95 Mach using a control system gain of -20.

```
$   EXECUTIVE CONTROL    $
ASSIGN FEM=patch1modecheck2.f06, FORM=MSC, BOUNDARY=SYM, PRINT=0
ASSIGN MATRIX=smgh.mgh, MNAME=SMGH, PRINT=0
ASSIGN MATRIX=mode1def.mgh, MNAME = MODE1DEF, PRINT=0
DIAG 1
CEND


$   CASE CONTROL    $
TITLE= SUBSONIC FLUTTER ANALYSIS
SUBTIT= ASE CONTROL SYSTEM ANALYSIS
ECHO = SORT


$   FOR THIS TEST FILE, THERE IS ONLY ONE SUBCASE - AT 0.95 MACH   $
SUBCASE = 1
LABEL = MATCH POINT FLUTTER MACH 0.95
ASE = 2000


$  BULK DATA  $
BEGIN BULK


$   "NEW" ASE CONTROL SYSTEM ANALYSIS SECTION    $


$   DEFINE AEROELASTICITY RUN OPTIONS    $
ASE, 2000, 2600, 40000, 0, 0, 0


$   PIEZO-ACTUATOR    $
PZTMODE, PATCH1, SYM, MODE1DEF, 2050
ACTU, 2050
```

```
$   SENSOR (ACCELEROMETER)   $
ASESNSR, 2100, 2, 910310, 3


$   CONTROL JUNCTIONS AND COMPONENTS   $
SISOTF, 2150, 2, 0, 0.0, 0.0, 1.0


$   GAINS   $
ASEGAIN, 2250, 2150, 1, 2050, 1, -20.0


$   FIXED CONNECTIONS   $
CONCT, 2300, 2100, 1, 2150, 1


$   SETS OF COMPONENTS OF THE SYSTEM  $
SURFSET, 2350, PATCH1
SENSET, 2400, 2100
TFSET, 2450, 2150
GAINSET, 2500, 2250
CNCTSET, 2550, 2300


$   CONTROL SYSTEM   $
ASECONT, 2600, 2350, 2400, 2450, 2500, 2550, 0, 0


$   "ORIGINAL" ZAERO FLUTTER ANALYSIS BULK DATA SECTION   $
CORD2R, 9002, 0, 390.003, -17.561, -27.695, 389.8731, 170.5019, -78.0359, +CS6Y3
+cS6Y3, 398.243, -17.456, -27.241


AEROZ, 9002, YES, NO, SLIN, IN, 55.0, 23.0, 1265.0, +AZ1
+AZ1, 0.0, 0.0, 0.0


MKAEROZ, 95, 0.95, 0, 0, SAVE, FLUTTER9, 5.AIC, 0, +MK20
+MK20, 0.82, 0.918, 1.016, 1.114, 1.212, 1.310, 1.408, 1.506, +MK21
+MK21, 1.604, 1.70
```

A-13

```
CAERO7, 1000, VENTRAL, 0, 5, 11, 0, 0, 0, +CA1
+CA1, 0.0, 0.0, 0.0, 55.0, 0, 0, , , +CA2
+CA2, 11.6, 23.0, 0.0, 43.4, 0, 0


SPLINE1, 10, , 0, 100, 200, 0.0, 0.01


PANLST1, 100, 1000, 1000, 1039


SET1, 200, 910201, 910202, 910203, 910204, 910205, 910206, 910207, +ST1
+ST1, 910208, 910209, 910210, 910211, 910212, 910213, 910214, 910215, +ST2
+ST2, 910216, 910217, 910218, 910219, 910220, 910221, 910222, 910223, +ST3
+ST3, 910224, 910225, 910226, 910227, 910228, 910229, 910230, 910231, +ST4
+ST4, 910232, 910233, 910234, 910235, 910236, 910237, 910238, 910239, +ST5
+ST5, 910240, 910241, 910242, 910243, 910244, 910245, 910246, 910247, +ST6
+ST6, 910248, 910249, 910250, 910251, 910252, 910253, 910254, 910255, +ST7
+ST7, 910256, 910257, 910258, 910259, 910260, 910271, 910272, 910273, +ST8
+ST8, 910274, 910275, 910276, 910277, 910278, 910279, 910280, 910281, +ST9
+ST9, 910282, 910283, 910284, 910285, 910286, 910289, 910290, 910291, +ST10
+ST10, 910292, 910400, 910402, 910403, 910404, 910405, 910406, 910407, +ST11
+ST11, 910408, 910409, 910410, 910411, 910412, 910413, 910414, 910415, +ST12
+ST12, 910416, 910417, 910418, 910419, 910420, 910421, 910422, 910424, +ST13
+ST13, 917022, 917025, 917026, 917028, 917030, 917032, 917034, 917038, +ST14
+ST14, 917063, 917066, 917074, 917078, 917081, 917084


$   MATCH-POINT FLUTTER ANALYSIS - SUBCASE 1   $


FLUTTER, 40000, SYM, 800, 0, 0, 0, 0, 0


FIXMATM, 800, 95, 0, SLIN, IN, 20.16, 0, 0, +FH1
+FH1,-114.0E4,-108.0E4,-102.0E4,-96.0E4,-90.0E4,-84.0E4,-78.0E4,-72.0E4,+FH2
+FH2,-66.0E4,-60.0E4,-54.0E4,-48.0E4,-42.0E4,-36.0E4,-30.0E4,-24.0E4,+FH3
+FH3,-18.0E4,-12.0E4,-6.0E4, 0.0, 6.0E4


$   PLOT CARDS   $
```

```
$   * PLOT AERO MODEL BY PLTAERO *   $
PLTAERO, 11, YES, 0, TECPLOT, VENTAERO, .PLT


$   * PLOT FLUTTER MODE BY PLTFLUT *   $
PLTFLUT, 12, 20000, 1, 8, 0.3, TECPLOT, FLUT1.PL, T


PLTMODE, 13, SYM, 1, , 0.3, FEMAP, MODE1.NE, U
PLTMODE, 14, SYM, 2, , 0.3, FEMAP, MODE2.NE, U


$   * V-G PLOT *   $
PLTVG, 15, 10000, 5, V, FEMAP, Opt80VG1, .NEU
PLTVG, 16, 20000, 5, V, FEMAP, Opt85VG1, .NEU
PLTVG, 17, 30000, 5, V, FEMAP, Opt90VG1, .NEU
PLTVG, 18, 40000, 5, V, FEMAP, Opt95VG1, .NEU


ENDDATA
```

Bibliography

1. Burnham, Jay K. *Structural Technology and Analysis Program (STAP), Delivery Order 0017: Active Vibration Suppression Technology Buffet Load Alleviation (BLA) Program*. Technical Report AFRL-VA-WP-TR-2002-3002, WPAFB, OH 45433: Air Force Research Laboratory, June 2001.

2. Computational Methods Corporation. *Modification, F-16 Right Hand Ventral Fin*, 2003. Product Specifications Package.

3. Cook, Robert D. and others. *Concepts and Applications of Finite Element Analysis*. New York, NY: John Wiley & Sons, Inc., 2002.

4. Cunningham, Atlee M. *Buzz, Buffet and LCO on Military Aircraft - The Aeroelastician's Nightmares*. Technical Report, Fort Worth, TX: Lockheed Martin Aeronautics Company, 2003.

5. Cunningham, Atlee M. *Weapons Systems/Aircraft Integration: Dynamic Trials and Tribulations*. Technical Report RTO-MP-IST-999, Fort Worth, TX: Lockheed Martin Aeronautics Company, 2004.

6. Daue, Thomas, "Piezoelectric patches." Electronic Message, November 2004. Transmitted to Shawn Morgenstern.

7. "Dutch Air Force Test Results." Letter and Attached Plots, October 2004. Sent to Leonard Shaw by Atlee Cunningham and forwarded to Shawn Morgenstern.

8. *F-16 LANTIRN Pod Turbulence Evaluation - Vibration Investigation (CCP 9199)*. Technical Report F33657-82-C-2038, May 1985.

9. Gibswon, Warren C. *Piezoelectric Elements in ASTROS, User's Manual*. Palo Alto, CA 94303: CSA Engineering, Inc., June 1997.

10. Hanagud, Sathyanaraya. *F-15 Tail Buffet Alleviation: A Smart Structure Approach*. Technical Report, Atlanta, GA 30332: School of Aerospace Engineering, Georgia Institute of Technology, December 1998.

11. Hopkins, Mark, et al. "Active Vibration Suppresion Systems Applied to Twin Tail Buffeting." *International Society for Optical Engineering*. Number 3326. Pages 27–33. 1998.

12. Lazarus, Kenneth B. and Gregory S. Agnes. "An Active Smart Material System for Buffet Load Alleviation." *International Society for Optical Engineering*. Number 2447. Pages 179–192. March 1995.

13. Minarecioglu, Selen E., "Ventral Fin NASTRAN Model Question." Electronic Message, September 2004. Transmitted to Bob Bair from Selen E. Minarecioglu.

14. Morgenstern, Shawn D., et al. *Limited Characterization of Dual Bimorph Synthetic Jet Actuators: Aeroelastic Load Control - Phase I, Project HAVE PUFF*. Technical Information Memorandum AFFTC-TIM-05-07, Edwards AFB, CA 93524: Air Force Flight Test Center, December 2005.

15. Moses, Robert W. *Active Vertical Tail Buffeting Alleviation on a Twin-Tail Fighter Configuration in a Wind Tunnel*. Conference Paper, Hampton, VA 23681: Aeroelasticity Branch, NASA Langley Research Center, 1997.

16. Moses, Robert W. "Vertical Tail Buffetting Alleviation Using Piezoelectric Actuators - Some Results of the Actively Controlled Response of Buffet-Affected Tails (ACROBAT) Program." *International Society for Optical Engineering*. Number 3044. Pages 87–98. 1997.

17. Moses, Robert W. *Active Vertical Tail Buffeting Alleviation on an F/A-18 Model in a Wind Tunnel*. Technical Report, Hampton, VA 23681: Aeroelasticity Branch, NASA Langley Research Center, 1998.

18. Moses, Robert W. *NASA Langley Research Center's Contributions to International Active Buffeting Alleviation Programs*. Technical Report, Hampton, VA 23681: Aeroelasticity Branch, NASA Langley Research Center, 1999.

19. Moses, Robert W., et al. "Evaluation of New Actuators in a Buffet Loads Environment." *International Society for Optical Engineering*. Number 4332. Pages 10–21. 2001.

20. MSC.Software Corporation, Santa Ana, CA 92707. *MSC.Nastran 2001, Getting Started with MSC.Nastran Users Guide*, 2001. Software Manual.

21. MSC.Software Corporation, Santa Ana, CA 92707. *MSC.Nastran Version 68, Basic Dynamic Analysis Users Guide*, 2001. Software Manual.

22. MSC.Software Corporation, Santa Ana, CA 92707. *MSC.Nastran 2004 Design Sensitivity and Optimization Users Guide*, 2003. Software Manual.

23. Pinkerton, Jennifer L., et al. "Controlled Aeroelastic Response and Airfoil Shaping Using Adaptive Materials and Integrated Systems." *International Society for Optical Engineering*. Number 2717. Pages 166–177. January 1996.

24. Ret, Paul. *F-16 Block 40 Ventral Fin Failure (Failure Analysis)*. Technical Report WL/MLS 97-062, Wright-Patterson AFB, OH 45433: Materials Integrity Branch (WL/MLSA), July 1997.

25. Rogers, Lynn. *Durability Patch Considerations for F-16 Ventral Fin*. Technical Report, January 1994.

26. Sacarcelik, Ozer, "Use of Smart Material Corporation Piezoelectric Actuators." Electronic Message, February 2005. Transmitted to Shawn Morgenstern from Ozer Scarcelik of the Smart Materials corporation.

27. Shaw, Leonard L., et al. "Active Control of a Pod Wake-Mid-Scale Application." *American Institute of Aeronautics and Astronautics*. Number 2005-799. Pages 1–10. January 2005.

28. Sheta, Essam F., et al. "An Active Smart Material Control System for F/A-18 Buffet Alleviation." *International Forum on Aeroelasticity and Structural Dynamics*. June 2003.

29. Smart Material Corporation. *Macro Fiber Composite (MFC) Engineering Properties*, 2004. Product Specifications Sheet.

30. Smith, Brian R., et al. "Active Control of a Pod Wake." *American Institute of Aeronautics and Astronautics*. Number 2002-3067. Pages 1–10. June 2002.

31. Sodano, Henry A., et al. "An Investigation into the Performance of Macro-Fiber Composites for Sensing and Structural Vibration Applications." *Mechanical Systems and Signal Processing*. Number 18 (2004). Pages 683–697. May 2003.

32. Toth, Raymond G. *Nonlinear, Transonic Flutter Prediction for F-16 Stores Configuration Clearance*. MS thesis, Graduate School of Engineering, Air Force Institute of Technology (AETC), Wright-Patterson AFB OH, March 2003. AFIT/GAE/ENY/03-8.

33. van Tongeren, J.H., et al. *F-16 Ventral Fins Analysis*. Technical Report NLR-CR-99366, Amsterdam, The Netherlands: National Aerospace Laboratory, August 1999.

34. "Ventral Fin Failure Background." Slide Presentation, April 1993. Given to Shawn Morgenstern by Mr. Bob Bair of the Aeronautical Systems Center, WPAFB, OH.

35. Williams, R. Brett, et al. *Nonlinear Tensile and Shear Behavior of Macro Fiber Composite Actuators*. Technical Report, Blacksburg, VA 24061: Department of Mechanical Engineering, Virginia Polytechnic Institute.

36. ZONA Technology, Inc. *ZAERO Theoretical Manual, Version 7.1*. Scottsdale, AZ 85251: ZONA Technology, Inc., September 2004.

37. ZONA Technology, Inc. *ZAERO User's Manual, Version 7.1*. Scottsdale, AZ 85251: ZONA Technology, Inc., September 2004.

Vita

Captain Shawn D. Morgenstern was born in Denver, Colorado and lived in Montana, Alaska, Utah and Ohio as an Air Force dependent. He graduated from Beavercreek High School in 1990 and attended college at the University of Cincinnati where he earned a Bachelor of Science degree in Mechanical Engineering.

As a Distinguished Graduate of ROTC, Captain Morgenstern attended Undergraduate Space and Missile Training at Vandenberg AFB, California where he was also a Distinguished Graduate. Following a month of system-specific training, he was assigned to the Ballistic Missile Early Warning System site in Thule, Greenland for 14 months where he served as a Crew Commander and the Chief of Standardization and Evaluation. In 1998, he returned to Vandenberg AFB for the Defense Satellite Communications System III satellite Initial Qualification Training course for which he was recognized as a Distinguished Graduate. After being assigned to the 3rd Space Operations Squadron at Schriever AFB, Colorado, Captain Morgenstern served as a Satellite Vehicle Operator and a Satellite Engineering Officer, conducted training for all crew members, performed launch and early orbit operations for two brand new satellites, and completed his tour as a Crew Commander. Additionally, he was a member of the 50th Space Wing's championship Guardian Challenge team in 1999. After departing Schriever AFB in 2001, he was assigned to the 412th Test Wing at Edwards AFB, California where he was an avionics Flight Test Engineer for the F/A-22 Combined Test Force.

Captain Morgenstern was selected for the combined Air Force Institute of Technology/Test Pilot School program in 2002, and entered the Air Force Institute of Technology master's degree program in August of 2003. He graduated from the Test Pilot School in December of 2005 with a diploma for completion of the Experimental Flight Test Engineer course. This thesis provides the final document required for him to earn his Master of Science Degree in Aeronautical Engineering.

Permanent address: 2950 Hobson Way
WPAFB, OH 45433

1. REPORT DATE *(DD-MM-YYYY)* 23 Mar 06	2. REPORT TYPE **Master's Thesis**		3. DATES COVERED *(From – To)* Aug 2003 – Feb 2006
4. TITLE AND SUBTITLE ALLEVIATION OF BUFFET-INDUCED VIBRATION USING PIEZOELECTRIC ACTUATORS			5a. CONTRACT NUMBER
			5b. GRANT NUMBER
			5c. PROGRAM ELEMENT NUMBER
6. AUTHOR(S) Morgenstern, Shawn D., Capt, USAF			5d. PROJECT NUMBER 05-209 and 05-313
			5e. TASK NUMBER
			5f. WORK UNIT NUMBER
7. PERFORMING ORGANIZATION NAMES(S) AND ADDRESS(S) Air Force Institute of Technology Graduate School of Engineering and Management (AFIT/EN) 2950 Hobson Way Wright-Patterson AFB, OH 45433-7765			8. PERFORMING ORGANIZATION REPORT NUMBER AFIT/GAE/ENY/06-M25
9. SPONSORING/MONITORING AGENCY NAME(S) AND ADDRESS(ES) Air Force Research Laboratory/Air Vehicles Directorate (AFRL/VA) ATTN: Mr. Leonard Shaw 2790 D Street, Building 65 Wright-Patterson AFB, OH 45433-7765			10. SPONSOR/MONITOR'S ACRONYM(S)
			11. SPONSOR/MONITOR'S REPORT NUMBER(S)

12. DISTRIBUTION/AVAILABILITY STATEMENT
APPROVED FOR PUBLIC RELEASE; DISTRIBUTION UNLIMITED.

13. SUPPLEMENTARY NOTES

14. ABSTRACT
Buffet-induced vibration has been problematic for aircraft structures for many years. The F-16 ventral fin, while prone to these effects, lends itself well to the evaluation of modern active structural and flow control technologies.

The objective of this research was to determine the most critical natural modes of vibration for the F-16 ventral fin and design piezoelectric actuators capable of reducing buffet-induced ventral fin vibration. A finite element model (FEM) for the fin was developed, tuned and optimized to closely match published modal frequencies. Piezoelectric actuator patches were designed using the strain characteristics of the FEM and integrated into the model using a thermal analogy which allowed voltage application and the resulting strain to be simulated by a change in temperature. Two phases of critical mode selection were completed and included reviews of existing flight test data, historical ventral fin failure characteristics, and the results of aeroelastic and closed-loop aeroservoelastic analyses conducted on the FEM.

Results showed the FEM tuning and optimization procedures, as well as the design and implementation process for the piezoelectric actuators to be very effective. Modes 1, 2 and 4 were determined to be the most suitable for future application of the technology.

15. SUBJECT TERMS
Aeroelastic, Aeroelastic Load Control (ALC), Damping, F-16B, Finite Element Model (FEM), Flight Testing, NASTRAN, Natural Modes, Optimization, Piezoelectric Actuator, Smart Materials, Structure, Test Pilot School (TPS), Ventral Fin, Vibration

16. SECURITY CLASSIFICATION OF:			17. LIMITATION OF ABSTRACT	18. NUMBER OF PAGES	19a. NAME OF RESPONSIBLE PERSON Robert A. Canfield, Ph.D., ENY
REPORT **U**	ABSTRACT **U**	c. THIS PAGE **U**	**UU**	118	19b. TELEPHONE NUMBER *(Include area code)* (937) 255-3636 x4723; Robert.Canfield @afit.edu